Politecnico di Torino

POLITECNICO DI TORINO
Department of Mathematical Sciences

SWINBURNE UNIVERSITY OF TECHNOLOGY
Department of Mathematics,
School of Science, Computing and Emerging Technologies

Master's Degree in
MATHEMATICAL ENGINEERING

Fighting cancer with mathematics: modelling of virotherapy and oncolytic viruses

Supervisors:
Prof. Marcello Edoardo Delitala
Prof. Federico Frascoli

Co-Supervisor:
Dr. David Morselli

Master's Thesis by:
Emma Ciccarelli
Matriculation number 318291

Academic Year 2024-2025

Abstract

The increasing complexity of solid tumours demands the development of innovative and personalised therapeutic approaches. This thesis aims to analyse, through mathematical modelling, the therapeutic potential of oncolytic virotherapy, an emerging strategy that uses genetically modified viruses to selectively infect tumour cells while simultaneously stimulating an antitumour immune response. However, the effectiveness of this therapy is hindered by resistance to infection and the complex interaction between tumour cells, immune system and tumour microenvironment. To this end, this work integrates mathematical and computational tools to simulate the dynamics of viral infection, with a detailed analysis of the interactions between tumour cells and viruses, considering key factors such as epigenetics, phenotypic variability, and the spatial dynamics of cell growth.

Two models are developed and compared: a continuous model based on partial differential equations (PDE) and a discrete agent-based model (ABM). The simulations, conducted in one spatial dimension, show how epigenetic and infectious parameters influence virus propagation and tumour response to therapy. In particular, the introduction of epigenetic averaging proves to be a useful tool to understand the phenotypic distribution of the tumour population and its impact on viral spread.

Simulations are carried out to explore different therapeutic scenarios, evaluating how various parameters affect infection spread and treatment efficacy. The results show that tumour response to virotherapy is strongly dependent on tumour structure and virus ability to adapt to microenvironmental conditions, suggesting the importance of personalised therapeutic strategies to improve treatment success.

In conclusion, this study provides a theoretical and computational foundation for optimising virotherapy, demonstrating the crucial role of mathematical modelling in predicting tumour response and designing therapeutic strategies.

Contents

Chapter 1

Introduction

In recent decades, the fight against cancer has made significant progress also thanks to the emergence of innovative therapeutic approaches such as immunotherapy and virotherapy.

Immunotherapy is considered one of the most promising strategies for cancer treatment, as it uses the immune system to recognise and destroy cancer cells. However, the effectiveness of this therapy can be limited by various factors, some of which are highly sensitive to the tumour microenvironment. In particular, one of those factors is hypoxia, a condition characterised by low oxygen availability that contributes to resistance to treatment and disease progression.

Another strategy, **oncolytic virotherapy**, is also emerging as a promising therapy: it uses oncolytic viruses, genetically modified viruses designed to selectively infect and destroy tumour cells while simultaneously stimulating an immune response against the tumour. Unlike traditional therapies, virotherapy offers the advantage of acting directly on cancer cells without harming the surrounding healthy tissues and is known to help improving the immune response.

The combination of virotherapy and immunotherapy represents an innovative approach aimed at enhancing overall treatment efficacy by overcoming limitations related to hypoxia and other factors in the tumour microenvironment.

Immunotherapy is a field of great interest and has revolutionised cancer medicine. Recent advances in virotherapy suggest that it too may provide an equally valuable path to address current challenges in cancer treatment.

Solid tumours are defined as abnormal aggregations of cells arising from uncontrolled proliferation within a specific tissue or organ, and are characterised by a distinct structural organisation and interaction with the surrounding microenvironment. Some solid tumours, for their high cellular heterogeneity and complex interactions with the microenvironment, require sophisticated approaches to understand and predict the therapeutic response. Therefore, mathematical and computational models prove to be valuable tools for analysing and optimising these therapies, as they allow the simulation of complex interactions among tumour cells, oncolytic viruses and the immune system.

1.1 The role of hypoxia in the tumour microenvironment

Hypoxia is a feature of tumours caused by the rapid proliferation of cells that exceeds the ability of the vascular system to adequately supply oxygen to the tumour tissue. This oxygen deficiency often leads tumour cells to become more aggressive and resistant to treatments, causing changes that promote both tumour cell survival and their ability to evade the immune

system. For these reasons, hypoxia represents a major challenge in the fight against cancer.

1.2 The effect of oncolytic viruses and immunotherapies

As mentioned above, oncolytic viruses represent a powerful tool, as they are capable of stimulating an antitumour immune response. However, their effectiveness is influenced by interactions with the tumour microenvironment and hypoxia. To understand the optimal conditions under which the virus can infect tumour cells and activate the immune system, advanced mathematical models are used to identify strategies to enhance the efficacy of therapy.

The combination of computational and analytical methods also enables the integration of a large volume of clinical and experimental data into the models, allowing for a more accurate description of the dynamics of the immune response.

1.3 Virotherapy: an alliance between virus and immune system

Oncolytic virotherapy is an innovative strategy: by harnessing viruses that are capable of infecting tumour cells without damaging the surrounding healthy tissues, it represents a promising alternative to traditional therapies. When viruses infect tumour cells, they not only directly destroy them, but also stimulate an immune response that is usually better directed at attacking the tumour. In turn, viral infection can alter and weaken the tumour, making cancer cells more sensitive to additional treatments such as chemotherapy or immunotherapy.

1.4 Generic resistance to infection in the tumour context

Tumours are known to be able to develop generic resistance to infection, preventing also oncolytic viruses from effectively infecting cells. Resistance to infection is a complex phenomenon that involves various defense mechanisms, including the activation of the immune response of the body and the formation of physical barriers such as the extracellular matrix.

In addition, hypoxia can further exacerbate generic resistance to infection: tumour cells can develop strategies to avoid recognition by the immune system, making it more difficult for the virus to spread within the tumour. Therefore, understanding the mechanisms of resistance to infection represents a key step toward improving the efficacy of virotherapy and other cancer treatments. This is another aspect where mathematics can help.

A natural question arises: *Why virotherapy and not just immunotherapy?*

Although immunotherapy has represented a breakthrough in cancer treatment, many tumours continue to be unresponsive to this therapy due to intrinsic factors, such as hypoxia and resistance. These factors reduce the effectiveness of traditional immunotherapies, highlighting the need for complementary approaches.

Virotherapy is considered a valid alternative, as oncolytic viruses not only act directly on tumour cells but also modify the tumour microenvironment in ways that enhance the effectiveness of the immune response. It is also considered a good adjuvant to traditional immune approaches.

1.5 Outline of the thesis

We now provide a brief overview of the structure of the thesis, summarising the contents of each chapter, some for review and other with original results.

Chapter 2 presents an extensive literature review, unified into a single chapter structured into three main sections.

The first section focuses on key theories and models in the field of cancer immunotherapy, with particular attention to aspects directly related or closely associated to virotherapy. The main emphasis is on the mathematical modelling of cancer therapies.

The second section explores mathematical models applied to the response of cancer immunotherapies in hypoxic and highly heterogeneous tumour environments, typical of certain cancers such as glioblastomas. It discusses coevolution models describing the interactions between tumour cells and immune system lymphocytes, population models structured by phenotype, and epidemiological models, with a focus on phenotypic adaptation and immunoresponse variability.

The final section of the chapter examines virotherapy in more detail. It highlights resistance mechanisms developed by tumour cells, particularly in hypoxic environments, and discusses strategies aimed at overcoming such barriers. Various studies have shown that phenotypic selection and tumour cell adaptation are key obstacles to the effectiveness of virotherapy. One promising strategy to counteract these resistance mechanisms is the combined use of virotherapy and immunotherapy.

Chapter 3 presents the mathematical models used to describe solid tumour growth and interactions with viral therapies. Two complementary approaches are described: continuous modelling, leading to partial differential equations (PDE), which simulates spatial and epigenetic diffusion, as well as large-scale growth and infection dynamics, and the agent-based modelling (ABM), which simulates individual cell interactions on a discretised spatial and temporal domain. In this chapter, the continuous PDE model is derived from the underlying agent-based counterpart.

Chapter 4 reports and analyses several simulations, all performed in one spatial dimension and with epigenetic variability. In the first part, infection spread and cell proliferation are examined by comparing predictions from the PDE and ABM models; in the second part, epigenetic averaging is introduced to analyse local variability in the tumour population and its impact on viral spread. Furthermore, initial conditions of the infected cells are modified to study their impact on the entire cell population. The analysis highlights how tumour environment and cellular diversity can determine the effectiveness of therapy. Finally, two key parameters, η and ζ, are studied to evaluate their effect on the response to treatment and to discuss possible therapy optimisation strategies.

Finally, **Chapter 5** presents the discussion and conclusions of the study. The main observations drawn from the models are outlined and future directions for improving oncolytic virotherapy are discussed, including possible developments in research through the integration of new mathematical equations and the use of advanced artificial intelligence techniques.

In addition, the **Appendix** takes the study a step further by extending the models to two spatial dimensions. The goal is to provide a more realistic representation of tumour growth and interaction with virotherapy. The necessary adaptations to the PDE and ABM models are discussed to account for the spatial spread of tumour cells and oncolytic viruses. Insights from simulations are presented and discussed.

Chapter 2

Literature Review

In this thesis, literature review is presented in a single chapter, divided into three distinct sections. This structure allows for a clearer and more focused exploration of the field, enabling each aspect of the literature to be examined in greater depth while maintaining a cohesive narrative.

This separation is not only structural but is also intended to make the reading and understanding of the current study easier and more accessible. In the following, we will select and comment upon some of the most relevant works in the field, concentrating on the salient aspects of the most mathematically and biologically valuable ideas.

2.1 Theories and mathematical models

In this section, we focus on the theories and models that have shaped the field. The section explores the main theoretical frameworks, highlighting key authors, foundational ideas, and significant developments. We concentrate particularly on works that have had a lasting impact and provide the foundation for this study. A brief discussion will be dedicated to the main mechanisms of immunotherapy, with particular attention to its interactions and synergies with oncolytic virotherapy.

2.1.1 Integration of mathematical models and therapeutic strategies

Mathematical modelling is valuable for understanding tumour growth and predicting the response to cancer treatments. The heterogeneous nature of most tumours makes them quite complex, requiring advanced approaches to understand and anticipate the body's response to oncological therapies.

In this regard, the study by **Enderling and Chaplain (2014)** [1] provides a detailed overview of the mathematical techniques applied to the analysis of tumour progression and its interaction with various therapeutic strategies. The authors explore the role of models based on differential equations in describing tumour growth dynamics and response to treatments, including chemotherapy, radiotherapy, immunotherapy and oncolytic virotherapy. One key aspect of their work is the analysis of interactions between the tumour and its surrounding microenvironment, emphasising how external factors, such as the immune system and tumour vascularisation, influence treatment effectiveness. In addition, the study shows how the use of predictive models can help optimise therapeutic strategies by identifying crucial parameters that determine the efficacy of treatment. Specifically, the modelling approach suggests that personalised combination therapies, tailored to the biological characteristics of the tumour, can significantly improve clinical outcomes compared to standardised treatments.

The use of advanced statistical methods is essential in cancer research, particularly for

the analysis of biomarker and the evaluation of new therapies. **Dejardin et al. (2023)** [2] provide a detailed analysis of statistical methodologies used in the study of biomarkers during the early stages of immunotherapy development. The authors explore statistical modelling techniques, including regression methods and multivariate analysis, to identify predictive clues of treatment response. The study also discusses the use of machine learning models and Bayesian approaches to improve the prediction of responses.

2.1.2 Synergy between immunotherapy and oncolytic virotherapy

As mentioned, the combination of oncolytic virotherapy and immunotherapy represents a promising strategy in cancer treatment, utilising the synergistic action between viruses and immune system to enhance an antitumour response.

A significant example among the many available is the **IGNYTE clinical trial (2024)** [3], which evaluated the effectiveness of *RP1*, an oncolytic virus, in combination with *nivolumab*, a checkpoint inhibitor, in patients with advanced melanoma refractory to other immunotherapies. Checkpoint inhibitors are immunotherapeutic agents that block specific molecules, such as PD-1 or CTLA-4, which tumours exploit to suppress immune responses. By inhibiting these pathways, checkpoint inhibitors restore the ability of T cells to recognize and eliminate cancer cells, enhancing the overall antitumour immune activity. The results showed an objective response in 33.6% of the treated patients, with a median response duration of 27.6 months. This suggests that the addition of the oncolytic virus can reactivate the immune system even in previously non-responsive cases, with significant improvement of patients' outcomes.

Another relevant study was presented at the **ESMO Immuno-Oncology Congress (2024)** [4], where the benefits of combining oncolytic viruses with immunotherapies were discussed. This combination aims to enhance the immune response through induction of immunogenic cell death, improving therapeutic efficacy compared to the use of single treatments. In particular, early-phase results on the oncolytic adenovirus ORCA-010 in patients with prostate cancer showed that the intratumoural administration of the virus induced both local and systemic antitumour immune responses. An increased activation and proliferation of CD8+ T cells was observed, effectively transforming the tumour microenvironment from "cold" to "hot". Furthermore, peripheral blood analysis confirmed a rise in activated and proliferating those cells in the weeks following treatment. These findings suggest that oncolytic viruses can prime the immune system, potentially enhancing the efficacy of subsequent immunotherapies.

These studies highlight the importance of combined therapeutic strategies that integrate oncolytic virotherapy and immunotherapy, offering new hope for treating tumours resistant to conventional therapies.

2.1.3 Mathematical modelling of virotherapy

A mathematical approach in oncolytic virotherapy is essential to understand and optimise the dynamics between oncolytic viruses, tumour cells and the immune system.

For example, the study by **Paiva et al. (2013)** [5] proposes a multiscale model to analyse the effect of suppressing adaptive immunity on cancer virotherapy. In their work, the authors develop a model that integrates different levels of analysis, from molecular processes to cellular and tissue dynamics, to study the interaction between virus and host immune response. The model is based on differential equations that describe viral replication, tumour cell destruction and immune system activation. A key finding from the study is that the immune response can limit the efficacy of virotherapy, as the immune system tends to eliminate the

virus before it can fully eradicate the tumour.

Closely related to virotherapy, **Wodarz and Komarova (2005)** [6] have been some of the first to offer an in-depth analysis of the application of mathematical models to understand tumour growth and cancer cell evolution. Their book is particularly relevant to a thesis on oncolytic virotherapy, as it dedicates a specific section to gene therapy and oncolytic virus therapy. In that section, the authors explore how models can describe the interaction between viruses and tumour cells, evaluating the effectiveness of different therapeutic strategies and providing insights to optimise virus-based cancer treatments. In addition, the book addresses related topics such as cancer cell evolution, drug resistance dynamics, and the impact of immune responses, offering a comprehensive and integrated view of tumour dynamics and possible therapeutic interventions. It overall represents a valuable resource for any mathematical modeller interested in these systems.

Other interesting works are also present in the literature and are useful for this thesis. For example, **Morselli et al. (2024)** [7] propose a hybrid discrete-continuum modelling approach to study the interactions between the immune system and oncolytic viral infections. They presents a mathematical framework to study the interplay between oncolytic virotherapy and the immune response. The authors integrate an agent-based stochastic model with a continuum PDE system to simulate spatial-temporal interactions among tumour, infected, and immune cells. Simulations indicate that an overly rapid immune response may hinder the efficacy of virotherapy, highlighting the need for carefully timed immunomodulation. The study emphasises the importance of stochastic effects in tumour dynamics and offers insights for optimising combined virotherapy-immunotherapy strategies.

Zou et al. (2022) [8] provide an overview of the latest advancements in oncolytic virotherapy and its integration with other immunotherapeutic approaches. The authors discuss the mechanisms by which oncolytic viruses induce tumour cell lysis and stimulate host immune responses, thereby enhancing the therapeutic efficacy against various cancers. They also address the challenges associated with this therapeutic strategy, including issues related to viral delivery, immune evasion, and the tumour microenvironment. The review highlights the potential of combining oncolytic virotherapy with other immunotherapies to overcome these challenges and improve treatment outcomes.

Malinzi et al. (2018) [9] present a mathematical model to explore the synergistic effects of combining oncolytic virotherapy (OV) with chemotherapy. The authors develop an ordinary differential equation (ODE)-based model that incorporates tumour cells, immune responses, and treatment dynamics. Stability analysis indicates that chemotherapy alone can eliminate tumour cells if its efficacy surpasses the tumour's intrinsic growth rate. However, OV alone may not eradicate tumour cells but can enhance chemotherapy's effectiveness when using potent viruses. The study employs sensitivity analysis to identify critical chemotherapy doses beyond which further tumour reduction is minimal. Optimal control theory, specifically Pontryagin's maximum principle, is applied to determine the optimal combination of chemotherapy and OV, suggesting that administering half of the maximum tolerated doses of both treatments yields the most effective outcome. Numerical simulations support these findings, highlighting the importance of virus burst size, infection rate, and drug dosage in successful combinatorial therapy.

Other recent mathematical models have also significantly contributed to the understanding of cancer immunotherapy dynamics. **Wilkie and Hahnfeldt (2013)** [10] provide a comprehensive overview of immune-tumour interactions, highlighting tumour dormancy as a crucial transitional state modulated by immune response. Their work bridges immunological mechanisms with virotherapeutic dynamics. **De Pillis and Radunskaya (2003)** [11] developed an optimally controlled model integrating immune responses with therapeutic strategies, offering foundational tools to simulate the impact of virotherapy. These models are key to conceptualising virus-host-tumour triads in oncolytic applications.

Timalsina et al. (2017) [12] introduce a novel mathematical framework utilising partial differential equations to investigate tumour virotherapy in the context of mediated immunity. This model integrates both innate and adaptive immune responses, capturing the complex interactions among tumour cells, oncolytic viruses, and the immune system within a domain featuring a moving boundary. Through extensive numerical simulations, the study examines tumour development under various conditions, providing insights into key aspects of virotherapy, including the dependence of efficacy on critical parameters and the impact of delays in adaptive immunity. The findings offer valuable perspectives on enhancing virotherapy strategies for tumour treatment, examining how different immune components affect viral spread and tumour clearance.

Finally, **Wang et al. (2024)** [13] summarise recent advances in oncolytic virus immunotherapy, with a focus on mechanisms of immune activation and promising preclinical and clinical results. The authors provide a comprehensive review of the current progress in combining oncolytic viruses with various therapeutic strategies, including immune checkpoint inhibitors, chemotherapy, targeted therapy, and cellular therapy; they also discuss the advantages of oncolytic viruses, such as high killing efficiency, excellent targeting capabilities, minimal adverse reactions, and multiple pathways for tumour destruction. However, they also note that the efficacy of oncolytic viruses as a monotherapy often falls short of expectations. Therefore, combining oncolytic viruses with other treatments to achieve synergistic effects has emerged as a promising direction for the development of oncolytic virus therapies. The review aims to offer valuable insights and references for the further advancement of these combination strategies in clinical applications.

2.2 Coevolution, epigenetics, and therapies in tumour dynamics

This section discusses the methodological approaches used, the main results obtained, and the practical implications of the research conducted. The chapter is expanded with recent studies and articles that explore the topic from various perspectives, with the aim of offering a more structured view.

Despite growing interest in oncolytic virotherapy, a quantitative understanding of its effectiveness and infection dynamics remains an open challenge. The virus' ability to spread and induce an immune response depends on numerous factors, including tumour cell density, epigenetic susceptibility and interactions with the surrounding microenvironment.

One of the objectives of this second review section is to compare two mathematical approaches, partial differential equation (PDE) models and agent-based models (ABMs) to capture the role of epigenetics and viral infectivity in tumour progression and the response to virotherapy.

The development of mathematical models, based on differential equations and stochastic simulations, is a possible approach to addressing the challenges of evolutionary dynamics of tumours and their adaptation to antitumour therapies. In particular, recent studies are examined that investigate both coevolutionary processes between tumour cells and cytotoxic T lymphocytes (CTLs), and models for phenotype-structured populations and epidemic dynamics, to highlight the mechanisms underlying tumour resistance.

Mathematical models addressing tumour heterogeneity and hypoxia provide vital insights into the spatial and phenotypic complexity affecting immunotherapy. **Tonekaboni et al. (2017)** [14] introduced a structured population model accounting for phenotypic plasticity, simulating tumour cell adaptation under immune pressure. **Gatenby and Gillies (2008)** [15] proposed a microenvironmental framework describing carcinogenesis as an evolutionary response to hypoxic stress, supporting the use of coevolutionary models to study immune-tumour dynamics. These studies are essential for analysing virotherapy in the context of evolving tumour resistance.

2.2.1 Coevolution models between tumour cells and CD8+ T lymphocytes

Almeida et al. (2022) [16] propose an individual-based mathematical model to analyse the co-evolutionary dynamics between CTLs and tumour cells, without spatial interactions, focussing on how phenotypic variability influences the effectiveness of immune response. The model also includes a continuous version, derived through a deterministic limit, involving integro-differential equations for the phenotypic distribution of both tumour cells and CTLs. This model provides a useful theoretical framework for interpreting resistance phenomena and immune responses in tumours with phenotypic heterogeneity. It will be used extensively in our work.

Understanding the interactions between oncolytic virotherapy and the immune system is fundamental for optimising combined therapeutic strategies. The integration of CAR T cells with oncolytic viruses is an emerging area of research that promises to overcome the limitations of standalone therapies. CAR T cells (Chimeric Antigen Receptor T cells) are genetically modified T cells designed to express a receptor specific to cancer cell antigens. This modification enables T cells to target and kill tumour cells more efficiently than regular T cells, thus enhancing the immune response of the body against cancer. When combined with oncolytic viruses, CAR T cells can synergistically improve tumour targeting and immune activation. **Conte et al. (2025)** [17] recently proposed an experimental and modelling study that analyses the dynamics of interaction between CAR T cells targeting $IL-13R\alpha 2$ and an oncolytic virus specific for solid tumours. The work demonstrates that sequential administration of oncolytic viruses can modulate the tumour microenvironment, improving the infiltration and persistence of CAR T cells. One of the most interesting aspects of the model is the analysis of competition between oncolytic viruses and T lymphocytes in the tumour microenvironment, suggesting that viral replication can be modulated to enhance CAR T cytotoxic activity. This approach opens new avenues for personalised therapeutic strategies, based on controlled virus administration to optimise immune response.

2.2.2 Phenotype-structured population models and epigenetic adaptation

Chisholm et al. (2016) [18] develop a phenotype-structured population model that incorporates both spontaneous epigenetic variation and the effect of a hostile environment, such as that typical of tumour metastases. They used an agent-based model and an integro-differential equation to describe an asexually reproducing population, undergoing random phenotypic changes and subject to environmental selective pressures. The study shows how epigenetic changes can influence the adaptation of a population under rapidly changing environmental conditions.
Although not directly related to the tumour microenvironment, it provides a theoretical foundation for the role of epigenetics in tumour cell adaptation in hypoxic environments, helping explain the phenomena of acquired resistance to antitumour therapies. This occurence is one of the major hindrances for the success of clinical therapies.

Macfarlane et al. (2022) [19] contribute a model that compares an individual-based and a continuous approach to describe cell populations with phenotypic variability, providing a detailed picture of growth and invasion dynamics. The model offers a useful perspective to understand how phenotypic heterogeneity can facilitate tumour invasion and adaptation to stress conditions such as hypoxia.

2.2.3 Susceptible-Infectious models with phenotype structured

The Susceptible-Infectious (SI) model is a basic compartmental model used in epidemiology to describe the spread of infectious diseases within a population. In this model, individuals are classified into two compartments: those who are susceptible to infection (S) and those who are infectious (I). The model tracks the transition of individuals from the susceptible to the

infectious compartment, based on the rate of infection. It is commonly used to analyse the early stages of disease outbreaks, where individuals can either become infected or remain susceptible, without considering other factors like recovery or immunity. The SI model proposed by **Lorenzi et al. (2021)** [20] considers a compartment of susceptible elements structured by phenotype, accounting for variability in infection resistance and proliferative potential. That model, applied in an epidemiological context, offers a framework for understanding how phenotypic variability can drive infection dynamics and the adaptive potential of susceptible populations under selective pressures.
Although developed for epidemics, the model provides an analytical structure for studying adaptation phenomena under selective pressure in a phenotype-structured system. Analyses show that higher levels of selection lead to reduced phenotypic heterogeneity, suggesting that more lethal infections favour individuals with higher resistance.

Another relevant addition in this section is the study by **Morselli et al. (2023)** [21], which explores the spatial dynamics of oncolytic virus infection in solid tumours using a stochastic agent-based model.
The study shows that the virus' ability to spread is strongly influenced by cell density and movement restrictions imposed by pressure in the tumour microenvironment, a factor potentially analogous to hypoxic pressure in highly heterogeneous tumours. Under pressure conditions, viral infections tend to remain confined to the tumour core and do not spread to the periphery. This shows how the phenotypic structure and environmental conditions can hinder the effectiveness of virotherapy in hypoxic tumour contexts.

Other noteworthy studies include the research by **Kaid et al. (2023)** [22], which presents a phenotype-structured model for tumour-immune response interactions, particularly in the context of immune checkpoint inhibitors (ICIs). Utilising a nonlocal integro-differential Lotka-Volterra framework, the model accounts for heterogeneity in tumour and immune cell populations through continuous phenotypic traits representing aggressiveness and anti-tumour efficacy, respectively. The analysis captures the dynamics of immunoediting, encompassing elimination, equilibrium, and escape phases. Numerical simulations demonstrate the model's capacity to replicate these phases and explore the potential impact of ICIs on tumour-immune dynamics.

Fiandaca et al. (2020) [23] develop a mathematical model to study the influence of hypoxia and acidity on the evolutionary dynamics of cancer cells in vascularised tumours. Formulated as a system of partial integro-differential equations, the model describes phenotypic evolution in response to spatial variations in oxygen, glucose, and lactate concentrations. Simulations reveal that nonlinear interactions between tumour cells and these abiotic factors can lead to environmental gradients, promoting phenotypic heterogeneity and selection for more aggressive cancer cell phenotypes. The study provides insights into how microenvironmental stressors drive tumour adaptation and resistance.

Furthermore, **Villa et al. (2024)** [24] propose a generalised moment dynamics approach to reduce phenotype-structured partial differential equation (PDE) models of cancer evolution to systems of ordinary differential equations (ODEs). This method employs moment generating functions and Taylor series expansions to derive moment equations, facilitating the analysis of phenotypic heterogeneity in cancer cell populations. By removing assumptions about distribution shapes, the framework offers flexibility in modelling phenotypic dynamics and simplifies computational complexity. The approach enhances the tractability of models addressing intratumour heterogeneity and adaptive dynamics.

Leschiera et al. (2021) [25] also propose a spatially explicit stochastic individual-based model to investigate the impact of intra-tumour heterogeneity (ITH) on the efficacy of CD8+ T cell immune responses. The model simulates interactions between tumour cells and CD8+ T cells, considering variations in antigen expression among tumour sub-populations. Results indicate that increased antigenic diversity and a higher proportion of non-immunogenic tu-

mour cells can diminish the effectiveness of immune surveillance. This framework aids in understanding mechanisms underlying variable immunotherapy outcomes.

Finally, let us conclude this short review with a significant contribution given by **Celora et al. (2021)** [26]: they present a phenotype-structured model exploring how phenotypic variation affects tumour growth dynamics and response to radiotherapy under normoxic and hypoxic conditions. Their findings indicate that hypoxia promotes the selection of more stem-like, radio-resistant cancer cell phenotypes, leading to increased tumour resilience. This study highlights the role of hypoxia-induced phenotypic plasticity in therapy resistance and is of value to the approach we present here.

2.3 Virotherapy and resistance to infection

This section explores the main aspects of virotherapy, with particular attention to the resistance that tumour cells can develop, especially in hypoxic environments. In particular, the mechanisms underlying resistance to virotherapy, such as phenotypic adaptation of tumour cells and reduced viral replication capacity under low oxygenation, will be analysed. Strategies proposed to overcome these issues will also be discussed, including the engineering of oncolytic viruses to enhance their effectiveness in hypoxic environments and the use of combination treatments with immunotherapy. The section concludes with an analysis of the therapeutic potential of these integrated approaches, suggesting how they can improve the results of virotherapy and overcome tumour resistance.

2.3.1 Resistance to viruses is crucial

Resistance to treatment, expecially in complex tumour environments such as those characterised by hypoxia, is particularly important. Hence, the use of oncolytic virotherapy combined with chemotherapy and immunotherapy has been studied in various contexts, especially because the combined use of multiple therapies is thought to be overall more efficient. For example, the study by **Wang et al. (2024)** [27] presents an advanced and mechanistically detailed investigation into the enhancement of cancer therapy via oncolytic virotherapy. The study introduces a modified vaccinia virus encoding hyaluronidase (OVV-Hyal1), which remodels the extracellular matrix by degrading hyaluronic acid in solid tumours. This remodelling facilitates improved intratumoural delivery of chemotherapy agents and enhances the efficacy of immunotherapy, including immune checkpoint inhibitors and CAR-T cells. The work provides robust preclinical evidence demonstrating improved tumour infiltration and antitumour responses. However, phenotypic selection and the adaptation of tumour cells in response to hypoxia are critical factors that influence the effectiveness of these therapies.

The study by **Zamarin et al. (2014)** [28] demonstrates that localised administration of Newcastle disease oncolytic virus can overcome systemic tumour resistance to immune checkpoint inhibitors such as anti-PD-1 and anti-CTLA-4. Oncolytic virotherapy not only acts directly on tumour cells, but also modulates the immune environment, promoting cytotoxic T lymphocyte infiltration and reducing immunosuppressive cells. This combined approach results in more effective tumour regression than immunotherapy alone.

The study by **Feng et al. (2018)** [29] explores the therapeutic enhancement achieved by combining oncolytic virotherapy with both chemotherapy and immunotherapy. The authors emphasise how this integrative approach may synergistically increase tumour cell cytotoxicity while also amplifying systemic immune responses. They discuss the potential of oncolytic viruses to disrupt the tumour microenvironment, thereby improving drug penetration and antigen presentation. However, the analysis remains largely theoretical and preclinical, offering limited in vivo data or clinical translation. Despite these limitations, it provides a solid foundation for the rationale behind multimodal cancer therapies, highlighting the need for

further translational and clinical research to validate the proposed strategies.

Another significant study on immunotherapy resistance is conducted by **Maio et al. (2022)** [30]. In this study, the researchers evaluate the effectiveness of combining two immunotherapeutic drugs, *ipilimumab* and *nivolumab*, with an epigenetic drug, *ASTX727*, in patients with melanoma and lung cancer who show resistance to standard, previous treatments. The results indicate that the addition of an epigenetic drug could modulate gene expression in tumour cells, making them a better target for the immune system and thus improving therapeutic response. This combined approach represents one of the currently investigated strategies to overcome resistance to immunotherapy in these tumours, some of which are explained below.

2.3.2 Strategies to overcome resistance to virotherapy

Several strategies have been proposed to overcome resistance to virotherapy, ranging from engineering better oncolytic viruses (to enhance their effectiveness) to the use of combination treatments.

As mentioned, hypoxia is a common feature of the tumour microenvironment and can significantly impact the efficacy of oncolytic virotherapy. **Aghi et al. (2009)** [31] explore how hypoxic conditions influence the replication of oncolytic herpes simplex virus (HSV) in tumour environments. Their findings reveal that certain strains, such as G207, replicate more effectively under low-oxygen conditions, highlighting an unexpected advantage of the tumour microenvironment. This discovery laid the groundwork for re-engineering oncolytic viruses to thrive in hypoxic niches. The study emphasises the value of adapting virotherapy to tumour physiology and suggests a paradigm shift where hypoxia is not just a barrier, but a potential asset to be leveraged.

Guo (2011) [32] present a comprehensive review on the effects of hypoxia across various types of oncolytic viruses. He discusses how oxygen deprivation can hinder viral spread and immune activation but also introduces approaches to counter these limitations, such as incorporating hypoxia-inducible elements. The author underlines the importance of tailoring virotherapies to withstand hypoxic stress, and advocates for combining virotherapy with agents that modulate tumour oxygenation. This work has become a reference point for subsequent innovations in hypoxia-adapted viral design.

Shayan et al. (2022) [33] provide new ideas on how to overcome hypoxia-related barriers in oncolytic virotherapy. They explore genetic modifications that enable viruses to preferentially replicate in low-oxygen zones, along with combination strategies involving radiation and antiangiogenic therapies. The authors emphasise the need for precise delivery systems and biomarker-driven approaches to enhance treatment efficacy in hypoxic tumours. Their work illustrates the growing sophistication of the field and the move toward more personalized, microenvironment-aware therapeutic platforms.

Resistance to oncolytic virotherapy remains a critical barrier, especially in hypoxic and heterogeneous tumours. **Russell et al. (2012)** [34] provide an extensive review of mechanisms limiting viral replication and spread, including innate resistance and cellular adaptation.

Genetic modification of oncolytic viruses represents one of the most promising strategies for improving therapeutic efficacy in cancer treatment. Several studies have explored how specific genetic alterations can be used to increase tumour selectivity, replication, and immune stimulation. For instance, **Cristi et al. (2022)** [35] describe how the insertion of immunostimulatory genes, such as those encoding cytokines or checkpoint inhibitors, can en-

hance the recruitment and activation of immune cells within the tumour microenvironment. These modifications can improve viral spread and reduce the likelihood of tumour recurrence. Similarly, **Davola et al. (2020)** [36] highlight approaches for modifying oncolytic viruses to boost antitumour immune responses. This includes engineering viruses to express tumour antigens or immunomodulatory molecules, thereby turning "cold" tumours into "hot" ones capable of eliciting a systemic immune response.

The engineering of oncolytic viruses (OVs) seems particularly promising for the treatment of non-small cell lung cancer (NSCLC). In the study by **Yin and Wang (2024)** [37], the authors analyse how genetic modifications of OVs can improve the efficacy of checkpoint inhibitor therapy. The work discusses various strategies, including the insertion of genes that modulate the tumour microenvironment and enhance the antitumour immune response. The authors propose a detailed genomic framework for the design of OVs capable of increasing response to anti-PD-1 therapy, offering new perspectives for cancer immunotherapy. Furthermore, **Zhao et al. (2023)** [38] develop a structure-guided genetic modification strategy to adapt the Seneca Valley Virus (SVV) for use in NSCLC models that are otherwise non-responsive. Through targeted mutations such as S177A and P60S, the modified virus exhibited enhanced infectivity, immune evasion, and improved survival outcomes in murine models.

All findings above show that tumour resistance, especially in hypoxic environments, remains a significant barrier to therapeutic effectiveness. Phenotypic adaptation mechanisms and the selection of cells resistant to viral infection play a role in reducing the effectiveness of oncolytic viruses, negatively impacting their therapeutic potential in solid tumours. Numerous challenges remain related to the phenotypic variability of tumour cells and the complexity of the tumour microenvironment. Current research emphasises on optimising combination treatments that consider the evolutionary and adaptive dynamics of tumours, with the goal of improving the effectiveness and robustness of virotherapy as a therapeutic option. Other interesting studies in this field include, for instance, the work by **Dong et al. (2023)** [39], who explore the synergistic use of oncolytic viruses and immune checkpoint inhibitors in head and neck squamous cell carcinomas, showing promising immune-enhancing effects. **Garofalo et al. (2021)** [40] demonstrate that a novel oncolytic adenovirus combined with anti-PD1 therapy produced a significantly stronger antitumour response in a melanoma mouse model than either treatment alone. **Spiesschaert et al. (2021)** [41] review the mutual benefits of combining oncolytic viruses with small molecule drugs, highlighting their role in enhancing viral replication and modulating the tumour microenvironment. Finally, **Everts et al. (2020)** [42] propose a dual-targeting strategy that uses oncolytic viruses to simultaneously attack tumour cells and the surrounding stroma, thereby disrupting tumour support systems and enhancing treatment efficacy.

As the reader can appreciate from these examples, this field of investigation is very active, complex and stimulating, with continuosly new approaches and novel therapeutic techniques.

Chapter 3

Mathematical models and computational approaches

The solid tumours we dedicate our attention to are characterised by high heterogeneity and the influence of the hypoxic environment, making the use of advanced mathematical models essential to investigate cell growth and dynamic interactions with therapies and the microenvironment.
To understand the intricate interplay between cancer cells, viral therapies, and hypoxic conditions, two distinct but complementary mathematical models are employed for tumour behaviour analysis at different scales. The continuous model, based on partial differential equations (PDE), provides a mean-field view of the diffusion and evolution of infected and uninfected cells, while the agent-based model (ABM) offers a discrete view, describing the individual behaviour of tumour and infected cells within a spatially discrete environment. We now explore how these two models are used and integrated.

3.1 Discrete model: agent-based model (ABM)

The agent-based model (ABM) is a discrete and stochastic approach in which cells are considered as individual entities (agents) interacting with each other and, possibly, the surrounding environment within a spatial grid. Each cell can have different states (infected or uninfected) and an epigenetic trait value (for uninfected cells). The model allows simulation of stochastic events such as epigenetic mutation, spatial movement, and infection at the cellular level.

The main characteristic of an ABM is discretisation: time is divided into intervals $t_n = \tau n$, space into points $x_j = \delta j$, and the epigenetic variable into values $y_k = \chi k$. Here, $n \in \mathbb{N}_0$, $j \in \mathbb{Z}$, and $k = 0, ..., [1/\chi]$ are integer indices corresponding to discrete time steps, spatial positions, and epigenetic states, respectively. The parameters $0 < \tau \ll 1$, $0 < \delta \ll 1$, and $0 < \chi \ll 1$ represent the discretisation steps for time, space, and the epigenetic variable, defining the resolution at which the system is simulated. Consequently, discrete variables are used to represent infected and uninfected cells at specific grid positions at a given time. The ABM model features (with more details shortly) include:

- **Movement**: uninfected and infected cells move to adjacent points with given discrete probabilities, mimicking diffusive behaviour.
- **Epigenetic mutation**: uninfected cells can change their epigenetic trait to adjacent values with a certain probability, simulating stochastic variation.
- **Growth and death**: uninfected cells reproduce or die with a given probability, while infected cells die as well, according to their own probability.

- **Infection**: Uninfected cells can become infected depending on the local density of infected cells and the probability of transmission, as infected cells are capable of spreading the infection to nearby tumour cells.

The ABM allows modelling of local interactions and provides a way to characterise stochastic fluctuations among cells, giving a detailed representation of cellular dynamics not captured in continuous models. This discrete approach is particularly useful for exploring individual cell responses to epigenetic variations and infection pressure.

3.2 Continuous model: partial differential equations (PDE)

In the continuous model we propose, let us denote by $t \in [0, +\infty)$ the time, by $x \in \Omega$ the space variable, and by $y \in Y := [0, 1]$ the epigenetic variable. We first assume that as y increases, cells become less proliferative and more likely to be infected by the virus: this is due to the fact that a slower metabolic activity results in a slower infection. The key variables are as follows:

- $u\colon [0, +\infty) \times \Omega \times Y \to [0, +\infty)$: the structured uninfected cell density dependent on time t, spatial position x, and epigenetic variable y. The latter is continuous within the interval $[0, 1]$, representing phenotypic traits related to cell proliferation and susceptibility to viral infection.
- $i\colon [0, +\infty) \times \Omega \to [0, +\infty)$: the unstructured infected cell density, also dependent on time and spatial position but unaffected by the epigenetic variable.

The dynamics is described by a system of partial differential equations that combine spatial diffusion, epigenetic diffusion, and reaction terms that model growth, infection, and cell death. The PDE system enables the modelling of various phenomena:

1. **Spatial diffusion**: both infected and uninfected cells can move randomly in space, with their movement governed by diffusion coefficients.
2. **Epigenetic diffusion**: for uninfected cells, the epigenetic variable evolves over time, reflecting gradual changes in epigenetic traits influencing proliferation and viral susceptibility.
3. **Growth and reaction to infection**: cell growth depends on the local total density of uninfected cells, defined as $\rho(t, \underline{x}) = \int_Y u(t, \underline{x}, y)\, dy$, while infection is modulated by the infection rate $\beta(y)$ and contact with infected cells.

This model provides a continuous representation of tumour growth and infection evolution, capturing essential aspects of growth dynamics, therapeutic response, and the effects of hypoxia and epigenetic heterogeneity.

3.3 Transition from ABM to the continuous model

For the model we propose, it is possible to derive a continuous representation from the agent-based model, by using a scaling limit where the spatial (δ) and epigenetic (χ) parameters tend to zero. In this limit, transition probabilities of the discrete model are converted into diffusion and reaction terms in the continuous framework. The mean movement, epigenetic mutation, infection, and growth rates of the ABM, approximated as average fluxes, generate the respective spatial and epigenetic diffusion terms and reaction terms in the PDEs.
The transition process involves the following:

1. Spatial diffusion: discrete movement probabilities across grid points translate into a continuous spatial diffusion term, representing the mean movement of cell populations.

2. Epigenetic diffusion: changes in epigenetic traits translate into continuous epigenetic diffusion.

3. Infection and growth reaction terms: proliferation and infection rates, derived from averaging growth and infection probabilities, generate reaction terms in continuous equations.

This process yields a continuous representation of the average dynamics describing tumour growth, employing the fundamental structure of the ABM. Consequently, the resulting PDE model retains key properties of the agent-based model, such as spatial and epigenetic diffusion and mean interaction rates between infected and uninfected cells, leading to an effective description for studies, with a focus on large collections on cells.

3.3.1 The equations for the ABM

As mentioned previously, the main feature of the agent-based model is discretisation, which involves the following variables:

- Temporal: $t_n = \tau n$
- Spatial: $x_j = \delta j$
- Epigenetic: $y_k = \chi k$

The modelling approach and the resulting equations are developed under the assumption of a one-dimensional spatial setting, which allows for a more tractable yet representative analysis of the dynamics.

The number of cells, infected and uninfected, located at a specific point in the grid x_j at a given time step t_n is represented by discrete variables, respectively:

- Uninfected cells: $U^n_{j,k}$
  The density of uninfected cells is therefore:
$$u^n_{j,k} = \frac{U^n_{j,k}}{\delta\chi}$$
- Infected cells: I^n_j
  The density of infected cells is therefore:
$$i^n_j = \frac{I^n_j}{\delta}$$

Let us now recall the main features of the considered model: *movement*, *epigenetic mutation*, *growth and death*, and *infection*. The behaviour of cells in more detail is given by the following equations.

UNINFECTED CELLS

An uninfected cell with epigenetic trait y_k, located at x_j at time t_n, can:

1. **Move** to one of the adjacent positions $x_{j\pm1}$ with probability $\frac{\theta_u}{2}$.
   The number of cells will then be:
$$U^{n+1}_{j,k} = \frac{\theta_u}{2}U^n_{j-1,k} + \frac{\theta_u}{2}U^n_{j+1,k} + (1-\theta_u)U^n_{j,k}$$
   Dividing each term by $\delta\chi$, we obtain the density of uninfected cells:
$$u^{n+1}_{j,k} = \frac{\theta_u}{2}u^n_{j-1,k} + \frac{\theta_u}{2}u^n_{j+1,k} + (1-\theta_u)u^n_{j,k}$$

2. **Mutate** its epigenetic trait to $y_k \pm \frac{1}{\chi}$ with probability $\frac{\theta_y}{2}$.
   Keeping j fixed, we have:
$$U_{j,k}^{n+1} = \frac{\theta_y}{2} U_{j,k-1}^n + \frac{\theta_y}{2} U_{j,k+1}^n + (1-\theta_y) U_{j,k}^n$$
   Dividing each term by χ, we obtain the density of uninfected cells:
$$u_{j,k}^{n+1} = \frac{\theta_y}{2} u_{j,k-1}^n + \frac{\theta_y}{2} u_{j,k+1}^n + (1-\theta_y) u_{j,k}^n$$

3. **Proliferate** with probability $\tau G(\rho_j^n)_+$ and **die** with probability $\tau G(\rho_j^n)_-$, where:
$$G(y,\rho) = p\left(r(y) - \frac{\rho(t,\underline{x})}{K}\right)$$
   Here, $p > 0$ denotes proliferation rate, $r(y)$ is the growth rate of uninfected cells depending on the epigenetic state y, $\rho(t,\underline{x})$ represents the local pressure, and K is the carrying capacity. A summary table of all variables and parameters will be provided in the next chapter. Since only one of the two events can occur at a given time $t_n = \tau n$, we define a single rate as $\tau G(\rho_j^n)$. Thus, the number of uninfected cells becomes:
$$\begin{aligned} U_{j,k}^{n+1} &= U_{j,k}^n + \tau G(\rho_j^n) U_{j,k}^n \\ &= (1 + \tau G(\rho_j^n)) U_{j,k}^n \end{aligned}$$
   Dividing each term by $\delta\chi$, the resulting density is:
$$\begin{aligned} u_{j,k}^{n+1} &= u_{j,k}^n + \tau G(\rho_j^n) u_{j,k}^n \\ &= (1 + \tau G(\rho_j^n)) u_{j,k}^n \end{aligned}$$

4. **Become infected** through contact with infected cells, with probability $\tau\beta(y_k) i_j^n$, where $\beta(y)$ represents the infection rate of uninfected cells.
   The number of uninfected cells is:
$$\begin{aligned} U_{j,k}^{n+1} &= U_{j,k}^n - \tau\beta(y_k) i_j^n U_{j,k}^n \\ &= (1 - \tau\beta(y_k) i_j^n) U_{j,k}^n \end{aligned}$$
   and the corresponding density is thus given by:
$$\begin{aligned} u_{j,k}^{n+1} &= u_{j,k}^n - \tau\beta(y_k) i_j^n u_{j,k}^n \\ &= (1 - \tau\beta(y_k) i_j^n) u_{j,k}^n \end{aligned}$$

To construct the complete equation for uninfected cells, we consider in order: epigenetic mutation, movement, proliferation/death, and infection.
The full equation for the expected number of uninfected cells at time step t_{n+1} is:

$$\begin{aligned} U_{j,k}^{n+1} = \{&(1-\theta_y)\frac{\theta_u}{2}[1+\tau G(\rho_j^n)] U_{j-1,k}^n + \frac{\theta_y}{2}\frac{\theta_u}{2}[1+\tau G(\rho_j^n)](U_{j-1,k+1}^n + U_{j-1,k-1}^n) + \\ &+ (1-\theta_y)\frac{\theta_u}{2}[1+\tau G(\rho_j^n)] U_{j+1,k}^n + \frac{\theta_y}{2}\frac{\theta_u}{2}[1+\tau G(\rho_j^n)](U_{j+1,k+1}^n + U_{j+1,k-1}^n) + \\ &+ (1-\theta_y)(1-\theta_u)[1+\tau G(\rho_j^n)] U_{j,k}^n + \frac{\theta_y}{2}(1-\theta_u)(U_{j,k+1}^n + U_{j,k-1}^n)\}(1-\tau\beta(y_k) i_j^n) \end{aligned}$$

Dividing the above equation by $\delta\chi$, we obtain the equation for the density of uninfected cells:

$$\begin{aligned} u_{j,k}^{n+1} = \{&(1-\theta_y)\frac{\theta_u}{2}[1+\tau G(\rho_j^n)] u_{j-1,k}^n + \frac{\theta_y}{2}\frac{\theta_u}{2}[1+\tau G(\rho_j^n)](u_{j-1,k+1}^n + u_{j-1,k-1}^n) + \\ &+ (1-\theta_y)\frac{\theta_u}{2}[1+\tau G(\rho_j^n)] u_{j+1,k}^n + \frac{\theta_y}{2}\frac{\theta_u}{2}[1+\tau G(\rho_j^n)](u_{j+1,k+1}^n + u_{j+1,k-1}^n) + \\ &+ (1-\theta_y)(1-\theta_u)[1+\tau G(\rho_j^n)] u_{j,k}^n + \frac{\theta_y}{2}(1-\theta_u)(u_{j,k+1}^n + u_{j,k-1}^n)\}(1-\tau\beta(y_k) i_j^n) \end{aligned} \tag{3.1}$$

INFECTED CELLS

An infected cell located at position x_j at time t_n can:

1. **Move** to one of the two adjacent positions $x_{j\pm1}$ with probability $\frac{\theta_i}{2}$.
   The number of cells will then be:

   $$I_j^{n+1} = \frac{\theta_i}{2} I_{j-1}^n + \frac{\theta_i}{2} I_{j+1}^n + (1-\theta_i) I_j^n$$

   Dividing each term by δ, we obtain the density:

   $$i_j^{n+1} = \frac{\theta_i}{2} i_{j-1}^n + \frac{\theta_i}{2} i_{j+1}^n + (1-\theta_i) i_j^n$$

2. **Die** with probability τq, where $q > 0$ is a constant death rate.
   We therefore have:

   $$\begin{aligned} I_j^{n+1} &= I_j^n - \tau q I_j^n \\ &= (1-\tau q) I_j^n \end{aligned}$$

   Dividing each term by δ, we obtain the density:

   $$\begin{aligned} i_j^{n+1} &= i_j^n - \tau q i_j^n \\ &= (1-\tau q) i_j^n \end{aligned}$$

3. **Come into contact** with an uninfected cell.
   We must consider, for each position j, that infected cells can encounter uninfected cells with different phenotypes; therefore, the number of infected cells after contact is:

   $$I_j^{n+1} = I_j^n + \tau \sum_k \beta(y_k) U_{j,k}^n I_j^n$$

   Recalling the definitions of the densities for infected and uninfected cells, and dividing by δ, we obtain:

   $$i_j^{n+1} = i_j^n + \tau i_j^n \sum_k \beta(y_k) \chi u_{j,k}^n$$

The complete equation for the density of infected cells is:

$$\begin{aligned} i_j^{n+1} = &\frac{\theta_i}{2}(1-\tau q) i_{j-1}^n + \\ &+ \frac{\theta_i}{2}(1-\tau q) i_{j+1}^n + \\ &+ \tau i_j^n \sum_k \beta(y_k) \chi u_{j,k}^n \end{aligned} \tag{3.2}$$

3.3.2 Continuous Equations

Once the discrete equations for the density of infected and uninfected cells have been obtained, we can derive the corresponding continuous equations by carefully going to infinitesimal quantities.

INFECTED CELLS

$$
\begin{aligned}
i_j^{n+1} &= (1-\tau q)\left[\frac{\theta_i}{2}i_{j-1}^n + \frac{\theta_i}{2}i_{j+1}^n + (1-\theta_i)i_j^n\right] + \tau i_j^n \sum_k \beta(y_k)\chi u_{j,k}^n \\
&= \left(\frac{\theta_i}{2}i_{j-1}^n + \frac{\theta_i}{2}i_{j+1}^n + (1-\theta_i)i_j^n\right) - \tau q\left(\frac{\theta_i}{2}i_{j-1}^n + \frac{\theta_i}{2}i_{j+1}^n + (1-\theta_i)i_j^n\right) + \\
&+ \tau i_j^n \sum_k \beta(y_k)\chi u_{j,k}^n \\
&= \left[i_j^n + \theta_i \frac{i_{j-1}^n + i_{j+1}^n - 2i_j^n}{2}\right] - \tau q\frac{\theta_i}{2}i_{j-1}^n - \tau q\frac{\theta_i}{2}i_{j+1}^n - \tau q i_j^n + \tau q\theta_i i_j^n + \\
&+ \tau i_j^n \sum_k \beta(y_k)\chi u_{j,k}^n
\end{aligned}
$$

Dividing both sides by τ and rearranging terms, we obtain:

$$
\begin{aligned}
\frac{i_j^{n+1} - i_j^n}{\tau} &= \theta_i \frac{i_{j-1}^n + i_{j+1}^n - 2i_j^n}{2\tau} - q\frac{\theta_i}{2}i_{j-1}^n - q\frac{\theta_i}{2}i_{j+1}^n - q i_j^n + q\theta_i i_j^n + i_j^n \sum_k \beta(y_k)\chi u_{j,k}^n \\
&= \theta_i \frac{\delta^2}{2\tau}\frac{i_{j-1}^n + i_{j+1}^n - 2i_j^n}{\delta^2} - q i_j^n - q\frac{\theta_i}{2}\delta^2\left(\frac{i_{j-1}^n + i_{j+1}^n - 2i_j^n}{\delta^2}\right) + i_j^n \sum_k \beta(y_k)\chi u_{j,k}^n
\end{aligned}
$$

In the continuous limit, as $\tau \to 0$, the left-hand side approximates the time derivative:

$$\frac{i_j^{n+1} - i_j^n}{\tau} \to \partial_t i(t,x),$$

assuming that the function i is smooth in time. Similarly, the spatial finite difference becomes a second spatial derivative:

$$\frac{i_{j-1}^n + i_{j+1}^n - 2i_j^n}{\delta^2} \to \partial_{xx} i(t,x),$$

as $\delta^2 \to 0$, and under the standard scaling condition $\frac{\delta^2}{2\tau} \to D$, we recover a diffusive term with diffusion coefficient D.
Furthermore, the epigenetic variable y, initially discretized as $y_k = \chi k$, becomes continuous in the limit $\chi \to 0$. The sum over k,

$$\sum_k \beta(y_k)\chi u(t_n, x_j, y_k),$$

is a Riemann sum and thus converges to the integral

$$\int_Y \beta(y)u(t,x,y)\,dy,$$

provided that u and β are sufficiently regular functions.
Putting everything together, we obtain the continuous equation:

$$\partial_t i(t,\underline{x}) = \theta_i D\Delta_x i(t,\underline{x}) + i(t,\underline{x})\int_Y \beta(y)u(t,\underline{x},y)dy - qi(t,\underline{x})$$

Finally, by defining $\theta_i D = D_x$, the final continuous equation for infected cells becomes:

$$\partial_t i(t,\underline{x}) = D_x\Delta_x i(t,\underline{x}) + i(t,\underline{x})\int_Y \beta(y)u(t,\underline{x},y)dy - qi(t,\underline{x})$$

UNINFECTED CELLS

We now return to the discrete description of uninfected cells and derive the corresponding continuous equation. Unlike the infected population, for which a more direct discretisation of the diffusion-reaction equation has been used, here we adopt a bottom-up probabilistic approach. This leads to the following update rule for $u_{j,k}^{n+1}$, describing the expected number of uninfected cells at time t_{n+1}, spatial location x_j, and epigenetic level y_k:

$$
\begin{aligned}
u_{j,k}^{n+1} = \Bigg\{ & (1-\theta_y)\frac{\theta_u}{2}[1+\tau G(\rho_j^n)]u_{j-1,k}^n + \frac{\theta_y}{2}\frac{\theta_u}{2}[1+\tau G(\rho_j^n)](u_{j-1,k+1}^n + u_{j-1,k-1}^n) + \\
& + (1-\theta_y)\frac{\theta_u}{2}[1+\tau G(\rho_j^n)]u_{j+1,k}^n + \frac{\theta_y}{2}\frac{\theta_u}{2}[1+\tau G(\rho_j^n)](u_{j+1,k+1}^n + u_{j+1,k-1}^n) + \\
& + (1-\theta_y)(1-\theta_u)[1+\tau G(\rho_j^n)]u_{j,k}^n + \frac{\theta_y}{2}(1-\theta_u)(u_{j,k+1}^n + u_{j,k-1}^n)\}(1-\tau\beta(y_k)i_j^n) \\
= \{ & u_{j-1,k}^n[(1-\theta_y)\frac{\theta_u}{2}(1+\tau G(\rho_j^n))] + u_{j-1,k+1}^n[\frac{\theta_y}{2}\frac{\theta_u}{2}(1+\tau G(\rho_j^n))] \\
& + u_{j-1,k-1}^n[\frac{\theta_y}{2}\frac{\theta_u}{2}(1+\tau G(\rho_j^n))] + u_{j+1,k}[(1-\theta_y)\frac{\theta_u}{2}(1+\tau G(\rho_j^n))] \\
& + u_{j+1,k+1}^n[\frac{\theta_y}{2}\frac{\theta_u}{2}(1+\tau G(\rho_j^n))] + u_{j+1,k-1}^n[\frac{\theta_y}{2}\frac{\theta_u}{2}(1+\tau G(\rho_j^n))] \\
& + u_{j,k}^n[(1-\theta_y)(1-\theta_u)(1+\tau G(\rho_j^n))] + u_{j,k+1}^n[\frac{\theta_y}{2}(1-\theta_u)(1+\tau G(\rho_j^n))] \\
& + u_{j,k-1}^n[\frac{\theta_y}{2}(1-\theta_u)(1+\tau G(\rho_j^n))]\Bigg\}(1-\tau\beta(y_k)i_j^n)
\end{aligned}
$$

For sufficiently small values of τ, δ, and χ, we can apply the following approximations:

$$
\begin{gathered}
u_{j,k}^n \approx u(t,\underline{x},y), \quad u_{j,k}^{n+1} \approx u(t+\tau,\underline{x},y), \quad i_j^n \approx i(t,\underline{x}) \\
u_{j\pm1,k}^n \approx u(t,\underline{x}\pm\delta,y), \quad u_{j,k\pm1}^n \approx u(t,\underline{x},y\pm\chi), \quad \beta(y_k) \approx \beta(y)
\end{gathered}
$$

So that the expression above becomes:

$$
\begin{aligned}
u(t+\tau,\underline{x},y) = \{ & u(t,x-\delta,y)[(1-\theta_y)\frac{\theta_u}{2}(1+\tau G)] + \\
& + u(t,x-\delta,y+\chi)[\frac{\theta_y}{2}\frac{\theta_u}{2}(1+\tau G)] + \\
& + u(t,x-\delta,y-\chi)[\frac{\theta_y}{2}\frac{\theta_u}{2}(1+\tau G)] + \\
& + u(t,x+\delta,y)[(1-\theta_y)\frac{\theta_u}{2}(1+\tau G)] + \\
& + u(t,x+\delta,y+\chi)[\frac{\theta_y}{2}\frac{\theta_u}{2}(1+\tau G)] + \\
& + u(t,x+\delta,y-\chi)[\frac{\theta_y}{2}\frac{\theta_u}{2}(1+\tau G)] + \\
& + u(t,x,y)[(1-\theta_y)(1-\theta_u)(1+\tau G)] + \\
& + u(t,x,y+\chi)[\frac{\theta_y}{2}(1-\theta_u)(1+\tau G)] + \\
& + u(t,x,y-\chi)[\frac{\theta_y}{2}(1-\theta_u)(1+\tau G)]\}(1-\tau\beta i(t,\underline{x}))
\end{aligned}
$$

To transition from the discrete update rule to a continuous partial differential equation, we apply a second-order Taylor expansion to the function $u(t,\underline{x},y)$ around the point $(\underline{x},y)$, assuming sufficient regularity and smoothness. Specifically:

$$
\begin{aligned}
u(t, \underline{x}, y \pm \chi) &= u \pm \chi \frac{\partial u}{\partial y} + \frac{\chi^2}{2} \frac{\partial^2 u}{\partial y^2} \\
u(t, \underline{x} \pm \delta, y) &= u \pm \delta \frac{\partial u}{\partial x} + \frac{\delta^2}{2} \frac{\partial^2 u}{\partial x^2} \\
u(t, \underline{x} + \delta, y \pm \chi) &= u + \delta \frac{\partial u}{\partial x} \pm \chi \frac{\partial u}{\partial y} + \frac{\delta^2}{2} \frac{\partial^2 u}{\partial x^2} + \frac{\chi^2}{2} \frac{\partial^2 u}{\partial y^2} \pm \delta\chi \frac{\partial^2 u}{\partial x \partial y} \\
u(t, \underline{x} - \delta, y \pm \chi) &= u - \delta \frac{\partial u}{\partial x} \pm \chi \frac{\partial u}{\partial y} + \frac{\delta^2}{2} \frac{\partial^2 u}{\partial x^2} + \frac{\chi^2}{2} \frac{\partial^2 u}{\partial y^2} \mp \delta\chi \frac{\partial^2 u}{\partial x \partial y}
\end{aligned}
$$

where we use the notation $u(t, \underline{x}, y) \equiv u$.
These approximations allow us to identify diffusion terms in both the spatial and epigenetic variables, which will appear in the limit as $\delta, \chi \to 0$.

Therefore, we can write the previous expression as:

$$
\begin{aligned}
u(t+\tau, \underline{x}, y) = \Bigg\{ & (u - \delta \frac{\partial u}{\partial x} + \frac{\delta^2}{2} \frac{\partial^2 u}{\partial x^2})[(1-\theta_y)\frac{\theta_u}{2}(1+\tau G)] + \\
& + (u - \delta \frac{\partial u}{\partial x} + \chi \frac{\partial u}{\partial y} + \frac{\delta^2}{2} \frac{\partial^2 u}{\partial x^2} + \frac{\chi^2}{2} \frac{\partial^2 u}{\partial y^2} + \frac{\chi^2}{2} \frac{\partial^2 u}{\partial y^2} - \delta\chi \frac{\partial^2 u}{\partial x \partial y})[\frac{\theta_y}{2}\frac{\theta_u}{2}(1+\tau G)] + \\
& + (u - \delta \frac{\partial u}{\partial x} - \chi \frac{\partial u}{\partial y} + \frac{\delta^2}{2} \frac{\partial^2 u}{\partial x^2} + \frac{\chi^2}{2} \frac{\partial^2 u}{\partial y^2} + \frac{\chi^2}{2} \frac{\partial^2 u}{\partial y^2} + \delta\chi \frac{\partial^2 u}{\partial x \partial y})[\frac{\theta_y}{2}\frac{\theta_u}{2}(1+\tau G)] + \\
& + (u + \delta \frac{\partial u}{\partial x} + \frac{\delta^2}{2} \frac{\partial^2 u}{\partial x^2})[(1-\theta_y)\frac{\theta_u}{2}(1+\tau G)] + \\
& + (u + \delta \frac{\partial u}{\partial x} + \chi \frac{\partial u}{\partial y} + \frac{\delta^2}{2} \frac{\partial^2 u}{\partial x^2} + \frac{\chi^2}{2} \frac{\partial^2 u}{\partial y^2} + \frac{\chi^2}{2} \frac{\partial^2 u}{\partial y^2} + \delta\chi \frac{\partial^2 u}{\partial x \partial y})[\frac{\theta_y}{2}\frac{\theta_u}{2}(1+\tau G)] + \\
& + (u + \delta \frac{\partial u}{\partial x} - \chi \frac{\partial u}{\partial y} + \frac{\delta^2}{2} \frac{\partial^2 u}{\partial x^2} + \frac{\chi^2}{2} \frac{\partial^2 u}{\partial y^2} + \frac{\chi^2}{2} \frac{\partial^2 u}{\partial y^2} - \delta\chi \frac{\partial^2 u}{\partial x \partial y})[\frac{\theta_y}{2}\frac{\theta_u}{2}(1+\tau G)] + \\
& + u[(1-\theta_y)(1-\theta_u)(1+\tau G)] + \\
& + (u + \chi \frac{\partial u}{\partial y} + \frac{\chi^2}{2} \frac{\partial^2 u}{\partial y^2})[\frac{\theta_y}{2}(1-\theta_u)(1+\tau G)] + \\
& + (u - \chi \frac{\partial u}{\partial y} + \frac{\chi^2}{2} \frac{\partial^2 u}{\partial y^2})[\frac{\theta_y}{2}(1-\theta_u)(1+\tau G)] \Bigg\} (1 - \tau\beta(y) i(t, \underline{x}))
\end{aligned}
$$

Simplifying and collecting terms, we obtain:

$$
\begin{aligned}
u(t+\tau,\underline{x},y) = \Bigg\{ & 2u[(1-\theta_y)\frac{\theta_u}{2}(1+\tau G)] + \delta^2\frac{\partial^2 u}{\partial x^2}[(1-\theta_y)\frac{\theta_u}{2}(1+\tau G)]+ \\
& + 4u[\frac{\theta_y}{2}\frac{\theta_u}{2}(1+\tau G)] - 2\delta\frac{\partial u}{\partial x}[\frac{\theta_y}{2}\frac{\theta_u}{2}(1+\tau G)]+ \\
& + \delta^2\frac{\partial^2 u}{\partial x^2}[\frac{\theta_y}{2}\frac{\theta_u}{2}(1+\tau G)] + \chi^2\frac{\partial^2 u}{\partial y^2}[\frac{\theta_y}{2}\frac{\theta_u}{2}(1+\tau G)]+ \\
& + 2\delta\frac{\partial u}{\partial x}[\frac{\theta_y}{2}\frac{\theta_u}{2}(1+\tau G)] + \delta^2\frac{\partial^2 u}{\partial x^2}[\frac{\theta_y}{2}\frac{\theta_u}{2}(1+\tau G)]+ \\
& + \chi^2\frac{\partial^2 u}{\partial y^2}[\frac{\theta_y}{2}\frac{\theta_u}{2}(1+\tau G)] + u[(1-\theta_y)(1-\theta_u)(1+\tau G)]+ \\
& + 2u[\frac{\theta_y}{2}(1-\theta_u)(1+\tau G)] + \chi^2\frac{\partial^2 u}{\partial y^2}[\frac{\theta_y}{2}(1-\theta_u)(1+\tau G)]\Bigg\}(1-\tau\beta(y)i(t,\underline{x}))
\end{aligned}
$$

We now collect the coefficients of terms involving the same derivatives and obtain three equalities, i.e.:

1. $2u[(1-\theta_y)\frac{\theta_u}{2}(1+\tau G)] + 4u[\frac{\theta_y}{2}\frac{\theta_u}{2}(1+\tau G)] + u[(1-\theta_y)(1-\theta_u)(1+\tau G)] + 2u[\frac{\theta_y}{2}(1-\theta_u)(1+\tau G)] = u(1+\tau G)$

2. $\delta^2\frac{\partial^2 u}{\partial x^2}[(1-\theta_y)\frac{\theta_u}{2}(1+\tau G)] + 2\delta\frac{\partial u}{\partial x}[\frac{\theta_y}{2}\frac{\theta_u}{2}(1+\tau G)] = \frac{\delta^2}{2}\frac{\partial^2 u}{\partial x^2}\theta_u(1+\tau G)$

3. $2\chi^2\frac{\partial^2 u}{\partial y^2}[\frac{\theta_y}{2}\frac{\theta_u}{2}(1+\tau G)] + \chi^2\frac{\partial^2 u}{\partial y^2}[\frac{\theta_y}{2}(1-\theta_u)(1+\tau G)] = \frac{\chi^2}{2}\frac{\partial^2 u}{\partial y^2}\theta_y(1+\tau G)$

We can thus simplify as follows:

$$
\begin{aligned}
u(t+\tau,\underline{x},y) &= \Bigg\{u[1+\tau G] + \frac{\delta^2}{2}\frac{\partial^2 u}{\partial x^2}(\theta_u[1+\tau G]) + \frac{\chi^2}{2}\frac{\partial^2 u}{\partial y^2}(\theta_y[1+\tau G])\Bigg\}(1-\tau\beta(y)i(t,\underline{x})) \\
&= u(1+\tau G) + \frac{\delta^2}{2}\frac{\partial^2 u}{\partial x^2}\theta_u(1+\tau G) + \frac{\chi^2}{2}\frac{\partial^2 u}{\partial y^2}\theta_y(1+\tau G)+ \\
&- \tau\beta iu(1+\tau G) - \tau\beta i\frac{\delta^2}{2}\frac{\partial^2 u}{\partial x^2}\theta_u(1+\tau G) - \tau\beta i\frac{\chi^2}{2}\frac{\partial^2 u}{\partial y^2}\theta_y(1+\tau G) \\
&= u + u\tau G + \frac{\delta^2}{2}\frac{\partial^2 u}{\partial x^2}\theta_u + \frac{\delta^2}{2}\frac{\partial^2 u}{\partial x^2}\theta_u\tau G + \frac{\chi^2}{2}\frac{\partial^2 u}{\partial y^2}\theta_y+ \\
&+ \frac{\chi^2}{2}\frac{\partial^2 u}{\partial y^2}\theta_y\tau G - \tau G - \tau\beta iu - \beta iu\tau^2 G - \tau\beta i\frac{\delta^2}{2}\frac{\partial^2 u}{\partial x^2}\theta_u+ \\
&- \beta i\frac{\delta^2}{2}\frac{\partial^2 u}{\partial x^2}\theta_u\tau^2 G - \tau\beta i\frac{\chi^2}{2}\frac{\partial^2 u}{\partial y^2}\theta_y - \beta i\frac{\chi^2}{2}\frac{\partial^2 u}{\partial y^2}\theta_y\tau^2 G
\end{aligned}
$$

Dividing both sides by τ and rearranging terms, we obtain:

$$\begin{aligned}\frac{u(t+\tau,\underline{x},y)-u}{\tau} &= uG+\frac{\theta_u\delta^2}{2\tau}\frac{\partial^2 u}{\partial x^2}+\frac{\theta_u\delta^2}{2}\frac{\partial^2 u}{\partial x^2}G+\frac{\theta_y\chi^2}{2\tau}\frac{\partial^2 u}{\partial y^2}+\\ &+\frac{\theta_y\chi^2}{2}\frac{\partial^2 u}{\partial y^2}G-\beta iu-\tau\beta iuG-\beta i\frac{\theta_u\delta^2}{2}\frac{\partial^2 u}{\partial x^2}+\\ &-\beta i\tau\frac{\theta_u\delta^2}{2}\frac{\partial^2 u}{\partial x^2}G-\beta i\frac{\theta_y\chi^2}{2}\frac{\partial^2 u}{\partial y^2}-\beta i\frac{\theta_y\chi^2}{2}\frac{\partial^2 u}{\partial y^2}G\end{aligned}$$

For $\delta\to 0,\quad \chi\to 0,\quad \tau\to 0,\quad \frac{\delta^2}{2\tau}\to D,\quad \frac{\chi^2}{2\tau}\to D$ we obtain that

$$\frac{\partial u}{\partial t}(t,\underline{x},y)=p\left(r(y)-\frac{\rho(t,\underline{x})}{k}\right)u(t,\underline{x},y)+D\theta_u\frac{\partial^2 u}{\partial x^2}+D\theta_y\frac{\partial^2 u}{\partial y^2}-\beta iu$$

By defining $D\theta_y\equiv D_y$ and $D\theta_u\equiv D_x$, the equation becomes:

$$\begin{aligned}\frac{\partial u}{\partial t}(t,\underline{x},y) &= D_x\frac{\partial^2 u}{\partial x^2}+D_y\frac{\partial^2 u}{\partial y^2}+p\left(r(y)-\frac{\rho(t,\underline{x})}{k}\right)u(t,\underline{x},y)-\beta iu\\ &= D_x\Delta_x u(t,\underline{x},y)+D_y\Delta_y u(t,\underline{x},y)+p\left(r(y)-\frac{\rho(t,\underline{x})}{k}\right)u(t,\underline{x},y)+\\ &-\beta(y)u(t,\underline{x},y)i(t,\underline{x})\end{aligned}$$

Therefore, the resulting continuous model is the following:

$$\begin{cases}\partial_t u(t,x,y)=D_y\Delta_y u(t,x,y)+D_x\Delta_x u(t,x,y)+p\left(r(y)-\frac{\rho(t,x)}{K}\right)u(t,x,y)+\\ \qquad\qquad -\beta(y)\ u(t,x,y)\ i(t,x)\\ \partial_t i(t,x)=D_x\Delta_x i(t,x)+i(t,x)\int_Y\beta(y)u(t,x,y)dy-qi(t,x)\\ \rho(t,x)\coloneqq\int_Y u(t,x,y)dy+i(t,x)\end{cases}\tag{3.3}$$

where:

- $D_x=\theta_u D$ is the spatial diffusion coefficient.
- $D_y=\theta_y D$ is the epigenetic diffusion coefficient.
- $r(y)$ is the proliferation rate dependent on the epigenetic state.
- $\beta(y)$ is the infectivity of uninfected cells as a function of their epigenetic state y
- $\rho(t,x)=\int_Y u(t,x,y)dy$ is the local total density of uninfected cells.

This system is the same studied in **Lorenzi et al.** [11], with the addition of spatial dynamics. We may expect that a travelling wave originates from the system: in the center, the cell densities reach the steady state predicted in absence of spatial dynamics (although the spatial diffusion may have some effects on that), while at the front there is a prevalence of cells with epigenetic variable close to 0.
We define $r(y)$ and $\beta(y)$ as

$$r(y)\coloneqq 1-\eta y^2\qquad \beta(y)\coloneqq\beta_1+\zeta(1-y^2)$$

In the next chapter, we will show a number of results employing the discrete and continuous modelling discussed here.

Chapter 4

Simulations in one spatial dimension

This chapter presents the initial results obtained from simulations of the interaction between tumour cells and therapies based on oncolytic viruses, with a particular focus on the effects of epigenetic variability. Two main modelling approaches are used: a continuous model based on partial differential equations (PDE) in Eq. (3.3) and a discrete agent-based model (ABM) in Eq. (3.3.1) for infected cells and in Eq. (3.1) for uninfected cells. Both models aim to describe the evolution of infected cells (oncolytic viruses) and uninfected tumour cells.

In this chapter, all simulations are performed in a one-dimensional spatial setting. The analysis is structured into four distinct parts.

In the first part, a brief overview of the working context and the parameters used is provided. In addition, a so-called reference simulation is described, which includes both infected and uninfected cells simulated in both models.

In the second part, two important concepts are introduced: the cellular average and the epigenetic average, which are essential to understand the evolution of cell populations over time. The goal is to compare the two approaches and assess the impact of epigenetic variability on tumour cell behaviour, highlighting the similarities and differences between the deterministic PDE and the stochastic ABM.

In the third part, the propagation of infected and uninfected cells is studied in three distinct configurations, characterised by different initial conditions for the distribution of infected cells. The goal is to assess how these variations influence the dynamics of infection and its impact on the uninfected population. In particular, three sets of initial conditions with different radii and initial concentrations of infected cells are considered, whereas the uninfected cells maintain a constant standard configuration. The simulations allow for comparison of the evolutions of the two models and help clarify the role of initial settings in determining infection spread.

Finally, in the fourth part of the chapter, we investigate the importance of epigenetics in cell behaviour and interactions by varying two key parameters of our study, both of which influence the behaviour of uninfected cells: η, which appears in the definition of growth rate, and ζ, which affects the infection rate. Specifically, the growth rate is modeled as $r(y) := 1 - \eta y^2$, where η modulates the selective pressure exerted on different epigenetic phenotypes, penalising cells further from the neutral state $y = 0$. A higher η leads to a stronger reduction in proliferation for extreme phenotypes. Similarly, the infection rate is given by $\beta(y) := \beta_1 + \zeta(1 - y^2)$, where ζ determines the extent to which susceptibility to infection depends on the epigenetic state. When $\zeta > 0$, cells with phenotypes closer to $y = 0$ are more susceptible to infection. These two parameters thus encapsulate how epigenetic heterogeneity can influence both cell proliferation and vulnerability to oncolytic viruses.

The main objective is to analyse several key aspects in the study of tumour dynamics, with particular focus on infected and uninfected cells, and the influence of the epigenetic variable. Numerical solutions from both approaches are compared to better understand the observed behaviours.

4.1 Description of the initial setting and parameters

In the model, the response to therapy is studied by simulating the infection of tumour cells by oncolytic viruses. Each cell can be infected or uninfected, the latter also being influenced by an epigenetic variable y, that modulates proliferation and susceptibility to infection.

Main parameters

Parameter	Meaning	Value
D_u	Diffusion coefficient for uninfected cells	2.35×10^{-3} (mm^2/h)
D_i	Diffusion coefficient for infected cells	2.35×10^{-3} (mm^2/h)
D_y	Epigenetic diffusion coefficient	5×10^{-6} (mm^2/h)
R_u	Initial radius of uninfected cells	2.6 (mm)
R_i	Initial radius of infected cells	1 (mm)
$\beta(y)$	Infection rate of uninfected cells	Defined by β_1 and ζ (h^{-1})
$r(y)$	Growth rate of uninfected cells	Defined by η
η	Epigenetic constant	0.5
ζ	Infection rate coefficient	2×10^{-4}
K	Carrying capacity	1000 (cells/mm)
p	Proliferation rate of uninfected cells	ln(2)/37 (h^{-1})
q	Death rate of infected cells	1/24 (h^{-1})
α	Viruses released per cell	3500

Table 4.1: Parameters used for the simulation.

Initial and boundary conditions

For the initial conditions, we define the initial density of infected and uninfected cells within regions defined by radii R_u and R_i (in mm). The boundary conditions impose zero diffusion at the spatial domain edges for both uninfected and infected cells.

For uninfected cells $u(x, y, t)$:

$$\frac{\partial u(x,y,t)}{\partial x}\Big|_{\text{boundary}} = 0, \quad \frac{\partial u(x,y,t)}{\partial y}\Big|_{\text{boundary}} = 0$$

For infected cells $i(x, t)$:

$$\frac{\partial i(x,t)}{\partial x}\Big|_{\text{boundary}} = 0$$

These boundary conditions ensure that cells do not move out of the spatial domain and that there is no flux at the edges, maintaining the cell populations within the specified domain during simulation.

Additional variables for the study

In addition to the primary model parameters, we introduce two key variables to better understand the behaviour of the system:

- The **cell average**, representing the mean density of infected and uninfected cells over time, obtained by averaging five independent simulations in the ABM model. This helps reduce stochastic fluctuations and allows for a more consistent comparison with the PDE model, which describes the evolution of the cell population in a deterministic way.

- The **epigenetic average** (for uninfected cells), providing a measure of the distribution of epigenetic states within the uninfected cell population. This allows us to assess the influence of epigenetic variability on proliferation and infection, considering that infected cells do not depend on the epigenetic variable.

  The epigenetic average $\mu(x,t)$ is calculated as:

  $$\mu(x,t) = \frac{\int_Y yu(x,y,t)dy}{\int_Y u(x,y,t)dy}$$

  where y represents the epigenetic state and $u(x,y,t)$ is the density of uninfected cells in the epigenetic space. The numerator corresponds to the weighted sum of the epigenetic states, and the denominator normalizes by the total number of uninfected cells at location x. In other words, $\mu(x,t)$ represents a local average epigenetic state within the population.

Analysis of simulations

This section describes the numerical simulations carried out to investigate the models proposed in this thesis. The adopted approach combined advanced computational tools, including the use of *MATLAB* for the development and verification of model prototypes, and high performance computing (HPC) resources via a *supercomputer*, to perform large-scale simulations and obtain results with greater precision and computational complexity.

The integration of these tools enabled parametric analyses, assessment of model robustness and simulation of realistic scenarios that require significant computational time. Throughout the chapter, methodological details, simulation configurations, and the results obtained are presented.

4.2 Introduction to the work

As said, the comparison between the agent-based model (ABM) and the continuous model based on partial differential equations (PDE) allows the evaluation of the differences and strengths of both approaches.

The analysis considers infected and uninfected cells, including the average of the cell distribution and the epigenetic average, treated in a unified manner to describe full temporal evolution. The following figures show the initial conditions of the models under analysis.

In this initial phase of the analysis, let us focus on the initial configuration of the system, considering the distribution of infected and uninfected cells in the PDE model, the average in the ABM model, and the epigenetic mean of uninfected cells, computed for both. The goal is to understand how these initial conditions influence the evolution of the cell population and

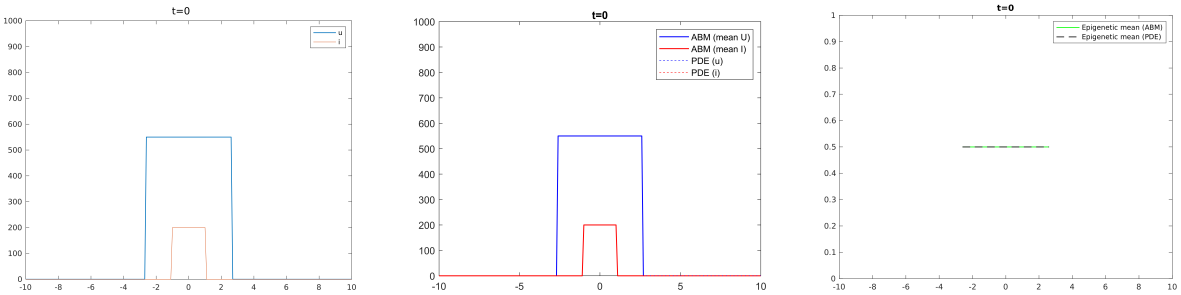

(a) PDE Model (b) ABM Average (c) Epigenetic Mean

Figure 4.1: Initial simulation configuration in the three main representations. (a) Initial distribution of infected and uninfected cells in the PDE model, with a central region containing the infection. (b) Average from five independent simulations in the ABM model, used to reduce local variability and to compare the behaviour with the PDE model. (c) Epigenetic mean of uninfected cells, which represents the initial variability in epigenetic states and provides a measure of cellular heterogeneity. Note that, at the beginning, configurations (a) and (b) are identical; differences will emerge over time.

the spread of infection over time.

As shown in Figure 4.1, the system initially presents a uniform distribution of uninfected cells across the domain, while a central region contains an initial population of infected cells. This configuration reflects an ideal situation where the infection due to the oncolitic virus has just been introduced and is in its early stage of expansion. For example, this can idealise an injection of the virus at the "centre" of the tumour in one dimension. The first image (Figure 4.1a) shows this initial condition in the PDE model, where the spatial distribution of the cells is continuous and follows a regular pattern.

Next to this, the central panel shows the average in the ABM model, obtained from five independent simulations of the discrete agent-based model. Since the ABM introduces stochastic variability, using the average provides a more stable and comparable picture with respect to the PDE model: since no simulation has yet been considered and as shown in Figure 4.1b, the initial configuration of the tumour features a compact mass of uninfected cells (in blue), while the presence of infected cells (in red) is limited to a small central region, indicating that the infection has just entered the system. At this early stage, consistency between the two models can be observed, but as time flows we will notice discrepancies between the two models.

Finally, the third panel (Figure 4.1c) shows the epigenetic mean of the uninfected cells, a key parameter to assess the epigenetic response of the cell population to infection. At this stage, two curves (solid green for the ABM model, dashed black for the PDE) overlap and align in the central region, given that the epigenetic mean is initially constant. This suggests that, in this early phase, the distribution of epigenetic states among uninfected cells is homogeneous, and no significant selection or differentiation effects are yet present. Again, at the start, the models show identical states.

The joint analysis of these three representations provides a solid foundation for understanding the dynamics of infection diffusion and the evolution of populations. The PDE model offers a continuous description of the infection, the ABM and its average provide a more detailed view of local fluctuations, and the epigenetic mean allows for evaluating the role of epigenetic variability in the process.

4.2.1 Comparison between the two models

Before analysing the temporal evolution of the parameters under investigation, it is useful to highlight the similarities and differences between the two models considered. To do this, we examine two reference simulations: in both cases, both infected and uninfected cells are included, but with a difference in how the results are visualised. In the first simulation, the focus is on the distribution of uninfected cells, which are plotted separately to emphasise their behaviour in the two models. In the second simulation, infected cells are also plotted, allowing a direct comparison of the evolution of the two cell populations in both models.

Behaviour of uninfected cells

To validate the comparison between the PDE model and the ABM, we analysed the evolution of the density of uninfected cells in a reference simulation, corresponding to a time length of $T_{pde} = 1500h$.

At the beginning of the simulation, the uninfected cells are uniformly distributed around the central region. This initial distribution is used as the starting condition for both the agent-based model (solid line) and the PDE model (dashed line): both show a concentration of uninfected cells around the central area of the spatial domain x, defined by the radius R_u, with a symmetric and well-defined profile.

As time progresses, uninfected cells spread toward the peripheral regions of the domain, following a dynamic governed by diffusion and its coefficient D_u. It is observed that the PDE model produces an extremely smooth and regular curve, whereas the ABM introduces local fluctuations because of its stochastic and discrete nature. These variations are more pronounced in the peripheral areas of the domain, where cell density is lower and discrete effects become dominant. Both models show a gradual reduction in cell density, because of the impact of infection.

At later time points, the system appears to approach a more stable configuration. The distribution of uninfected cells in the agent-based model is observed to maintain local oscillations, whereas the PDE model displays a smoother, diffuse profile, with several local minima and maxima.

For an in-depth analysis, three corresponding frames are extracted at time points $t = 400h$, $t = 750h$, and $t = 1000h$.

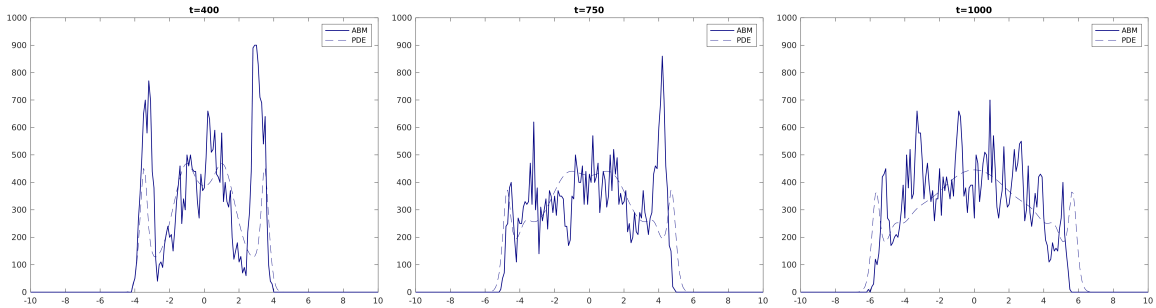

Figure 4.2: Temporal evolution of the distribution of uninfected cells: we observe the onset of fragmentation in the cell distribution, where the agent-based model shows a more irregular behaviour compared to the PDE model. Note partial stabilisation of the system, with visible differences between the two approaches, as time progresses.

As shown in the first frame, at time $t = 400h$, two distinct large peaks appear in the agent-based model, while the PDE model shows a smoother and more continuous curve. Lo-

cal oscillations in the centre of the ABM profile are evident.

In the second frame, at time $t = 750h$, the density of uninfected cells begins to fragment further. The PDE model continues to show a smooth distribution, whereas the agent-based model exhibits more pronounced local variations, with sharper peaks forming in certain regions and a large excursion at one of the two edges of the profile.

In the final frame, at time $t = 1000h$, the density of uninfected cells appears more dispersed. The PDE model still provides a good, smooth approximation to the agent-based model, which is still characterised by a series of peaks and local fluctuations, resulting in a more irregular distribution over time.

The comparative analysis of the two models highlights differences and similarities in the propagation of the infection.

Main differences between the two models are given by:

- **Homogeneity of diffusion**: the PDE model produces a more uniform spread of infection compared to the ABM.
- **Stochastic effects**: the ABM introduces spatial variability, with some regions being infected faster than others.
- **Population structure**: the ABM shows local fluctuations, whereas the PDE model follows a continuous distribution.

Despite these differences, both models exhibit qualitatively similar behaviour in the spread of infection: in both the PDE and the ABM, the infection propagates from the initially central region toward the surrounding areas, and both models show similar increase in the number of infected cells over time. In addition, in both cases, the majority of uninfected cells are eventually infected in the later stages. Further, speeds of propagations for infections appear comparable, but we will discuss differences shortly.

This first and (perhaps) simplistic simulation is nonetheless fundamental for validating the proposed model: the behaviour of uninfected cells observed in the continuous dynamics is consistent with that seen in the discrete dynamics, demonstrating the robustness of the approach.

To obtain consistent results, the analysis can be extended by increasing the observation time or the number of simulations.

1. Increasing the observation time With $T_{pde} = 10000h$, the system shows higher cell density in specific regions, suggesting that it is evolving toward a partially stable configuration (see Fig. 4.3, left and centre). These panels illustrate how, over time, cell populations tend to concentrate in well-defined zones, hinting at the emergence of structured spatial patterns.

2. Increasing the number of simulations Considering ten distinct simulations for the discrete model (instead of the previous five), more complex dynamics emerge, with competition and cooperation among cells, leading to a heterogeneous distribution with densely populated and nearly empty zones (see Fig. 4.3, right). This behaviour reflects the influence of stochastic variability and local interactions on the spatial organisation of the system.

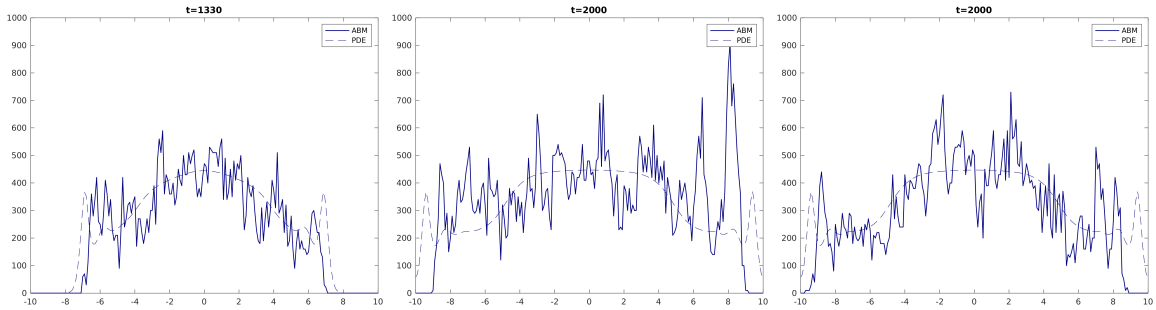

Figure 4.3: Temporal evolution of uninfected cells: left and centre, variations in cell density with increased observation time; right, spatial competition in a multi-simulation scenario.

These results highlight how interaction between different tumour cell populations can significantly influence the overall dynamics, suggesting that increasing complexity may require different therapeutic strategies compared to simpler and homogeneous systems.

Behaviour of infected and uninfected cells

The analysis of the temporal evolution of the distribution of infected and uninfected cells in the two models, PDE and ABM, highlights similarities and differences in how the infection spreads across the domain. As shown in Figures 4.4 and 4.5, both models describe a progressive spread of infection, with the infected population expanding over time.

In the PDE model, as shown in Figure 4.4, the infection spreads uniformly and continuously, generating a regular and symmetric front that expands outward from the central region. As a result, the density of infected cells increases progressively and gradually, reaching an almost homogeneous distribution in the later stages of the simulation. Note also how the centre of the profile for u flattens and reaches a plateau.

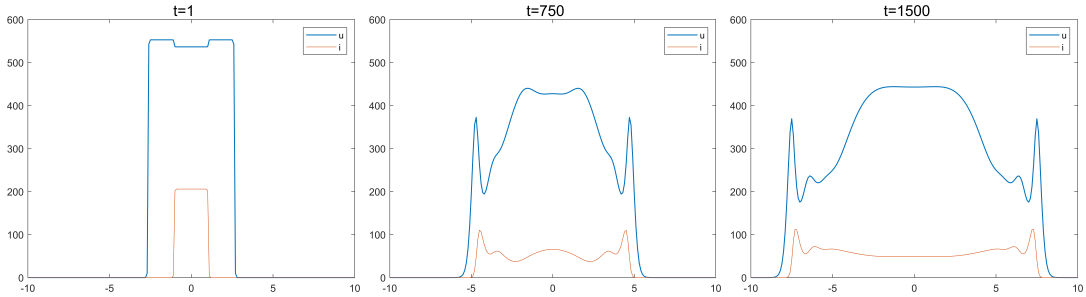

Figure 4.4: Temporal evolution of the PDE simulation. On the left, the initial state shows a homogeneous distribution of uninfected cells, with a central region of infected cells. In the intermediate phase (centre), the infection spreads laterally, increasing the number of infected cells. Finally, in the advanced phase (right), the infected population stabilises, reaching an almost uniform distribution.

In contrast, in the ABM model, the infection does not follow a regular pattern, but shows local variations due to the discrete nature of the model. As illustrated in Figure 4.5, the spread of infection occurs irregularly, with some areas becoming infected more rapidly and others more slowly. Note also that, although the values of u and i in the ABM initially match those in the PDE model, stochastic effects in the dicrete model lead to increasing divergence over time, thereby highlighting the differences between the two approaches.

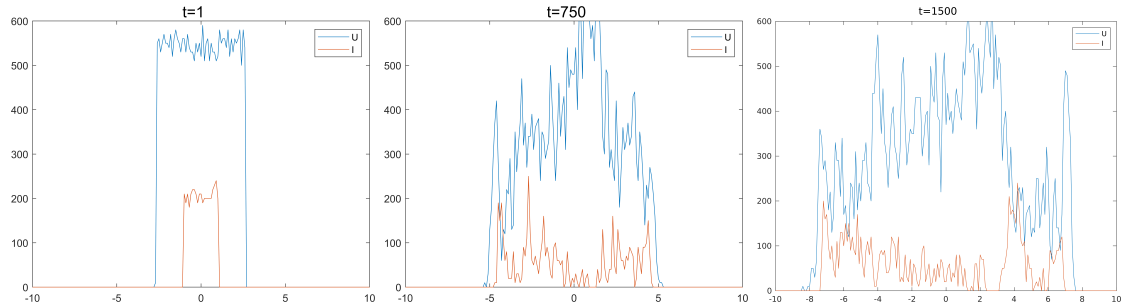

Figure 4.5: Temporal evolution of the ABM simulation. On the left, the initial state shows a configuration similar to the PDE model, with differences arising from the discrete nature of the model. In the intermediate phase (centre), peaks of infection emerge, with a non-uniform growth. In the advanced phase (right), the infection distribution appears less homogeneous than in the PDE model, highlighting the greater spatial variability of the agent-based model.

In conclusion, the PDE model provides a smoother and more uniform representation of infection spread, while the ABM highlights spatial variability resulting from discrete effects.

4.3 Temporal evolution of the tumour and the infection

After analysing the similarities and differences between the two models in the spread of infection, the evolution of the system is examined through the simultaneous comparison between the PDE and ABM models, considering both infected and uninfected cells as well as their epigenetic mean.

As introduced in the previous section, in the early stages the tumour appears in its initial configuration, with a clearly visible distribution of uninfected cells. The cells are organised into a compact and uniformly distributed mass. At this initial stage, uninfected tumour cells appear to proliferate without significant hinderance. The region in which the tumour is located appears compact and homogeneous, where treatment has not yet taken effect.

As time progresses, the treatment begins to take effect and the first signs of therapy are observed: infected cells begin to increase. It is noticeable that infection spreads more rapidly in areas with a lower density of uninfected cells, which is also consistent with the fact that the probability of contact (and therefore infection) is higher in these regions.

Figure 4.6 shows the temporal evolution of populations at three significant time points: the first row represents the cellular averages, while the second row shows the epigenetic mean.

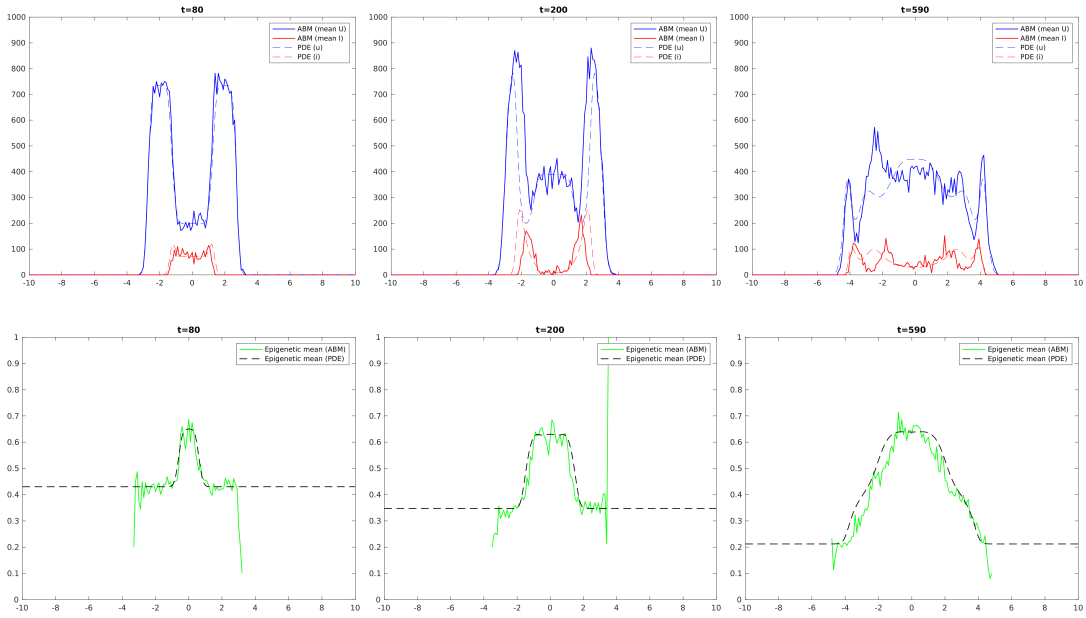

$t = 80$ $t = 200$ $t = 590$

Figure 4.6: Temporal evolution of the cellular average (first row) and the epigenetic mean (second row). In the first row, the graphs show the average cell population over five simulations: infected cells are represented in red, with a dashed line for the PDE model and a solid line for the ABM. In the second row, the epigenetic mean is shown with a solid green line for the ABM and a black dashed line for the PDE model. The temporal evolution highlights how the infection spreads rapidly, leading to a progressive reduction of uninfected cells. Over time, the epigenetic mean increases in central regions, suggesting a selective effect favouring cells with higher epigenetic states. Note also the presence of peaks in the ABM epigenetic mean, indicating fluctuations due to the stochastic nature of the model.

At time $t = 80h$, the spread of the infection has led to a significant increase in the number of infected cells, which begin to spread from the centre of the domain to the peripheral regions of the tumour. Uninfected cells are still largely present and appear more concentrated in the outer areas of the tumour, far from the regions where the therapy has taken effect. At the same time, the epigenetic mean remains relatively homogeneous, suggesting that epigenetic variability has not yet significantly influenced the selection of uninfected cells. There is a good agreement between the two models, especially in terms of the spatial distribution of cells.

Later, at $t = 200h$, the infection has advanced further outward. The number of infected cells has increased, with more pronounced peaks that are gradually shifting from the centre towards the periphery of the tumour. Uninfected cells are still present in large numbers, and their population continues to grow in the central region, although signs of infection are already visible. Differences between the ABM and PDE models begin to emerge more clearly, particularly in the shape and position of the peaks. At this stage, the epigenetic mean begins to show more noticeable variations: in the central region of the tumour, an increase in the epigenetic mean can be observed.

As time progresses, the number of infected cells continues to grow, while the number of uninfected cells decreases. This indicates a degree of effectiveness of the oncolytic virus, which successfully eliminates a large number of uninfected cells. The interaction between spatial diffusion and epigenetic variability appears to have reached a balance in which the remaining uninfected cells exhibit reduced proliferation, likely associated with higher values of y.

Over time, significant changes in the structure of the epigenetic mean become apparent, particularly in the central region of the spatial domain where cell densities are higher. This

phenomenon is clearly visible in Figure 4.6, where it can be seen that the epigenetic mean gradually increases in the central region, while remaining lower in peripheral zones.

In particular, the increase in epigenetic mean in the central regions indicates that cells with higher epigenetic states tend to persist longer in these areas. In contrast, in the peripheral regions, where the infection may be less intense or delayed, the epigenetic mean remains lower, suggesting that these cells retain epigenetic characteristics more similar to the initial state.

At time $t = 590h$, the system tends towards stabilisation: the population of uninfected cells is significantly reduced across the entire domain. Infected cells exhibit a more fragmented distribution, with several distinct peaks. The epigenetic mean shows a bell-shaped distribution, with a peak in the central tumour region. This trend suggests that, over time, the epigenetic structure of the cell population is reorganising, with a higher concentration of cells in elevated epigenetic states in the tumour core. The discrepancy between the ABM and PDE models becomes more evident at this stage, especially for uninfected cells, where the stochastic variability of the ABM is clearly visible.

Observing the entire simulation video, it becomes clear that, over the long term, the epigenetic mean reaches a sort of equilibrium, where variations become less pronounced and the spatial distribution stabilises. This appears to indicate that, following an initial phase of strong selection, the system tends to converge toward a more stable epigenetic configuration.

To understand the overall evolution of tumour dynamics within the PDE model, we study the integrated densities of uninfected and infected cells over time. These values are obtained by summing the cell distributions across the spatial domain at each time point, using the appropriate spatial discretisation weights. Specifically, we compute the following quantities:

- The total uninfected density $\rho_U(t)$ is computed as

$$\rho_U(t) = \sum_x \sum_y u(x, y, t)\, \Delta y\, \Delta x$$

- The total infected density $\rho_I(t)$ is computed as

$$\rho_I(t) = \sum_x i(x, t)\, \Delta x$$

The total cell burden at time t, denoted by $\rho_T(t)$, is simply the sum $\rho_T(t) = \rho_U(t) + \rho_I(t)$.

Figure 4.7 shows the temporal evolution of these densities: uninfected cells (in blue), infected cells (in red), and their total (in yellow). The resulting curves reflect the global tumour burden, combining the dynamics of both infection spread and tumour proliferation within the PDE model.

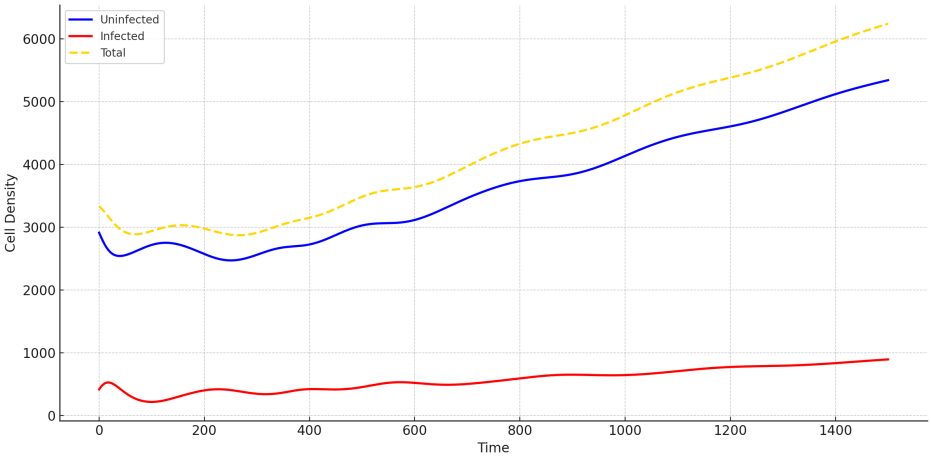

Figure 4.7: Temporal evolution of uninfected (blue), infected (red), and total (yellow) integrated cell densities, computed using spatial integration with $\Delta x = \Delta y = 0.1$. The vertical axis reports integrated cell density, and the horizontal axis corresponds to time in hours. The total cell burden grows steadily, with infected cells increasing rapidly early on and uninfected cells recovering later.

From the figure, several distinct phases in the dynamics can be identified. Initially, the infected cell density rises sharply, indicating rapid spatial propagation of the virus. During this early phase, the uninfected cell population declines, likely due to infection-induced loss. This divergence highlights the acute impact of viral spread on tumour integrity. As time progresses, the uninfected population begins to recover, possibly due to proliferation of resistant or spatially isolated subpopulations, while the infected population continues to grow more slowly. The total cell density increases steadily, reflecting net tumour growth driven by both infected and uninfected cell proliferation. This behaviour illustrates the complex interplay between spatial dynamics and selective pressures encoded in the PDE model.

It is important to note the fluctuations in the epigenetic average μ near the edges of the spatial domain, visible in the second row of Fig. 4.6, particularly at early time points. These variations are not due to numerical instabilities, but rather to the inherent stochasticity of the agent-based model. In those peripheral regions, the number of uninfected cells is extremely low, making random effects more pronounced and causing the dynamics to diverge from the expected mean behaviour. However, these few cells do not significantly influence the overall tumour dynamics. For this reason, we have chosen to retain these fluctuations in the plots: they highlight how the continuous approximation becomes less reliable when population sizes are too small. Notably, the strong agreement between models in terms of the average epigenetic trait breaks down near the tumour edges, where the number of cells is extremely low. In these regions, stochastic effects become more prominent, but their limited influence on the total cell population means they do not substantially alter the overall dynamics. This phenomenon will be examined more precisely in mathematical terms later on, when we present a direct comparison of the behaviour of μ in both models.
The joint analysis of the cellular mean and the epigenetic mean highlights how infection not only reduces the density of uninfected cells but also alters their epigenetic structure. Over time, epigenetic selection favours the survival of cells with specific epigenetic states, suggesting that the tumour response to virotherapy depends not only on cell density but also on its epigenetic organisation. This could be an important key to better therapies.

4.3.1 Comparison between cellular mean and epigenetic mean

Analysis of the epigenetic mean of uninfected cells introduces additional information beyond the simple average of total cell density. While the latter provides insight into the spatial

distribution of cells and their temporal evolution, the epigenetic mean offers an indication of the internal variability of uninfected cells, representing a synthesis of the evolution of their epigenetic state y over time. This parameter is particularly relevant because infected cells do not depend on the epigenetic variable, implying that their dynamics is less influenced by epigenetic variations and is more directly governed by interaction, infection, and diffusion processes.

Let us now analise a simulation that compares the average of the entire cell population (infected and uninfected) with the epigenetic mean (of uninfected cells only). Figure 4.8 shows a snapshot between the two parameters at $t = 1000h$, highlighting the main structural differences.

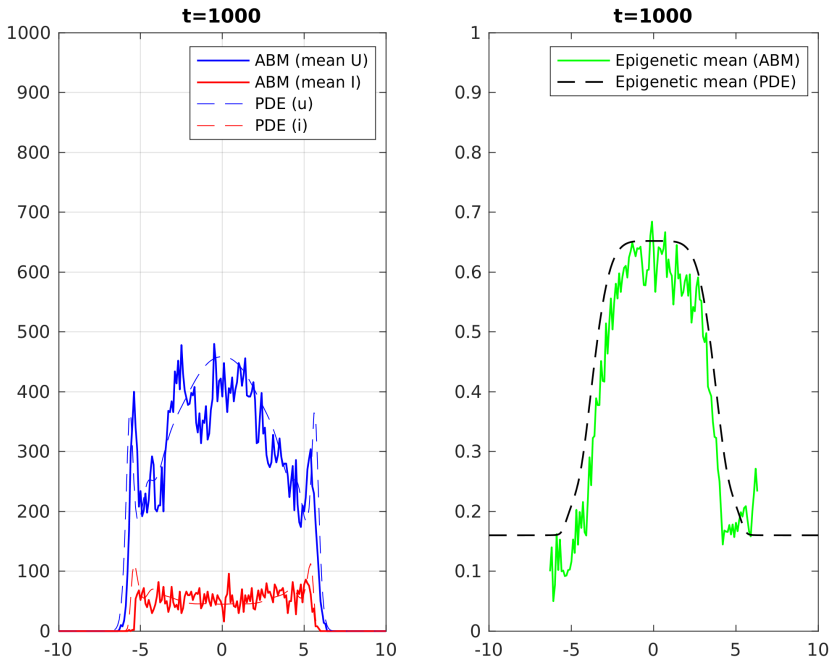

Figure 4.8: Comparison between the cellular mean (left) and the epigenetic mean (right) at time $t = 1000h$. In the left graph, the average of the cell populations is computed over five simulations: both models show a consistent infection spread pattern, with a progressive reduction of uninfected cells and a higher concentration of infected cells in the central region. In the right graph, the epigenetic mean is shown: a bell-shaped profile is observed, with higher values in the central area, suggesting that the epigenetic dynamics are consistent across the two models and confirm the selective effect of the infection.

Some key differences emerge from the two images:

1. The epigenetic mean reflects the distribution of the epigenetic state of uninfected cells, highlighting any phenotypic preferences (e.g., whether the population tends to maintain a more resistant or more vulnerable epigenetic state in response to infection). A significant variation in the epigenetic mean over time suggests that epigenetic mechanisms modulate the population's response.

2. The epigenetic mean is also useful for identifying differences between the PDE and ABM models: in the ABM, the presence of individual agents can generate local fluctuations that a simple average cannot capture, whereas the epigenetic mean makes it possible to highlight emerging trends in the epigenetic distribution.

To study the relationship between epigenetic state and the evolution of uninfected cells, we analyse the structured cell density $u(t, x, y)$ governed by the PDE system. Figure 4.9 shows the temporal evolution the total density of uninfected cells across the spatial domain, and the global epigenetic mean of the uninfected population. To facilitate the visual comparison

between biological quantities with different scales, we plot these two curves using dual vertical axes.

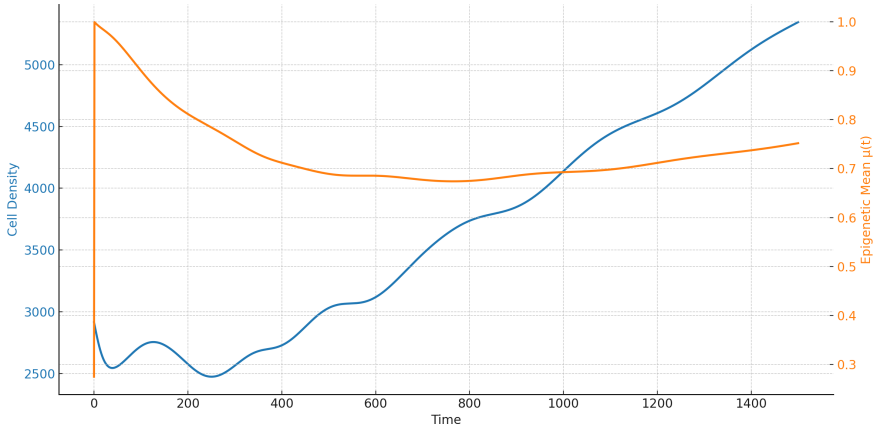

Figure 4.9: Temporal evolution of the total uninfected cell density (blue, left axis) and the global epigenetic mean (red, right axis), computed over 1500 hours. The vertical axes report the total number of uninfected cells (left axis) and the mean value of the epigenetic trait (right axis), respectively.

The total uninfected cell density (blue, left axis), denoted by $\rho_U(t)$, at time t is defined as:

$$\rho_U(t) = \int_\Omega \int_Y u(t, x, y)\, dy\, dx \tag{4.1}$$

To evaluate this quantity numerically, we discretise the domain uniformly with $\Delta x = \Delta y = 0.1$, and approximate the integral by summing $u(x, y, t)$ across all epigenetic states y at each spatial location x:

$$\rho_U(t) \approx \sum_x \sum_y u(t, x, y)\, \Delta y\, \Delta x \tag{4.2}$$

This quantity reflects the total number of uninfected cells across the spatial domain at each time point.

The epigenetic mean (red, right axis) captures the internal structure of the uninfected population. At each location x, the local epigenetic mean is defined as:

$$\mu(x, t) = \frac{\sum_y y\, u(x, y, t)}{\sum_y u(x, y, t)}$$

The global epigenetic mean is then obtained by spatially averaging $\mu(x, t)$:

$$\mu(t) = \int_\Omega \mu(x, t)\, dx \approx \sum_x \mu(x, t)\, \Delta x$$

This value represents the average epigenetic state across the uninfected population at time t.

Figure 4.9 allows us to jointly track the tumour size and the evolution of its internal structure. The density of uninfected cells reflects global tumour expansion, while the epigenetic mean gives insight into functional heterogeneity and the distribution of phenotypic states under selective pressure. This figure highlights the relative dynamics of the two measures, showing that while the cell density varies on a larger scale, the epigenetic mean also evolves over time, albeit within a narrower range. The plot reveals that while the uninfected cell density increases moderately over time, the epigenetic mean gradually decreases. This trend indicates a selective advantage for cells with lower epigenetic values (closer to $y = 0$), which, due to the

proliferation function $r(y) = 1 - \eta y^2$, divide more rapidly. Thus, even though the infection process is not directly governed by the epigenetic state, the internal composition of the healthy population evolves as a result of differential proliferation.

4.3.2 Comparison of epigenetic mean in PDE and ABM models

As shown in Figure 4.10, the epigenetic mean computed with the PDE model provides a clearer indication of structural variations throughout the domain, showing a more regular and continuous pattern. However, the ABM model, despite introducing local fluctuations due to its discrete nature, follows a dynamic consistent with the PDE model, suggesting that both approaches capture the same general trends of the epigenetic phenomenon.

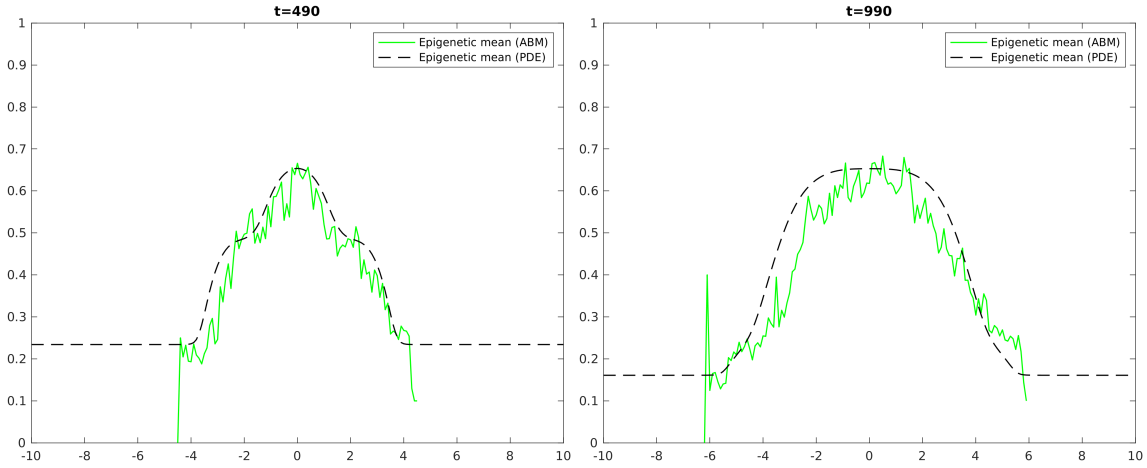

Figure 4.10: Comparison of the epigenetic mean between the agent-based model (solid green line) and the PDE model (dashed black line) at times $t = 490h$ (first panel) and $t = 990h$ (second panel). Both models show a bell-shaped profile with a central peak, indicating stronger epigenetic selection in the internal regions. The PDE model shows a smoother trend, while the agent-based model introduces local fluctuations. Despite these differences, both models show consistent evolution, with a progressive increase in the epigenetic mean in the central region.

At time $t = 490h$, both models exhibit a **bell-shaped epigenetic distribution**, with higher values in the central region. The PDE model provides a smoother and more continuous curve, while the ABM introduces minor local fluctuations. These differences are expected due to the discrete nature of the agent-based model, but they do not affect the overall consistency between the two approaches: both indicate an increase in the epigenetic mean in the central areas, a sign of more intense selection in these regions. However, in peripheral areas, the ABM shows a more irregular decline in the epigenetic mean compared to the PDE, suggesting greater local variability due to stochastic interactions between cells.

At $t = 990h$, the evolution continues to follow a similar trend in both models, with a further increase in the epigenetic mean in the central zones. The PDE model maintains a regular trend, while the ABM displays more pronounced oscillations, especially in the central part of the spatial domain. This suggests that, in the agent-based model, epigenetic selection does not occur perfectly uniformly but is influenced by local factors. Despite these variations, the overall profile of the epigenetic mean remains consistent between the two models, confirming that the emerging behaviour is robust and well described by both approaches.

A notable aspect concerns the **peripheral zones**: in the PDE model, the epigenetic mean remains relatively constant at the edges of the domain, whereas in the ABM it shows a more irregular decrease. This implies that, in the agent-based model, some cells may have retained

a lower epigenetic state, reflecting a more heterogeneous selection process compared to the continuous description provided by the PDE model. This highlights a difference in local details, but at the same time reinforces the consistency between the models, as both confirm the general trend of epigenetic increase in the central part of the domain.

Finally, the progressive *divergence* between the two models over time suggests that, in the long term, epigenetic selection may lead to greater heterogeneity in the discrete model, while in the PDE model this variability is smoothed out by the continuous nature of the equations.

Observation on the presence of NaN values in the ABM

An interesting aspect observed in the ABM is the presence of NaN values in the epigenetic mean in certain regions, which does not occur in the PDE model: as seen in Figure 4.10, there are abrupt interruptions in the continuous (green) line of the ABM model, especially in the peripheral regions.
This phenomenon can be explained mathematically by considering the definition of the epigenetic mean:

$$\mu(x,t) = \frac{\int_Y yu(x,y,t)dy}{\int_Y u(x,y,t)dy} \tag{4.3}$$

where the denominator represents the density of uninfected cells in the epigenetic space.

In the ABM, which is discrete, it is possible that in some regions of the domain there are no uninfected cells present, causing the denominator to become zero. When this happens, the formula for the epigenetic mean becomes undefined, resulting in NaN values.

In the PDE model, instead, cell density is treated as a continuous function, making it less likely for the denominator to vanish. Even if the density becomes very small, this situation is numerically handled without resulting in a division by zero.

The comparison between the two models shows that, despite differences in local details and in the representation of spatial variability, both coherently describe the phenomenon of epigenetic selection. However, the discrete model introduces numerical challenges in scenarios where the cell population is very low, generating NaN values in the epigenetic mean. This aspect represents a structural difference between the two approaches and must be taken into account when interpreting the results.

4.3.3 Variance of the epigenetic mean

The variance of the epigenetic mean is a statistical measure that describes the spread of epigenetic values around their mean. In other words, it indicates how much the epigenetic states of uninfected cells deviate from the average in a given spatial region and over time.
To characterise the internal heterogeneity of the uninfected tumour population, we compute the variance of the epigenetic distribution over time. This measure quantifies the extent to which individual cells deviate from the mean epigenetic state at each time point.

Mathematically, the local variance of the epigenetic mean is defined as follows:

$$\sigma^2(x,t) = \frac{\int_Y (y-\mu(x,t))^2 u(x,y,t)dy}{\int_Y u(x,y,t)dy}$$

where:

- y is the epigenetic state of the cell
- $\mu(x,t)$ is the previously computed epigenetic mean

- $u(x, y, t)$ is the density of uninfected cells with epigenetic state y

To obtain a biologically meaningful global variance $\sigma^2(t)$, we integrate $\sigma^2(x, t)$ across the spatial domain:

$$\sigma^2(t) = \int_\Omega \sigma^2(x, t)\, dx \approx \sum_x \sigma^2(x, t)\, \Delta x$$

This accounts for both the magnitude and spatial distribution of phenotypic heterogeneity. This quantity provides a global measure of the phenotypic heterogeneity within the uninfected tumour population. A high epigenetic variance $\sigma^2(t)$ indicates substantial diversity in the epigenetic states of the tumour cells, while a low value suggests a more homogeneous population.

In the context of oncolytic virotherapy, such heterogeneity can influence treatment outcomes. A diverse tumour may contain subpopulations with distinct phenotypic traits, potentially including cells that are less susceptible to infection. In contrast, a more uniform epigenetic profile implies that most cells respond similarly to viral propagation and are subject to similar selective pressures.

The curve shown in Figure 4.11 displays the evolution of the spatially integrated epigenetic variance over time, computed from the PDE simulations of uninfected cell dynamics. This integration takes into account both the distribution of epigenetic states and their spatial density across the domain. The analysis reveals three main temporal phases:

- **Initial phase** ($t \lesssim 200$ h): the variance is relatively high but begins to decline. This suggests that the initial tumour is phenotypically diverse, but early selective pressures due to infection and competition begin to reduce variability.
- **Transition phase** ($200 \lesssim t \lesssim 800$ h): the variance steadily decreases, reaching a minimum. This period likely corresponds to strong epigenetic selection, where only certain phenotypes persist in the face of infection and local crowding effects.
- **Late phase** ($t \gtrsim 800$ h): the variance slowly increases again. This may indicate either the re-emergence of diversity due to epigenetic drift or mutation, or the repopulation of the domain with cells that explore a broader range of epigenetic traits.

Overall, this behaviour highlights the dynamic balance between epigenetic selection and diversification. The trajectory of $\sigma^2(t)$ offers insight into how treatment and intrinsic dynamics shape tumour heterogeneity over time.

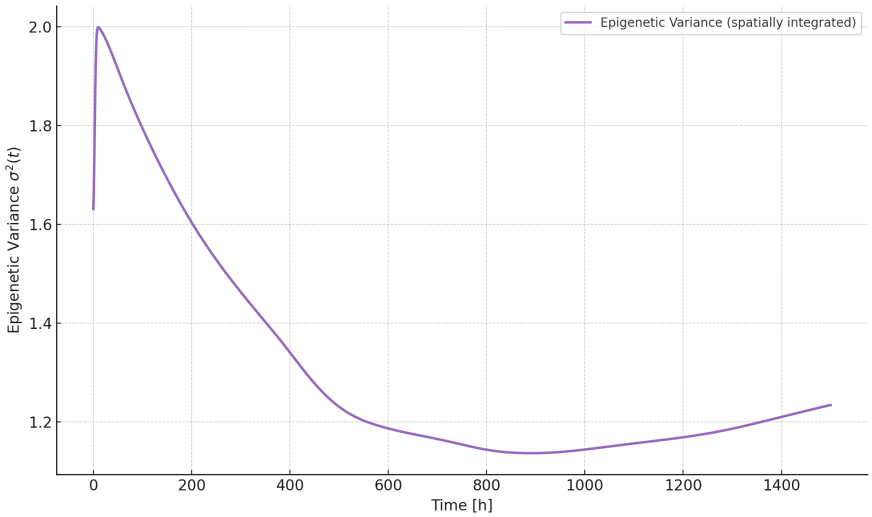

Figure 4.11: Temporal evolution of the epigenetic variance $\sigma^2(t)$, integrated over space using the spatial step $\Delta x = 0.1$, computed from the PDE model for the uninfected tumour cell population over 1500 hours. As a result, the horizontal axis shows time, while the vertical axis represents a single aggregated variance value per time step. This quantity reflects the degree of internal phenotypic heterogeneity across space and time. The initial decline indicates a reduction in epigenetic diversity due to selective pressures, while the late-phase increase may signal re-diversification or the emergence of new subpopulations. Although the data originates from PDE, the consistency between the continuous model and the corresponding agent-based model ensures the general validity of the observed behaviour.

The observed trend of variance suggests that viral infection does not act uniformly in the tumour population but induces dynamic epigenetic selection, leading to increased cellular heterogeneity during certain phases. This result is particularly interesting because it shows that virotherapy not only reduces the tumour population but also actively modifies the epigenetic composition of the remaining cells.

If the variance of the epigenetic mean remains high over time, it indicates the presence of subpopulations resistant to infection, which may have significant clinical implications: in a real-world context, these cells could be responsible for tumour relapse after treatment.

However, if the variance progressively decreases, it means that the virus has successfully selected a more homogeneous and potentially more vulnerable population, increasing the chances of tumour eradication. This could be very important for clinical application.

4.3.4 Conclusions

The analysis conducted so far allows us to better understand the dynamics of infection spread and the evolution of cell populations over time. To look at the problem from a different angle, we introduce an additional analysis based on heatmaps. Heatmaps are graphical representations where individual values contained in a matrix are represented using a colour scale. The colour intensity at each point reflects the magnitude of a variable at a given time.

Heatmaps show the temporal evolution of cell populations and their epigenetic mean. Through these visualisations, it is possible to observe the progression of infection, the reduction of uninfected cells, and the emergence of epigenetic dynamics over time.

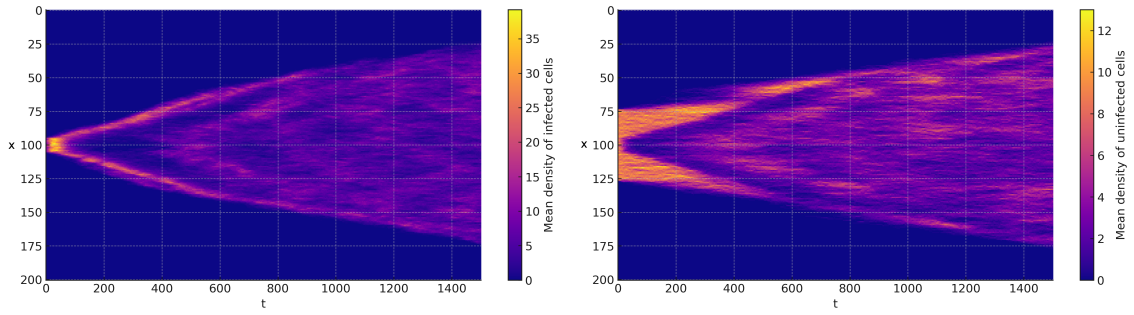

Figure 4.12: Temporal evolution of infected and uninfected cells. The horizontal axis represents time t, while the vertical axis indicates spatial position x. The color bar on the right shows the cell density scale, with higher values indicated by lighter colors (yellow) and lower values by darker colors (blue). The image on the left shows the spread of infection over time, while the image on the right highlights the decrease of uninfected cells under the same conditions.

Figures 4.12 shows the spatiotemporal distribution of the infected and uninfected cell populations, respectively. Both maps are plotted as functions of the spatial coordinate x and time t, with colour intensity indicating the local cell density. Warmer colours correspond to higher densities.
The uninfected population $u(x, y, t)$ depends not only on space and time but also on the epigenetic state y. To obtain a comparable representation to the infected population $i(x, t)$, we computed the marginal density $u(x, t) = \int_Y u(x, y, t)\, dy$ by summing over all discrete epigenetic states. This provides a global view of the tumour mass evolution, accounting for all uninfected cells regardless of their epigenetic configuration.

At the beginning ($t = 0\,h$), the density of infected cells is concentrated around a central spatial state. This phase shows a density peak (yellow area), suggesting that the infection initially affects cells with intermediate epigenetic traits. In contrast, uninfected cells are more widely distributed across the spatial domain, with higher densities (lighter colours) indicating a strong presence at various states.

As time progresses, the infection spreads along the y axis, creating a fan-like shape. A bifurcation in propagation is observed: two main regions of high density emerge and move away from the initial point. The infection spreads in both directions along the y axis, indicating spatial dispersion within the system. Uninfected cells also form two main regions over time, moving away from the central position and creating a fan-like structure as well. However, the areas between these two "arms" show a lower density, suggesting that these zones are quite sensitive to changes from uninfected to infected cells.

Over times $t > 100\,h$, the infected region appears more diffused and less concentrated compared to the initial phase, indicating a more uniform distribution of infected cell density; simultaneously, the number of uninfected cells in these areas decreases over time.

Another key aspect of cell dynamics is the temporal evolution of the epigenetic mean. Analysing this quantity allows us to understand the role of epigenetic variability in the interactions between infected and uninfected cell populations. To investigate the evolution of epigenetic heterogeneity within the tumour cell population, we computed and analysed $\mu(x, t)$, defined as the average epigenetic state of uninfected cells at each spatial location x and time t. This quantity allows us to assess how the local distribution of epigenetic traits changes during the dynamics and in response to the viral infection.

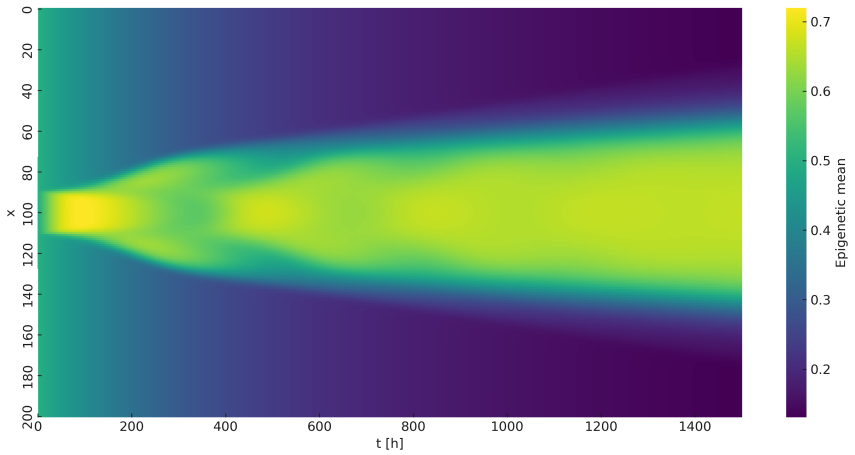

Figure 4.13: Heatmap of the epigenetic average $\mu(x,t)$. Each point in the map represents the mean epigenetic state of uninfected tumour cells at spatial position x and time t. High values (yellow regions) indicate zones where tumour cells exhibit high epigenetic activity, which is often associated with increased proliferation or resistance to infection. Conversely, low values (dark regions) indicate low epigenetic activity, possibly corresponding to more quiescent or susceptible cells. The map provides a dynamic picture of the tumour's epigenetic landscape and reveals how heterogeneity evolves under the combined effects of proliferation, diffusion, and viral interaction.

Figure 4.13 shows the spatiotemporal distribution of the epigenetic mean $\mu(x,t)$ within the uninfected tumour cell population. The horizontal axis represents time (in hours), and the vertical axis corresponds to the spatial variable x. The colour scale encodes the value of the epigenetic average: lighter (warmer) colours correspond to higher values of μ, while darker (colder) colours indicate lower averages.

Initially, a localised region of high epigenetic activity appears near the centre of the domain, suggesting the presence of a subpopulation of cells with enhanced proliferative properties. As time progresses, this region expands spatially, indicating the spread of these cells. Meanwhile, peripheral areas remain characterised by lower epigenetic values, which may correspond to more quiescent or susceptible cells. Over longer timescales, the pattern stabilises, forming a broader central band of intermediate-to-high epigenetic activity.

The heatmap reveals the temporal and spatial progression of the tumour's epigenetic profile. If high epigenetic states become dominant in certain regions, it may suggest that those areas harbor more aggressive or resistant cell populations. Alternatively, localised reductions in $\mu(x,t)$ could indicate successful viral suppression or a shift toward less proliferative phenotypes. Monitoring $\mu(x,t)$ therefore provides insights into the evolving resistance and adaptability of the tumor.

Note. Unlike other works, where such quantities are evaluated only at a fixed point (e.g., $x = 0$), here we compute and visualize the full spatial-temporal structure of $\mu(x,t)$. This allows for a more complete understanding of spatial heterogeneity and the effects of diffusion and local interactions on epigenetic evolution.

Note 2. The heatmaps are computed using the solution of the ABM model, by averaging over spatial and temporal bins, which captures the discrete spatio-temporal dynamics of the tumour and infection. However, the same type of visualisation could be generated from the continuous model (PDE), making the two approaches comparable in terms of output interpretation.

4.4 Comparison between models and initial conditions

The aim of this section is to characterise the dynamics of infected and uninfected cells under three different configurations, each given by distinct initial conditions for the distribution of infected cells. The analysis focuses on how these initial conditions influence the behaviour of infected cells and their impact on the uninfected population.

Specifically, we consider three settings:

- **Simulation** `1`: characterised by a small initial number of infected cells, with an initial radius $R_i = 0.5$ mm and an initial concentration $h_{\text{inf}} = 0.1K$.
- **Simulation** `standard`: intermediate condition with initial radius $R_i = 1$ mm and initial concentration $h_{\text{inf}} = 0.2K$. This is the baseline simulation used throughout this study.
- **Simulation** `2`: characterised by a higher initial number of infected cells, with an initial radius $R_i = 1.6$ mm and an initial concentration $h_{\text{inf}} = 0.3K$.

Uninfected cells, on the other hand, maintain the same initial conditions in all simulations: $R_u = 2.6$ mm, $h_{\text{uninf}} = 0.5K$.

4.4.1 Results

Agent-Based Model (ABM): comparison between `agenti1`, `agenti_standard`, and `agenti2`

The analysis reveals significant differences between the three configurations, which emerge in Figure 4.14.

- **Simulation** `agenti1`: With a smaller initial radius and lower initial concentration of infected cells, propagation occurs gradually and locally. The expansion speed of the infected front is low, which means that uninfected cells remain dominant for a significant portion of the simulation.

  As seen in Figure 4.14a, at $t = 100h$ the infected cells show two distinct peaks with an irregular shape. In Figure 4.14b, after 1000 hours, the infection has spread but is still growing more slowly compared to other two setups considered here.

- **Simulation** `agenti_standard`: The spread is faster than in `agenti1`.

  In Figure 4.14c, after 100 hours, the infection has already expanded and is less localised. By $t = 1000h$ (Figure 4.14d), the spread is more uniform and covers a larger region compared to `agenti1`, showing a more balanced growth.

- **Simulation** `agenti2`: Increasing both the initial radius and the concentration leads to faster and more extensive infection propagation.

  As shown in Figure 4.14e, by $t = 100h$, the fluctuations are pronounced, and the infection is more widespread than in `agenti1`. At $t = 1000h$ (Figure 4.14f), the infected region has expanded considerably, with a scattered and irregular distribution.

As anticipated, the analysis shows that the speed and uniformity of propagation strongly depend on the initial conditions. Simulation `agenti1` exhibits slow and localised expansion, while `agenti2` results in faster, irregular diffusion. The `agenti_standard` configuration lies between, with a more balanced propagation compared to the extremes.

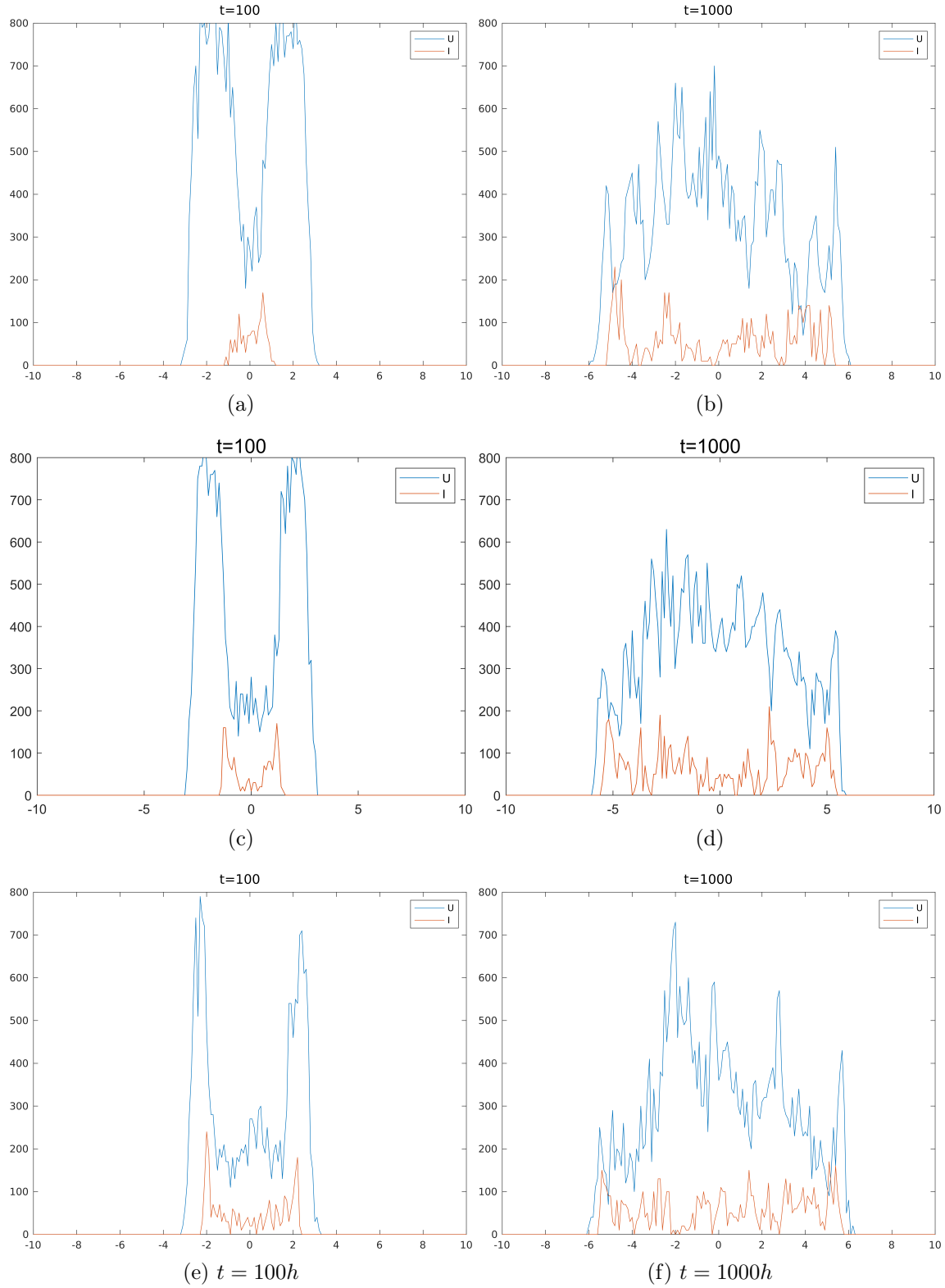

Figure 4.14: Comparison of infection propagation in the ABM model. The first row represents the configuration with fewer infected cells (`agenti1`), the second row corresponds to the standard configuration (`agenti_standard`), and the third row represents the configuration with more infected cells (`agenti2`). The columns indicate the two time points analysed: 100 hours (left) and 1000 hours (right).

PDE Model: comparison between `pde1`, `pde_standard`, and `pde2`

As for the ABM case, we analyse the three different cellular dynamics using the continuous model. From Figure 4.15, we observe that:

- **Simulation** `pde1`: With a low initial concentration of infected cells, the infection remains confined during the early stages of the simulation.

  At $t = 100h$ (Figure 4.15a), two distinct peaks are visible with limited infection. At $t = 1000h$ (4.15e), the spread has occurred, but the infected front remains relatively contained compared to the other cases.

- **Simulation** `pde_standard`: This case represents an intermediate spread.

  From Figures 4.15c and 4.15d, we observe that in $t = 100h$ the infection has spread more widely than in `pde1`, with a smoother gradient and a less fragmented front. At $t = 1000h$, the infected region has expanded considerably, covering a larger area than in `pde1`, while maintaining a relatively homogeneous structure, unlike `pde2`.

- **Simulation** `pde2`: The spread is faster and more extensive compared to the other cases.

  At $t = 100h$ (4.15e), the infection is already widespread with larger but lower peaks. After 1000 hours (Figure 4.15f), the infected domain is almost completely saturated, with a more uniform distribution than `pde1`, but less structured than `pde_standard`.

These results show that diffusion dynamics are strongly influenced by the initial conditions. The `pde1` configuration exhibits slower and more localised growth, while `pde2` shows rapid and widespread diffusion. The `pde_standard` simulation falls between these extremes, with a more balanced and progressive expansion compared to the others.

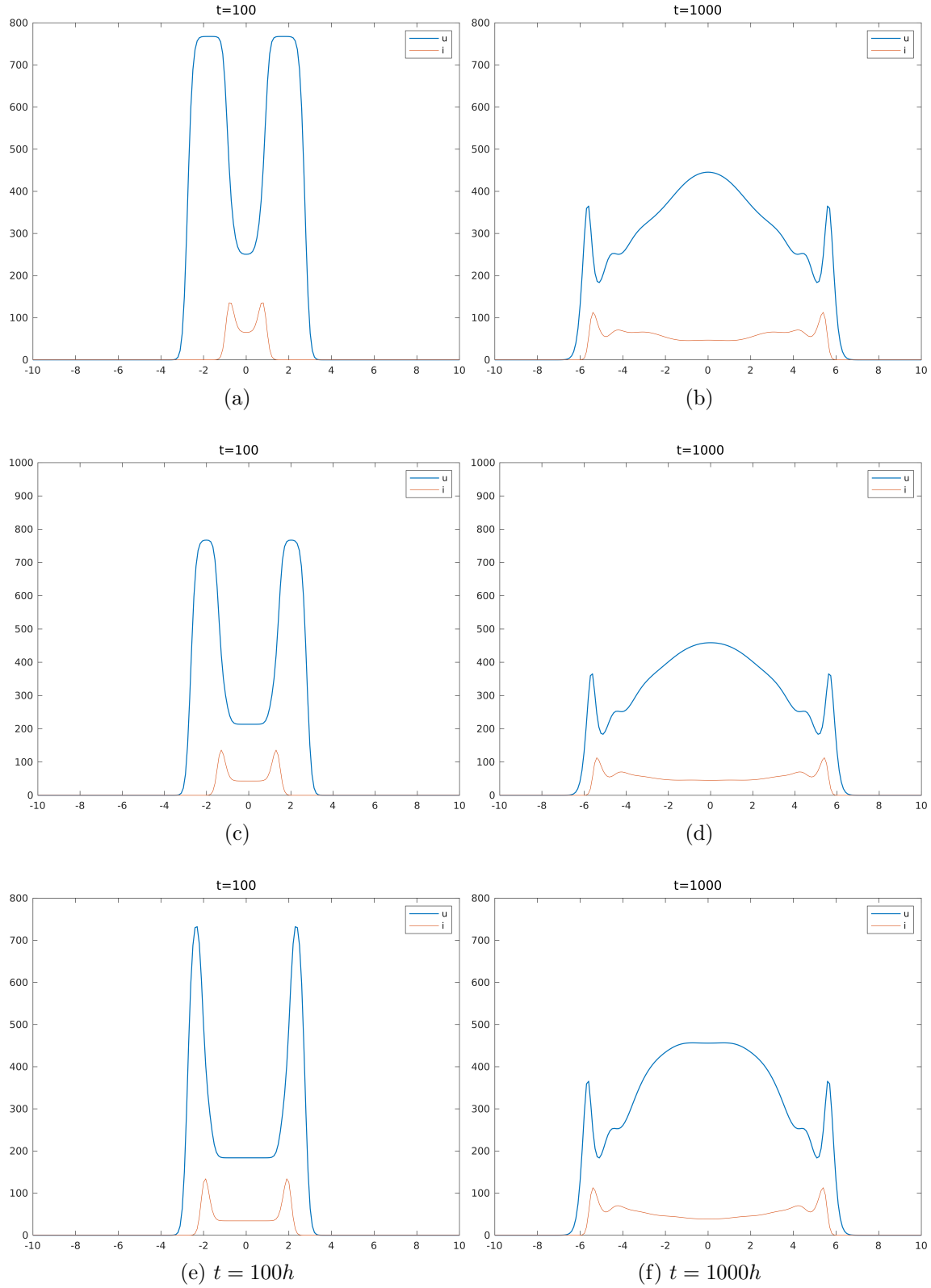

Figure 4.15: Comparison of infection propagation in the PDE model. The first row represents the configuration with fewer infected cells (`pde1`), the second row corresponds to the standard configuration (`pde_standard`), and the third row represents the configuration with more infected cells (`pde2`). The columns indicate the two time points analysed: 100 hours (left) and 1000 hours (right).

4.4.2 Conclusions

The comparison between the three simulations shows that the initial concentration and radius of the infected cells significantly influence diffusion dynamics. In particular, a higher number of initially infected cells accelerates the spread of the infection, while a lower number slows it down and keeps it more localised.

The analysis shows that increasing the radius and initial concentration of infected cells in configuration `agenti2` and `pde2` leads to faster diffusion and a more disorganised spread of infection; the intermediate configuration `agenti_standard` and `pde_standard` lies between the two extremes, showing a more balanced expansion and a more uniform infection gradient over time; finally, the configuration with fewer infected cells, `agenti1` and `pde1`, exhibits a segmented growth, with an infection that remains localised for a longer period and spreads more slowly.

In models based on partial differential equations (PDEs), the speed of diffusion is closely related to the initial conditions, with a significant impact on the progression of infection over time. In particular, `pde2` shows how a wider and more uniform gradient favours a faster spread of the infection, progressively reducing the areas without infected cells.

The comparison between the simulations also reveals differences in the spatial distribution of the infection: the infection follows a more "chaotic" dynamics when the initial concentration is high in the ABM, while in PDE models the propagation is more continuous and homogeneous. The simulation `pde1` displays distinct peaks suggesting segmented infection growth, while `pde2` shows a uniform and less structured spread, indicating efficient propagation.

These results confirm the importance of initial conditions in diffusion models and suggest that, depending on the parameters chosen, very different propagation scenarios can emerge. A high value of the initial concentration not only leads to faster diffusion, but also influences how the infection extends in space and time.

To confirm that the behaviours observed in the individual ABM and PDE models are also consistent in the averaged simulations, let us collate the data in Figure 4.16, which show that the average of the simulations reflects the trends already observed.

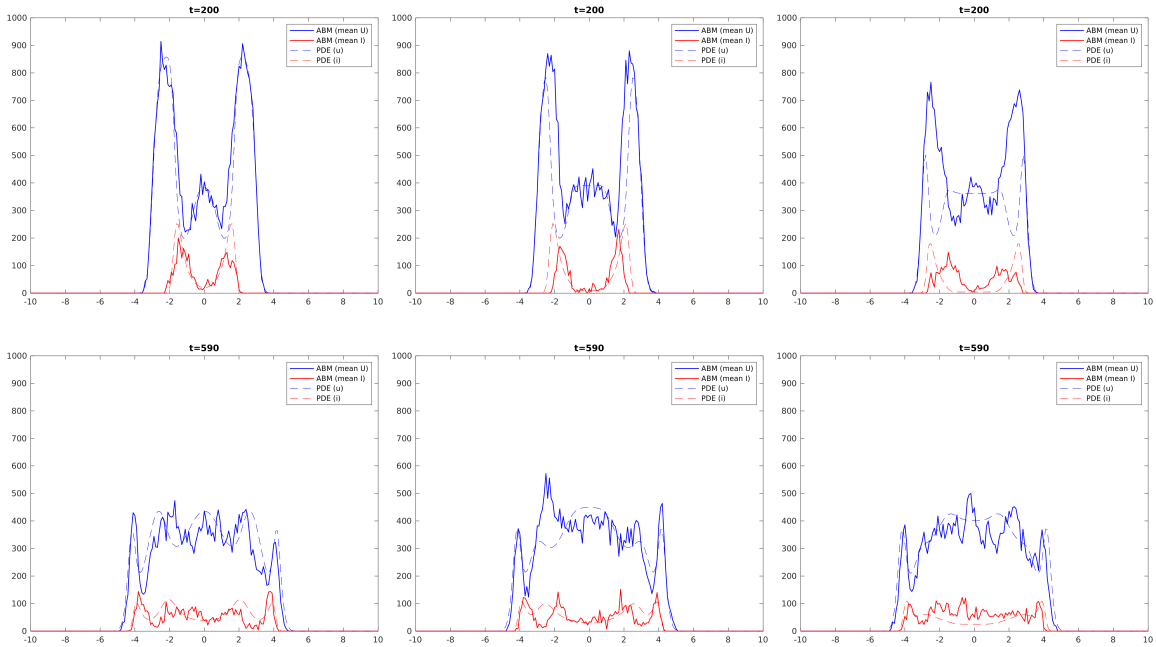

(a) Fewer infected (b) Standard condition (c) More infected

Figure 4.16: Comparison of infection propagation under different initial conditions. The first row shows the distributions at time $t = 200h$, while the second row shows the distributions at time $t = 590h$. A higher number of initially infected cells leads to a wider and less structured spread of the infection over time: note that in the last two panels (more infected), the initial discrepancy between ABM and PDE at $t = 200h$ decreases notably by $t = 590h$.

The first three images in Figure 4.16 show the distribution of infected and uninfected cells at $t = 200h$ for the three scenarios considered. Results are familiar.

In the first case, the infection spreads more slowly and remains localised, with two distinct peaks indicating a segmented growth. The presence of uninfected cells is still dominant compared to the other cases.

In the standard case, the spread is more homogeneous than in the low-infection scenario, and the infected front appears less segmented. The propagation reflects what is observed in the individual simulations, with a balanced expansion.

Finally, in the last case, the infection spreads more rapidly, with lower but wider peaks. The distribution is less structured than the other two cases, indicating less localised propagation.

At $t = 590h$, as shown in the second row of images in Figure 4.16, the differences between the three scenarios become even more pronounced.

In the case with fewer infected cells, the propagation remains more contained, with two distinct peaks still indicating a segmented diffusion.

In the standard case, the infection spreads more uniformly, confirming the balance between localisation and propagation observed in the individual models.

When the number of infected cells is increased, the infected front is much more extended and less structured, suggesting a faster and less organised diffusion compared to the other two cases. It is worth noting one final point in this scenario, concerning the comparison between the ABM and PDE models. At time $t = 200h$, the difference between the two approaches is quite pronounced, particularly in the distribution of uninfected cells, where the ABM exhibits sharper and more irregular peaks compared to the smoother profile of the PDE. However, as the simulation progresses, this discrepancy becomes significantly less evident. By $t = 590h$, the profiles generated by the ABM and PDE models show a much closer alignment, both in

the spatial extent and in the shape of the infected and uninfected distributions. This suggests that the divergence observed in the early stages is largely transient and tends to diminish as the system evolves, highlighting a convergence of the two modelling approaches over time.

The analysis of the averages generalises the trends obtained in the individual simulations: the initial concentration of infected cells plays a fundamental role in the speed and pattern of infection spread.

4.5 The importance of epigenetics and viral infectivity

In this section, our objective is to analyse the influence of two key parameters in the model: η and ζ. The parameter η controls the epigenetic inhibition of the growth of uninfected cells, while ζ influences the infection rate of the oncolytic virus. Both factors play a crucial role in determining the dynamics of tumour evolution and the response to viral therapy.

As said, the function $r(y)$, which represents the growth rate of uninfected cells, is defined as:

$$r(y) = 1 - \eta y^2$$

while the function $\beta(y)$, which regulates the probability of infection of uninfected cells, is given by:

$$\beta(y) = \beta_1 + \zeta(1 - y^2)$$

Simulations are performed with different values of η and ζ to analyse their effect on cellular behaviour. From the simulation videos, significant frames are extracted at three specific time points to observe the spatial distribution of the cells and the influence of variations in these two parameters.

4.5.1 Analysis of the effect of η

Simulations are carried out using five distinct values of η: 0.001, 0.4, 0.5, 0.6, 0.99, to capture its effect on cell behaviour and to identify differences with respect to the standard value ($\eta = 0.5$).
In all simulations, the value of ζ is kept fixed at its commonly used value, $\zeta = 0.0002$.

Images show the evolution of the distribution of uninfected cells over time, at three distinct time points ($t = 360h$, $t = 740h$, $t = 1120h$). The solid blue line represents the ABM, while the dashed line represents the solution of the PDE model.
From the extracted frames, significant differences in the behaviour of uninfected cells emerge as a function of the value of η.

Let us begin with $\eta = 0.001$. Epigenetic inhibition is negligible, and cells retain a high proliferative rate. This leads to a rapid expansion of the tumour front, with a more uniform distribution of cells across space. Under this condition, tumour growth appears almost uncontrolled, with a homogeneous spread of uninfected cells.

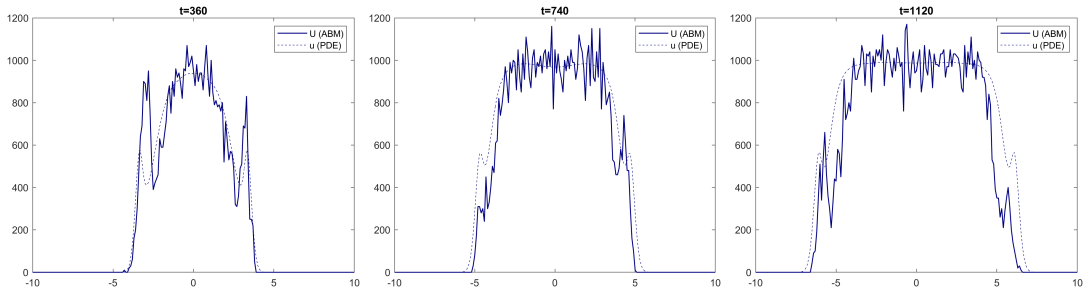

Figure 4.17: Evolution of the cell distribution for $\eta = 0.001$ at times $t = 360h$, $t = 740h$, and $t = 1120h$. A rapid and uniform growth is observed, with high cell density and a more homogeneous spatial distribution compared to higher values of η. The agent-based model shows greater fluctuations compared to the PDE solution.

A detailed analysis of the individual time points reveals that:

- $t = 360h$ **(Figure 4.17, left)**: At this stage, the tumour front has already expanded significantly, with high local variability in cell distribution. The discrepancy between the agent-based model and the PDE solution is particularly evident in the central regions, where more pronounced fluctuations are observed.
- $t = 740h$ **(Figure 4.17, centre)**: Proliferation continues and the tumour front advances further. The cell distribution becomes more uniform compared to the previous stage, with reduced local oscillations, while the PDE model provides a smoother profile compared to the stochastic behaviour of the agents.
- $t = 1120h$ **(Figure 4.17, right)**: At this point, the cell distribution stabilises, with a central region showing a consistently high density. The tumour front has significantly expanded its spatial domain, and the comparison between the agent-based model and the PDE solution shows good overall agreement.

Next, with $\eta = 0.4$, the growth of uninfected cells is less inhibited than in the subsequent cases we'll see, as the function $r(y)$ remains high for values of y close to 1. This results in a higher cell density in regions with high epigenetic values, suggesting more proliferative behaviour. Overall, a more irregular spatial distribution is present, compared to the previous case.

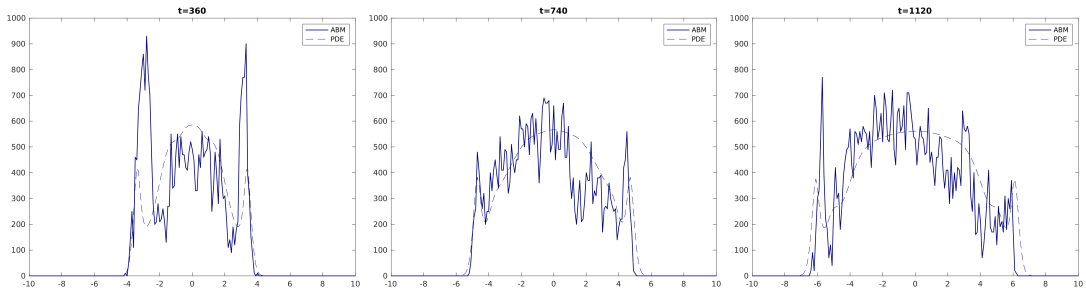

Figure 4.18: Evolution of the cell distribution for $\eta = 0.4$ at times $t = 360h$, $t = 740h$, and $t = 1120h$. A slower growth is observed compared to $\eta = 0.001$, with a more irregular spatial distribution.

Different time points reveal that:

- $t = 360h$ **(Figure 4.18, left)**: At this stage, distinct growth peaks are observed, with a more irregular distribution compared to $\eta = 0.001$. The agent-based model shows greater variability compared to the PDE solution.
- $t = 740h$ **(Figure 4.18, centre)**: Proliferation continues, but with greater spatial variability. A reduction in maximum cell density is observed compared to the previous case, with a more fragmented growth pattern.

- $t = 1120h$ **(Figure 4.18, right)**: Growth stabilises, but the cell distribution is less homogeneous than in cases with lower values of η. Spatial heterogeneity is pronounced, with significant fluctuations in the agent-based model.

Progressing further, an intermediate value of η allows a balance between proliferation and inhibition. In this configuration ($\eta = 0.5$), a more homogeneous behaviour is observed in cell densities, with a gradual advancement of the epigenetic front. The spatial distribution of cells appears to be more regular than in the cases with lower η.

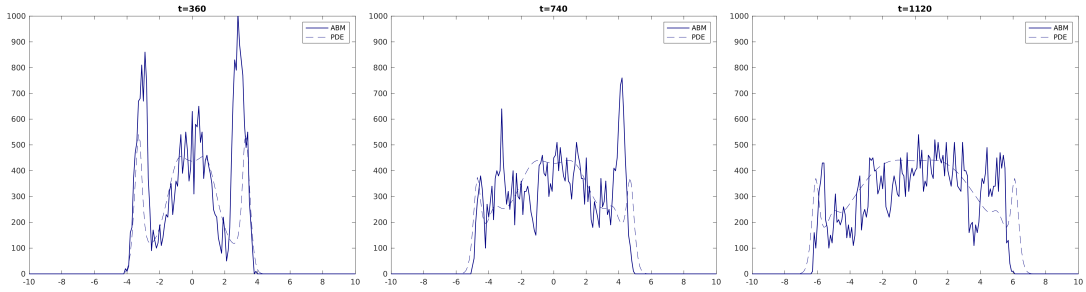

Figure 4.19: Evolution of the cell distribution for $\eta = 0.5$ at times $t = 360h$, $t = 740h$, and $t = 1120h$. A more regular and balanced growth is observed compared to previous cases.

In this case, we have:

- $t = 360h$ **(Figure 4.19, left)**: Different peaks are still present, but the spatial distribution is more uniform than in the lower η cases. The tumour front develops in a more structured and less "chaotic" way.
- $t = 740h$ **(Figure 4.19, centre)**: Proliferation continues with fewer fluctuations compared to previous cases, suggesting a controlled and less disordered growth.
- $t = 1120h$ **(Figure 4.19, right)**: The system reaches a stabilised cell distribution, with the tumour front expanding more regularly and predictably over time.

At a higher $\eta = 0.6$ there is intense epigenetic inhibition, limiting cell growth for high values of y. This leads to a higher concentration of cells in low epigenetic states ($y \approx 0$), with a slower invasion front compared to previous cases.

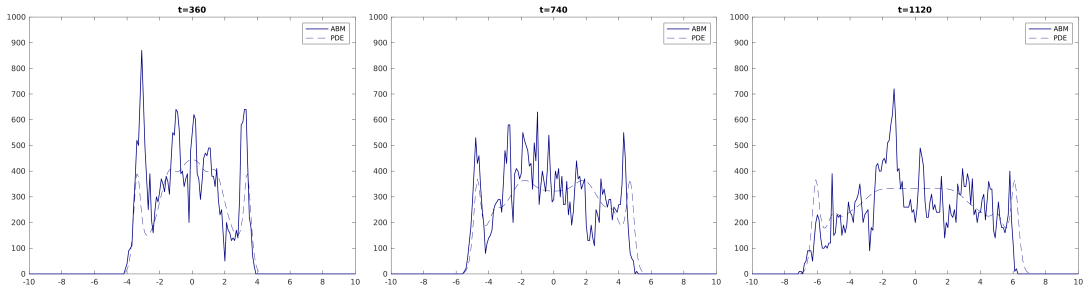

Figure 4.20: Evolution of the cell distribution for $\eta = 0.6$ at times $t = 360h$, $t = 740h$, and $t = 1120h$. Slower growth is observed compared to previous cases, with a less uniform spatial distribution. The agent-based model shows larger oscillations than the PDE model, as expected. However, the discrepancy is more evident than in previous cases with lower η. The PDE solution appears more regular, with a smoother distribution and no sharp peaks.

In fact, we see the following:

- $t = 360h$ **(Figure 4.20, left)**: The growth peaks are more attenuated than in previous cases, with a less uniform distribution of cells.

- $t = 740h$ **(Figure 4.20, centre)**: Proliferation slows down, with a more fragmented and less dense cell distribution compared to lower values of η.
- $t = 1120h$ **(Figure 4.20, right)**: The system stabilises with a limited tumour front, indicating a more evident effect of epigenetic inhibition on cell growth.

An interesting aspect that emerges is the presence of a very pronounced peak in the ABM around $x \approx -2$, a behaviour not observed in the PDE model (see Fig. 4.20, right). This discrepancy suggests that, in this configuration, the discrete model generates a marked local aggregation of tumour cells in a specific region of epigenetic space, showing a high concentration of cells in a narrow range, likely due to the intrinsic stochastic fluctuations of the discrete model.
This result indicates that increasing epigenetic inhibition not only slows down cell growth but also alters the spatial distribution of uninfected cells, making it less uniform.

The final, limiting case is given by $\eta = 0.99$. A markedly different behaviour is observed compared to the previous cases. Strong epigenetic inhibition drastically reduces the proliferative capacity of uninfected cells, resulting in a more irregular distribution and a significant slowdown of the invasion front. Cells tend to remain more concentrated in specific areas, suggesting that the parameter η not only regulates the growth rate, but also influences typical spatial patterns.

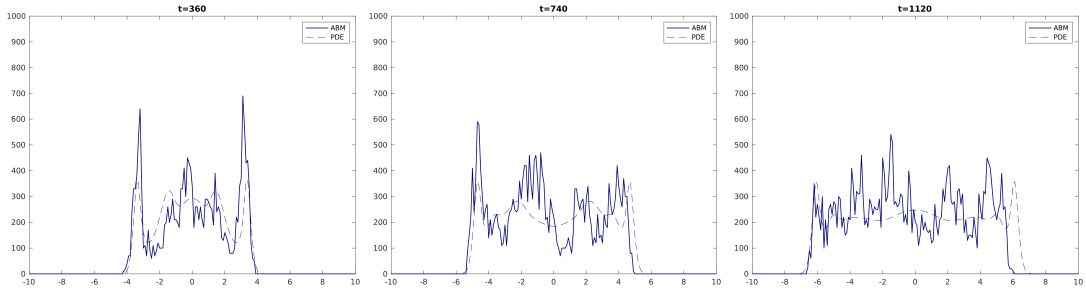

Figure 4.21: Evolution of the cell distribution for $\eta = 0.99$ at times $t = 360h$, $t = 740h$, and $t = 1120h$. tumour growth appears strongly limited, with a sparse cell distribution and minimal expansion.

Different time points now show that:

- $t = 360h$ **(Figure 4.21, left)**: Very weak growth peaks are observed, with a reduced and more localised cell distribution.
- $t = 740h$ **(Figure 4.21, centre)**: The proliferation rate is almost stagnant, with very limited growth and significantly reduced tumour expansion compared to previous cases.
- $t = 1120h$ **(Figure 4.21, right)**: The system stabilises with a highly sparse cell distribution and nearly halts tumour growth, confirming the strong impact of epigenetic inhibition.

The analysis of the simulations for different values of the parameter η revealed significant differences in the proliferation of uninfected cells. The main effects on tumour growth are summarised as follows:

- With low values of η ($\eta = 0.001$), epigenetic inhibition is negligible, and cells proliferate without significant restrictions. This leads to highly aggressive tumour growth compared to the standard case. Proliferation is virtually unchecked, and the spatial distribution is much more uniform, with no limits to expansion.

- For intermediate values such as $\eta = 0.4$, growth is slightly faster than in the standard case, while epigenetic regulation still effectively limits uncontrolled expansion.
- With higher values of η ($\eta = 0.6$), growth is significantly reduced compared to the standard case $\eta = 0.5$, with a more irregular distribution and lower cell density.
- In extreme cases ($\eta = 0.99$), the tumour almost completely stops expanding. Epigenetic inhibition dominates, cell proliferation is very low, and the tumour front stabilises quickly without further spatial spread.

Epigenetic inhibition, governed by η, plays a crucial role in determining the aggressiveness of tumour growth and the effectiveness of cell proliferation. High values of η could correspond to therapeutic strategies aimed at limiting tumour growth through epigenetic regulation. However, low values of η reflect conditions in which cell growth is not regulated, leading to uncontrolled tumour expansion.

4.5.2 Analysis of the effect of ζ

To evaluate the impact of parameter ζ, several simulations are performed by varying its value with respect to the standard value $\zeta = 0.0002$, considering three cases: $\zeta = 0$ (no variation of the infectivity with y), $\zeta = 0.0001$ (half the standard value), and $\zeta = 0.0004$ (double the standard value).
In all simulations, the value of η is fixed at $\eta = 0.5$, that we use as a starting value in reference simulations.

From the simulation videos, representative frames are extracted at three specific time points ($t = 360h$, $t = 740h$, $t = 1120h$) to observe the spatial distribution of uninfected cells and the effect of varying ζ on infection dynamics. By analyzing these frames, significant differences emerge in the behaviour of uninfected cells depending on the value of ζ.

Let us start with a $\zeta = 0$. In this scenario, the probability of infection is independent of the epigenetic state y, meaning that all cells have the same susceptibility to the virus. This condition results in a uniform propagation of the infection throughout the cell population, without preferential selection based on the epigenetic variable. As a consequence, the infection spreads homogeneously across all values of y, without forming preferential clusters.

As shown in Figure 4.22, an interesting behaviour emerges: in the absence of epigenetic dependence, the virus does not significantly alter the overall dynamics of tumour growth because of poor infection rates. Furthermore, the PDE solution closely follows the profile of the ABM, with slight fluctuations due to the discrete nature of the latter.

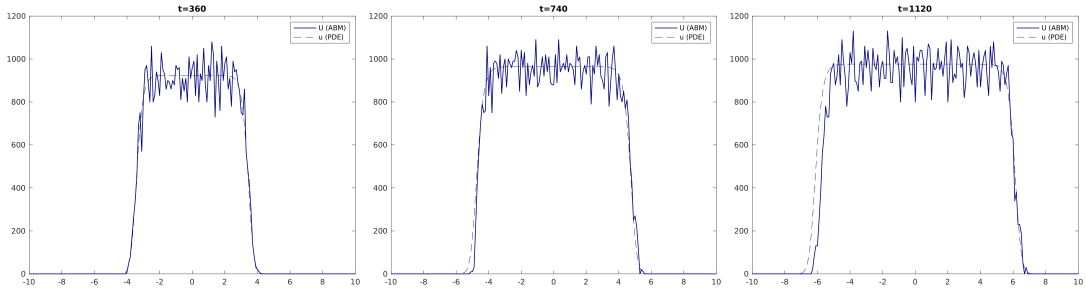

Figure 4.22: Evolution of the cell distribution for $\zeta = 0$ at times $t = 360h$, $t = 740h$, and $t = 1120h$. tumour growth is uniform and unaffected by changes in infectivity. The agent-based model shows slight fluctuations compared to the PDE solution.

Looking at the selected time points reveals the following:

- $t = 360h$ **(Figure 4.22, left)**: tumour growth is uniform and resembles the standard case of proliferation without infection. The tumour front is well defined, with an almost flat distribution in the central region.
- $t = 740h$ **(Figure 4.22, centre)**: The distribution of tumour cells continues to expand without signs of containment or reduction. A slight delay is observed in the PDE solution compared to the ABM, suggesting a stronger diffusion effect in the former.
- $t = 1120h$ **(Figure 4.22, right)**: Growth reaches a peak with a maximum cell density evenly distributed throughout the domain. The tumour front is well consolidated, and the differences between the agent-based model and the PDE solution are minimal, indicating convergence towards an almost steady-state distribution.

Let us continue with $\zeta = 0.0001$. In this case, the epigenetic dependence of infection is present but weaker than in the standard value. Infection develops less uniformly than in the case $\zeta = 0$, with a slight tendency to target cells with lower y values. Therefore, tumour propagation is slower and infection is selective: cells with low values of y are more likely to be infected.

Looking at the images in Figure 4.23, the effect of infection begins to influence tumour growth, with a less homogeneous distribution than in the case $\zeta = 0$. In particular, the central regions of the distribution show more pronounced variations over time, indicating a progressive reduction in cell density due to infection.

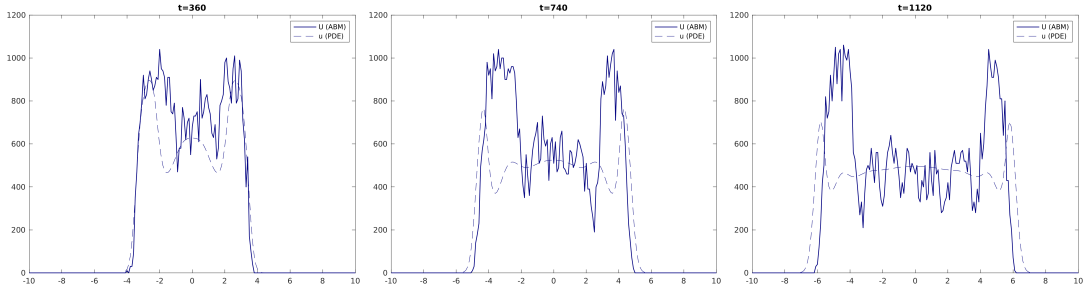

Figure 4.23: Evolution of the cell distribution for $\zeta = 0.0001$ at times $t = 360h$, $t = 740h$, and $t = 1120h$. Partial containment of tumour growth is observed, with more noticeable changes in cell distribution compared to $\zeta = 0$.

Analysis now reveals the following:

- $t = 360h$ **(Figure 4.23, left)**: Differences begin to emerge in the central regions of the cell distribution compared to the infection-free case. Slight fluctuations in tumour density are observed, indicating the initial action of the infection.
- $t = 740h$ **(Figure 4.23, centre)**: Cell proliferation slows down, and more pronounced fluctuations appear with a more fragmented distribution. Infection appears to begin limiting tumour growth in some regions. Note the increasing discrepancy between PDE and ABM.
- $t = 1120h$ **(Figure 4.23, right)**: Tumour expansion is less uniform and cell density is reduced compared to the standard case. The growing effect of infection is evident, significantly impacting the spatial distribution of tumour cells and increasing the fluctuations in the ABM.

Let us now look at $\zeta = 0.0002$. This represents the reference case, where the virus shows a clear preference for cells with low y. Infection progresses selectively, primarily targeting less proliferative cells. As a result, the infection front expands at a moderate rate, causing a more visible reduction in tumour growth compared to lower values of ζ.

Looking at Figure 4.24, the effect of infection is more pronounced than in previous cases. The distribution of tumour cells appears less uniform, with reduced density in the central regions. This indicates that infection effectively limits tumour growth.

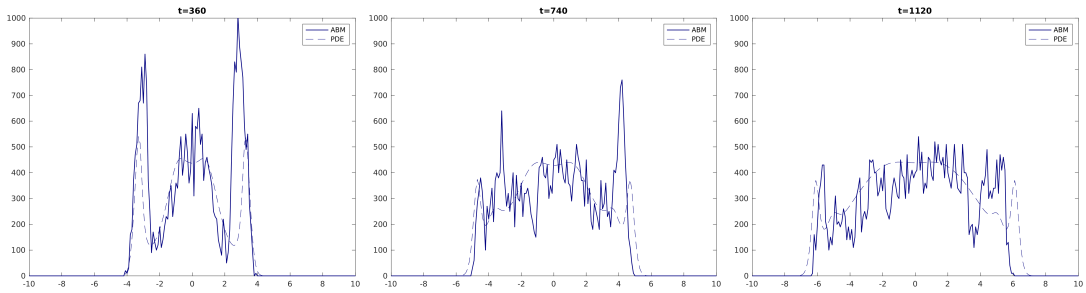

Figure 4.24: Evolution of the cell distribution for $\zeta = 0.0002$ at times $t = 360h$, $t = 740h$, and $t = 1120h$. Tumour growth is more contained compared to the cases with lower infectivity. Note the lower values for u respect to the previous plots.

Detailed analysis of each time point shows:

- $t = 360h$ **(Figure 4.24, left)**: Tumour growth is already more limited than in cases with lower infectivity. Clear changes in cell distribution are visible, indicating the effect of infection. The maximal values of u are less than in the previous case.
- $t = 740h$ **(Figure 4.24, centre)**: Proliferation also slows down, with a more heterogeneous profile. Regions with reduced cell density appear in the central area, indicating effective infection.
- $t = 1120h$ **(Figure 4.24, right)**: The tumour shows significant stabilisation, with significantly lower cell density compared to cases with lower ζ. Growth is clearly limited by infection, resulting in a more fragmented spatial distribution.

In the final case, for $\zeta = 0.0004$, the epigenetic selectivity of the infection is at its maximum: the virus almost exclusively targets cells with low y values (those with the highest proliferative potential). This affects tumour growth dynamics, strongly limiting the spread of uninfected cells and creating a spatial distribution very different from cases with lower ζ.

As shown in Figure 4.25, tumour growth is severely altered, with a visible reduction in cell density and a spiky, fragmented behaviour. Comparison with the PDE solution shows that infection results in greater heterogeneity and a slower expansion of the tumour front.

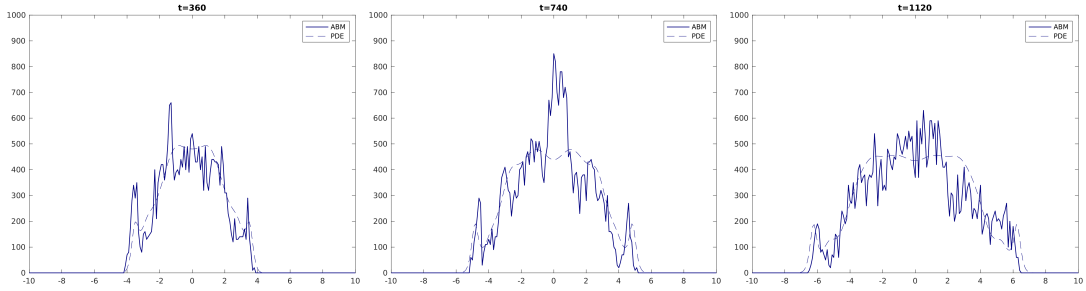

Figure 4.25: Evolution of the cell distribution for $\zeta = 0.0004$ at times $t = 360h$, $t = 740h$, and $t = 1120h$. Strong tumour growth containment and greater fragmentation in the cell distribution are observed compared to previous cases, with dense fluctuations throughout.

Looking at the chosen time points, we see:

- $t = 360h$ **(Figure 4.25, left)**: The effect of infection immediately manifests with lower cell density compared to lower-infectivity cases. A clear reduction in tumour population

is seen in the central region. Note also the reduction in the peaks at the edges of the profile.

- $t = 740h$ **(Figure 4.25, centre)**: Cell proliferation is significantly reduced, with a less compact and more fragmented tumour distribution. The PDE solution shows a more diffuse structure than the ABM, suggesting a stronger infection effect.

- $t = 1120h$ **(Figure 4.25, right)**: The tumour is strongly contained, with very limited growth and a more disorganised structure than in other cases. Infection has generated a strong epigenetic selection effect that drastically reduces the presence of proliferative tumour cells.

An important aspect that emerges is the presence of a pronounced peak in tumour cell distribution in the ABM around $x \approx 0$ (see Fig. 4.25, centre). This behaviour is not as evident in the continuous PDE model, which instead exhibits a homogeneous and diffuse distribution. The origin of this discrepancy can be attributed to the combined effect of the high epigenetic selectivity of viral infection and the stochastic fluctuations inherent in the ABM.
In particular, the high value of ζ implies that infection preferentially targets cells with low y values, i.e., those with higher proliferation rates. This effect, together with the discrete dynamics of the agents, can lead to localised concentrations of residual tumour cells that temporarily evade infection.
Another point to consider is the difference in fluctuations between the two models: in this specific configuration, the discrete model appears to show a more segmented behaviour and less consistency with the continuous solution compared to previous cases. This suggests that increasing ζ not only limits tumour growth, but also introduces more pronounced spatial effects, leading to a more heterogeneous cell distribution. This is an important point that can have consequences for clinical therapies, especially for tumours with high heterogeneity.

To sum up, the analysis of simulations for different values of the parameter ζ highlights significant differences in cell proliferation and the effectiveness of viral therapy, particularly compared to the standard case.

- With $\zeta = 0$, infection has no effect, and tumour growth is indistinguishable from an untreated tumour. Cell density remains high, and tumour expansion is uncontrolled.

- With $\zeta = 0.0001$ (half the standard value), infection begins to affect tumuor growth, but containment is still limited. The proliferation slows slightly compared to the infection-free case.

- With the standard value $\zeta = 0.0002$, tumour proliferation is clearly reduced compared to previous cases. Infection contains growth and cell distribution becomes less uniform.

- With $\zeta = 0.0004$ (twice the standard value), infection is extremely effective. Cell density in the central regions is significantly reduced, and tumour expansion is almost completely stopped. Nonetheless, some localised growth can still be seen.

In conclusion, the standard value of ζ represents a balance between cell proliferation and infection containment: any significant deviation from this value leads to marked effects on tumour growth.

Finally, the analysis of parameters η and ζ highlights two distinct but complementary effects. The parameter η controls the proliferation of uninfected cells, which influences the overall growth of the cellular population, whilst ζ governs the epigenetic selectivity of viral infection. These two parameters must be considered together in therapeutic strategies: balancing tumour proliferation and viral spread could optimise the effectiveness of virotherapy while minimising the risk of tumour resistance.

In the next section, we analyse the influence of the two parameters just discussed on the dynamics of infected and uninfected cells, as well as on the behaviour of the epigenetic mean $\mu(x,t)$.
As it will be shown, both models considered yield qualitatively similar results, showing good agreement on the behaviour of cell growth as a function of η and ζ. The plots presented illustrate the trends in both models and the main differences pertain to the smoother and continuous nature of the PDE model compared to the higher stochastic variability of the agent-based model. The overall trends remain instead consistent.

4.5.3 Analysis of the influence of η on cellular behaviour

In this section, we analyse the combined behaviour of infected and uninfected cells for three different values of η: two extremes ($\eta = 0.001$ and $\eta = 0.99$) and the standard case ($\eta = 0.5$). For each case, we examine the distribution of both cellular populations over time and their epigenetic mean. The results are illustrated in the following.

Let us consider the dynamics of uninfected and infected cells for the three values of η.

For $\eta = 0.001$, the growth of uninfected cells is almost independent of y: cells are distributed almost homogeneously in the epigenetic space, with significant presence even for high values of y. The infection develops in a gradual and diffuse manner, without particularly intense peaks.

Looking at Figure 4.26 (left panel), we can see that the tumour front is rapidly expanding, with a very rapid growth of the uninfected population and a limited presence of infected cells. The central panel shows that proliferation has advanced further: the density of uninfected cells has reached very high values and the spatial growth appears uniform. Finally, in the rightmost image, growth stabilises, with the cellular distribution maximised.

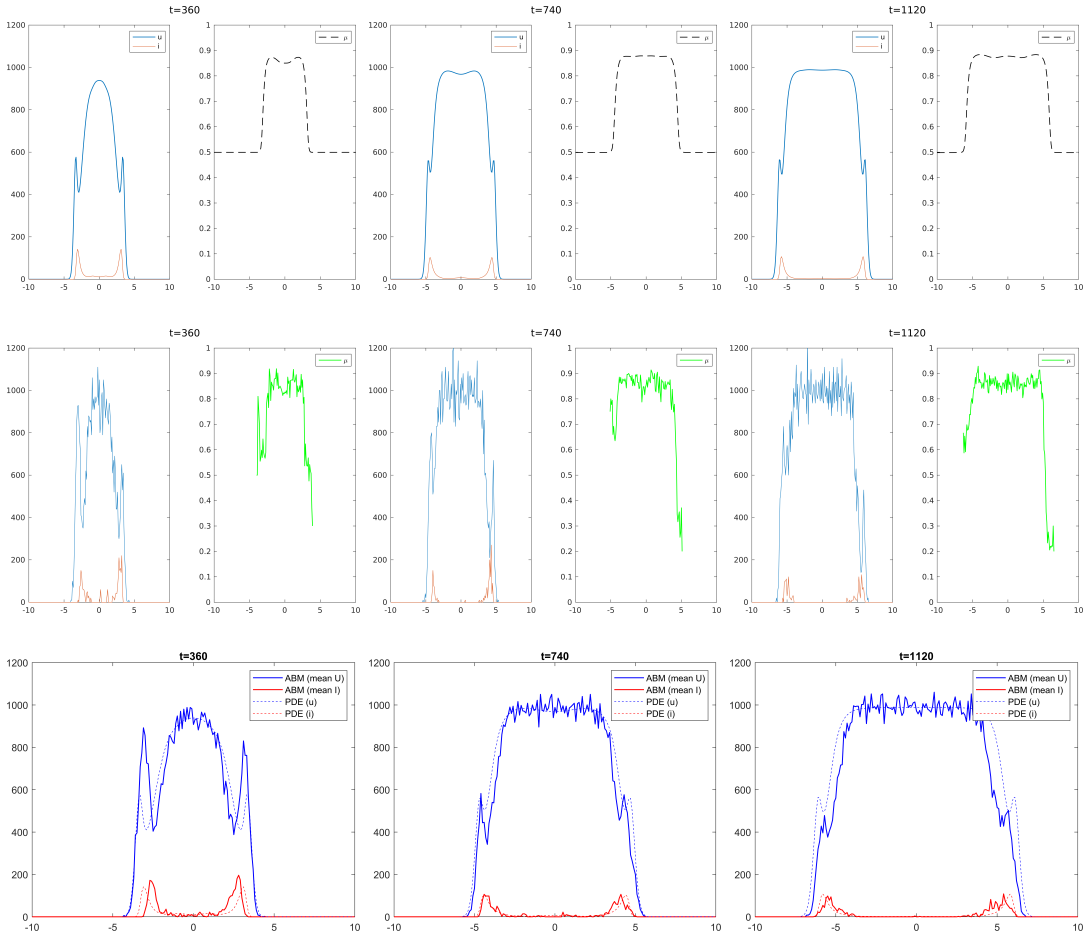

Figure 4.26: Evolution of cellular populations for $\eta = 0.001$. The top three panels show the results of the PDE model at times $t = 360h$, $t = 740h$, and $t = 1120h$, with blue and red curves representing uninfected and infected cells, respectively. A rapid and diffuse growth of uninfected cells is observed, with a scarce presence of infected ones. The epigenetic mean μ, represented in the right panels, is high in the central region, indicating a low level of epigenetic regulation. The central three panels show the same time points for the ABM model, confirming the behaviour observed in the PDE with slight stochastic fluctuations. The bottom three panels display the average cellular density profiles, computed over 5 independent ABM simulations at the same time points. These averaged curves provide a smoother, population-level view of the ABM behaviour, facilitating comparison with the deterministic PDE model.

With $\eta = 0.5$, we already know that epigenetic regulation has a more pronounced effect on cell proliferation, maintaining a balance between growth and inhibition. Growth is more balanced: a certain spatial order and intermediate cell concentration can be observed. The growth front appears more homogeneous, and the expansion is less aggressive compared to the previous case.

From the first image in Figure 4.27, it can be seen that cell growth has already started, but progresses more slowly than in the previous case. As time progresses (central image), the distribution of uninfected cells becomes more homogeneous, and growth is more controlled. Finally, cellular growth stabilises in a more balanced way.

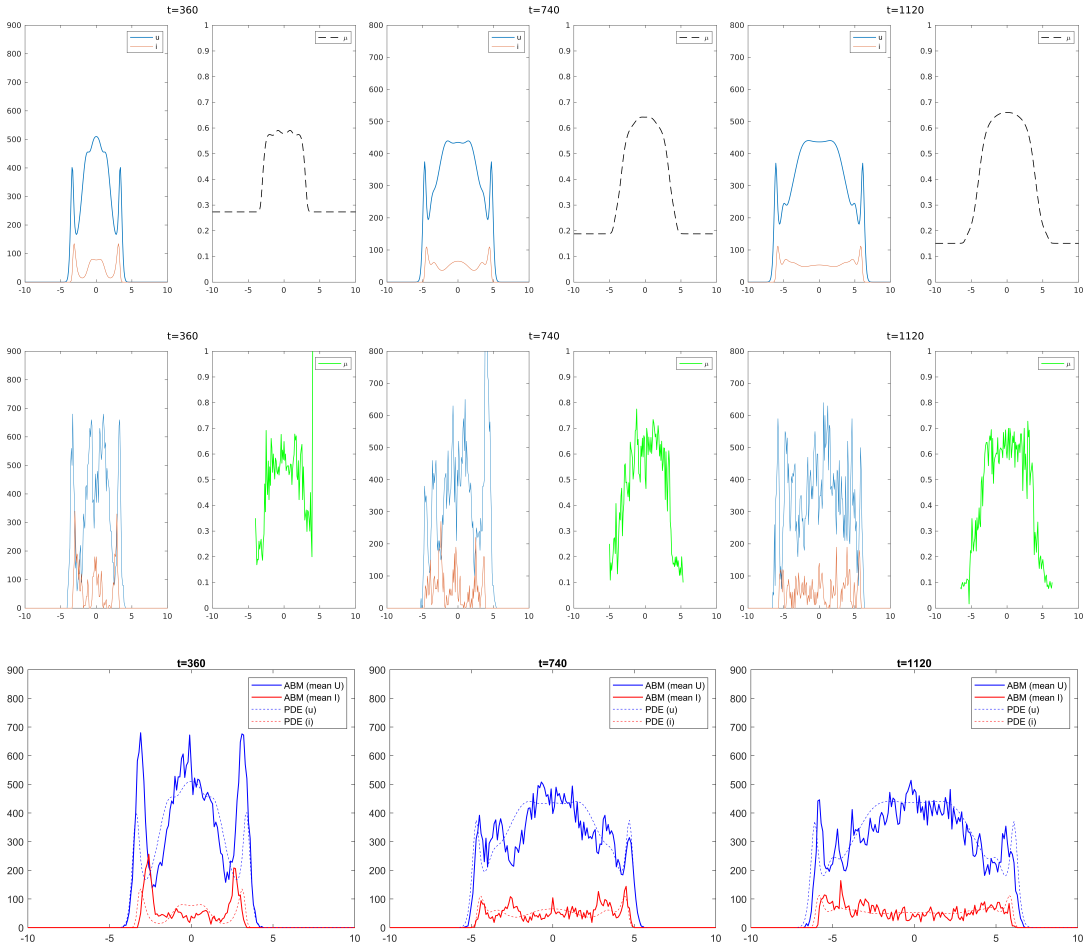

Figure 4.27: Evolution of cellular populations for $\eta = 0.5$. The top three panels correspond to the PDE model and show a mildly balanced growth of uninfected cells, with more controlled expansion compared to the $\eta = 0.001$ case. The epigenetic mean takes on moderate values, suggesting a clearer regulatory effect. The central panels display the ABM model results at the same time points, confirming the trend seen in the PDE and showing similar distributions for both cell populations. The distribution of the epigenetic mean is also consistent between the two models, indicating that epigenetic inhibition is beginning to have a significant impact on the system's behaviour. The bottom panels present the average cellular densities, obtained by averaging over 5 independent ABM simulations. These plots provide a smoothed view of the ABM behaviour, useful for quantitative comparison with the deterministic PDE solution.

For a large $\eta = 0.99$, epigenetic inhibition is very strong, significantly limiting the growth of uninfected cells. This leads to a drastic reduction in the tumour population: the growth of cells with high y is strongly suppressed, with cells clustering in restricted regions, showing very limited spatial expansion. The population of uninfected cells is almost exclusively made up of cells with low y values. The infection becomes highly localised and disordered, with irregular spatial distribution.

Figure 4.28 shows that growth is significantly constrained, with a much lower cell density compared to previous cases. As time progresses, proliferation remains limited, with fewer uninfected cells present. In the final panel, tumour growth appears almost completely stopped, with a very sparse distribution of both uninfected and infected cells.

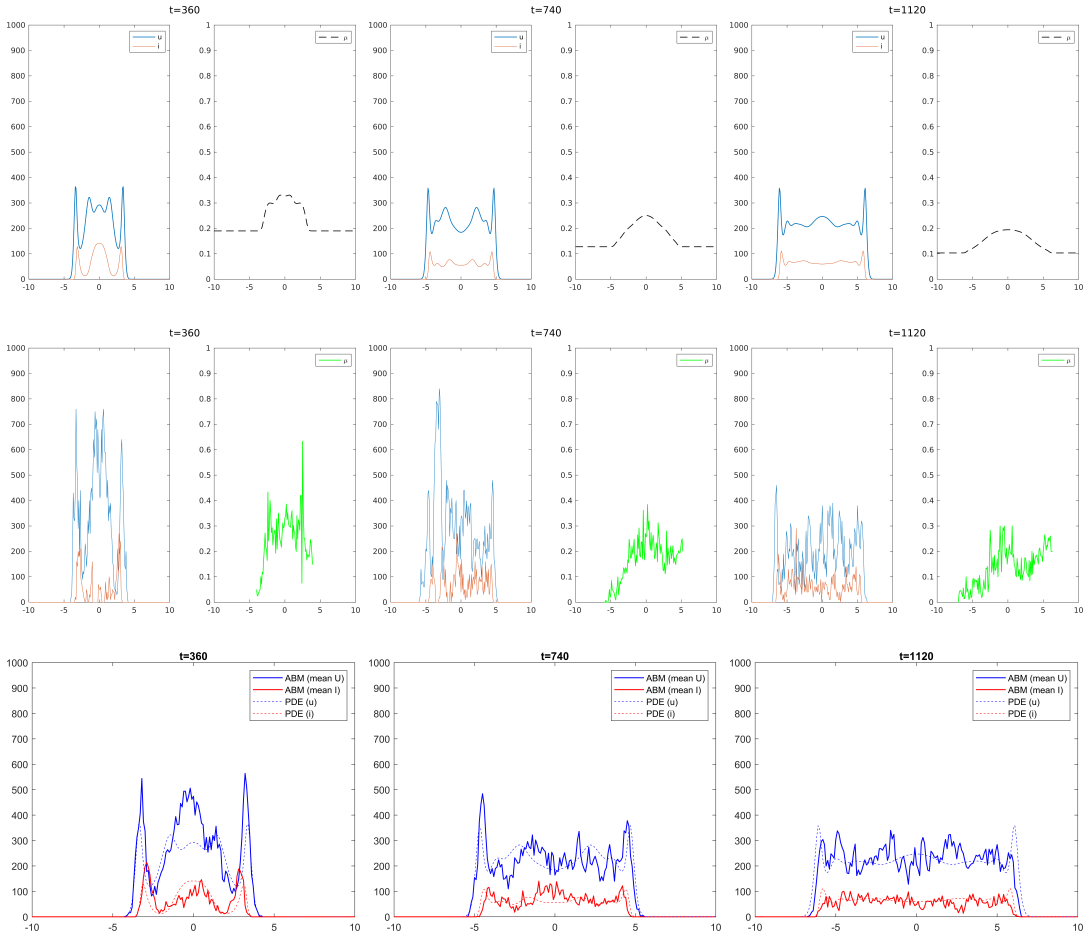

Figure 4.28: Evolution of cellular populations for a very large $\eta = 0.99$. The top three panels (PDE model) highlight a strong inhibitory effect on the growth of uninfected cells, which are much less abundant compared to previous cases. The epigenetic mean is drastically reduced, limiting the proliferative capacity of tumour cells. The central panels display the ABM results at the same time points, confirming that increasing η leads to a drastic reduction in the cellular population and to an almost complete inhibition of tumour growth. The bottom three panels show the average cellular density computed over 5 independent ABM simulations, offering a clearer picture of the mean behaviour under high epigenetic inhibition.

Interestingly, the epigenetic mean $\mu(x,t)$ varies significantly with η as well.

- For $\eta = 0.001$, the growth of uninfected cells is almost independent of y, leading to uniform profiles and a relatively high epigenetic mean. The values of μ remain high throughout most of the cellular domain, indicating that the cells maintain high proliferation rates. Looking at Figure 4.26, the epigenetic mean μ initially shows a value close to 0.9 in the central region, indicating weak epigenetic regulation. Even at later time points, it remains consistently high.

- For $\eta = 0.5$, epigenetic selection becomes more evident, reducing the presence of cells with high y values and causing the epigenetic mean to decrease. A gradient of μ is observed, with lower values in the central region and higher ones at the edges. Compared to the previous case, μ is noticeably lower.

- For $\eta = 0.99$, the growth of cells with high y is almost completely suppressed, resulting in a very low epigenetic mean. Epigenetic regulation is extremely strong, drastically reducing the values of μ. Areas with very low values of μ are observed, suggesting that most cells have lost their ability to proliferate. At this high value of η, the epigenetic mean μ is low, showing a strong inhibitory effect, and remains low.

4.5.4 Analysis of the influence of ζ on cellular behaviour

In this section, we analyse the behaviour of infected and uninfected cells for three distinct values of ζ: two extremes ($\zeta = 0$ and $\zeta = 0.0004$) and the standard case ($\zeta = 0.0002$). For each case, we examine the distribution of the two cell populations over time and their epigenetic mean, using both models, as per the previous discussions.

The influence of ζ is evident in the selectivity of the infection: as this parameter increases, the virus preferentially infects cells with a low epigenetic state y. This leads to significant differences in the spatial distribution of infected and uninfected cells.

For $\zeta = 0$, the infection does not have epigenetic dependence and spreads uniformly between tumour cells: the infection is widespread and the distribution of uninfected tumour cells remains relatively uniform.

As shown in Figure 4.29, the population of infected cells remains very limited, and tumour growth continues undisturbed. The epigenetic mean has low values and decreases over time, indicating an ineffective infection.

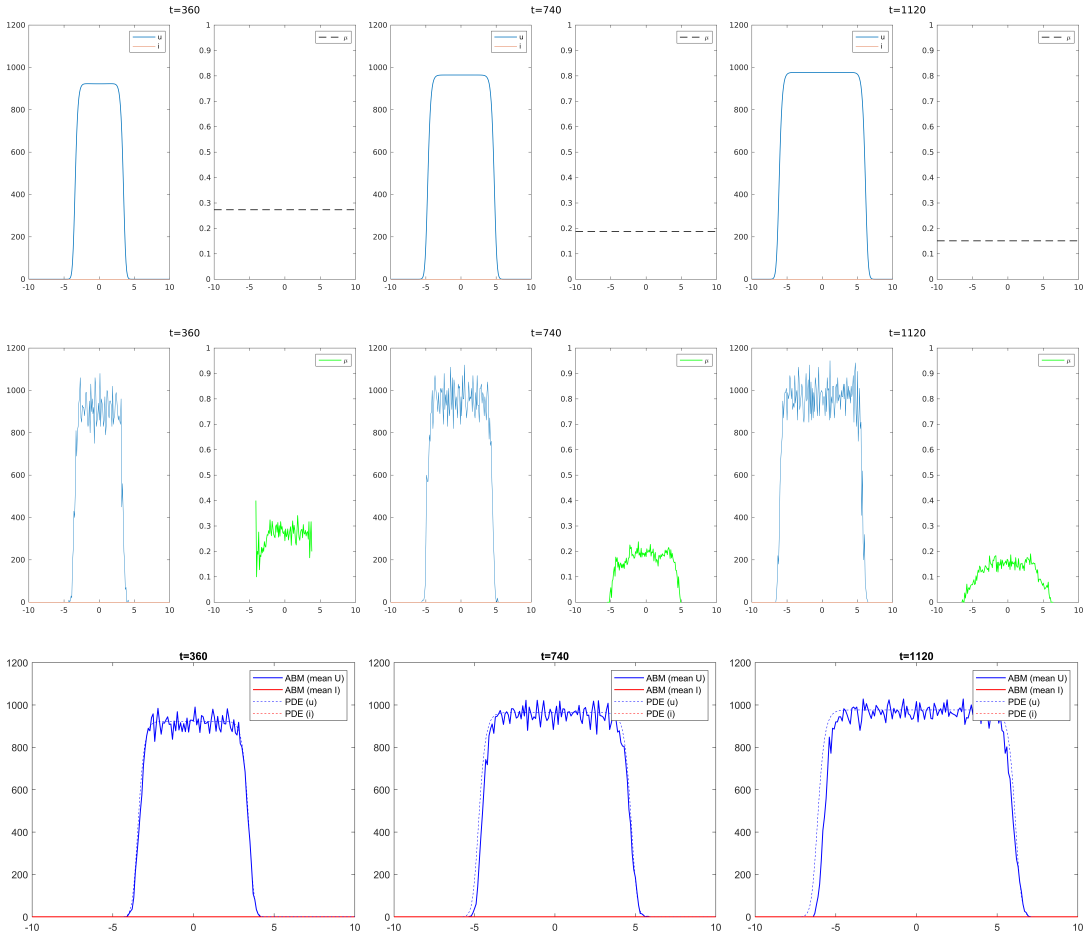

Figure 4.29: Evolution of the cell populations for $\zeta = 0$. The top three panels show the results of the PDE model at times $t = 360h$, $t = 740h$, and $t = 1120h$, with the blue curve representing uninfected cells (u) and the red curve representing infected cells (i). Uncontrolled tumour growth and a low presence of infected cells are observed. The epigenetic mean, shown in the right panels, remains low and constant. The central panels show the same time points for the ABM, confirming the behaviour observed in the PDE model, with small stochastic fluctuations. Notably, infected cells are scarcely present under this configuration. The bottom panels display the average cell density profiles computed over 5 independent ABM simulations, offering a smoothed representation of the system's behaviour in the absence of infection-induced epigenetic feedback.

For $\zeta = 0.0002$, tumour growth is limited compared to the previous case. The infection acts more effectively, preferentially targeting cells with low y values.

In Figure 4.30, we observe that the population of infected cells increases over time, and the epigenetic mean takes on intermediate values, indicating moderate selectivity of the infection.

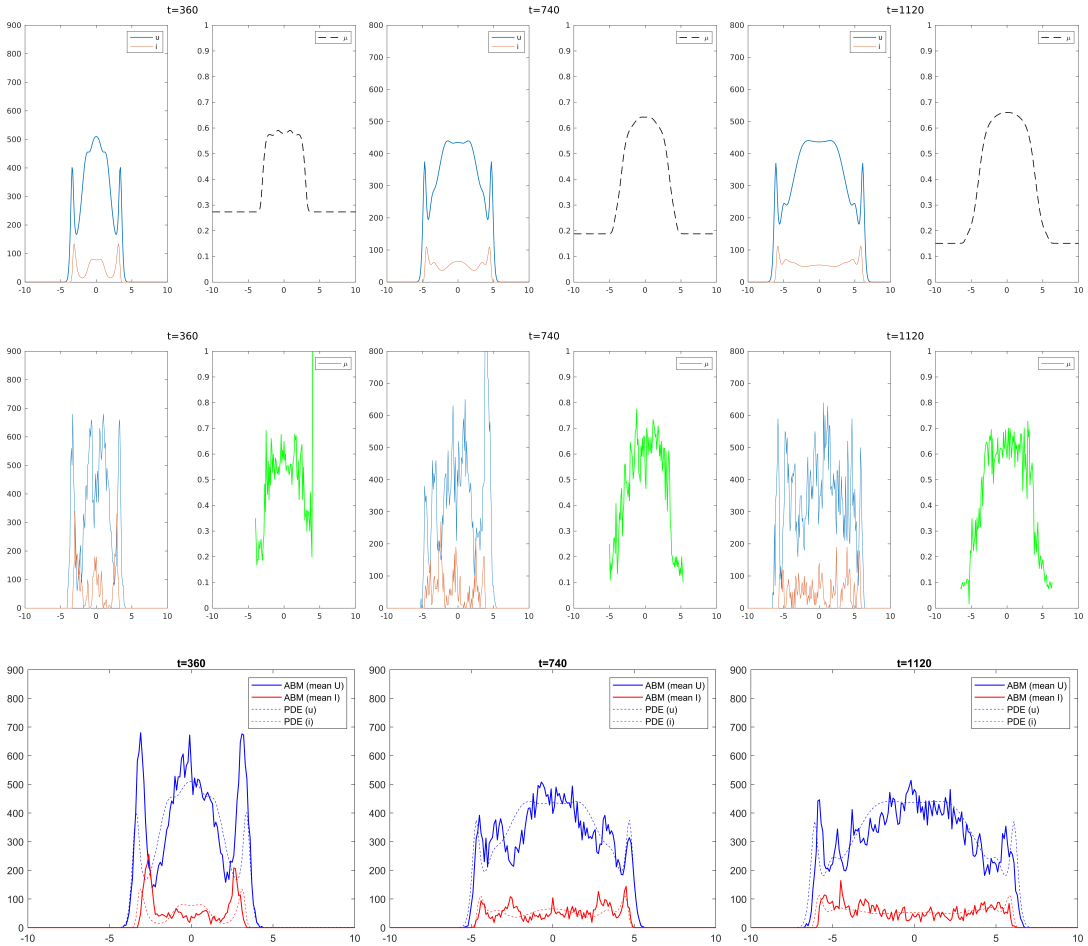

Figure 4.30: Evolution of cell populations for $\zeta = 0.0002$. A partially contained tumour growth and a non-uniform distribution of infected cells are observed. The epigenetic mean shows a more pronounced gradient. The PDE model (top row) results in a more homogeneous infection profile, whereas the ABM model (middle row) exhibits stronger local fluctuations, reflecting greater variability in infection dynamics at the individual-cell level. The bottom panels display the mean cellular densities obtained from 5 independent ABM simulations, providing a smoothed representation that captures the overall tendency while averaging out stochastic effects.

For $\zeta = 0.0004$, infection is highly selective and almost exclusively affects cells with low y. Uninfected tumour cells with high y values remain more preserved, and the infection front advances more slowly.

As shown in Figure 4.31, tumour growth is severely compromised and the cell density is significantly reduced. The epigenetic mean takes on higher values compared to previous cases, indicating a stronger effect of epigenetic regulation on tumour growth.

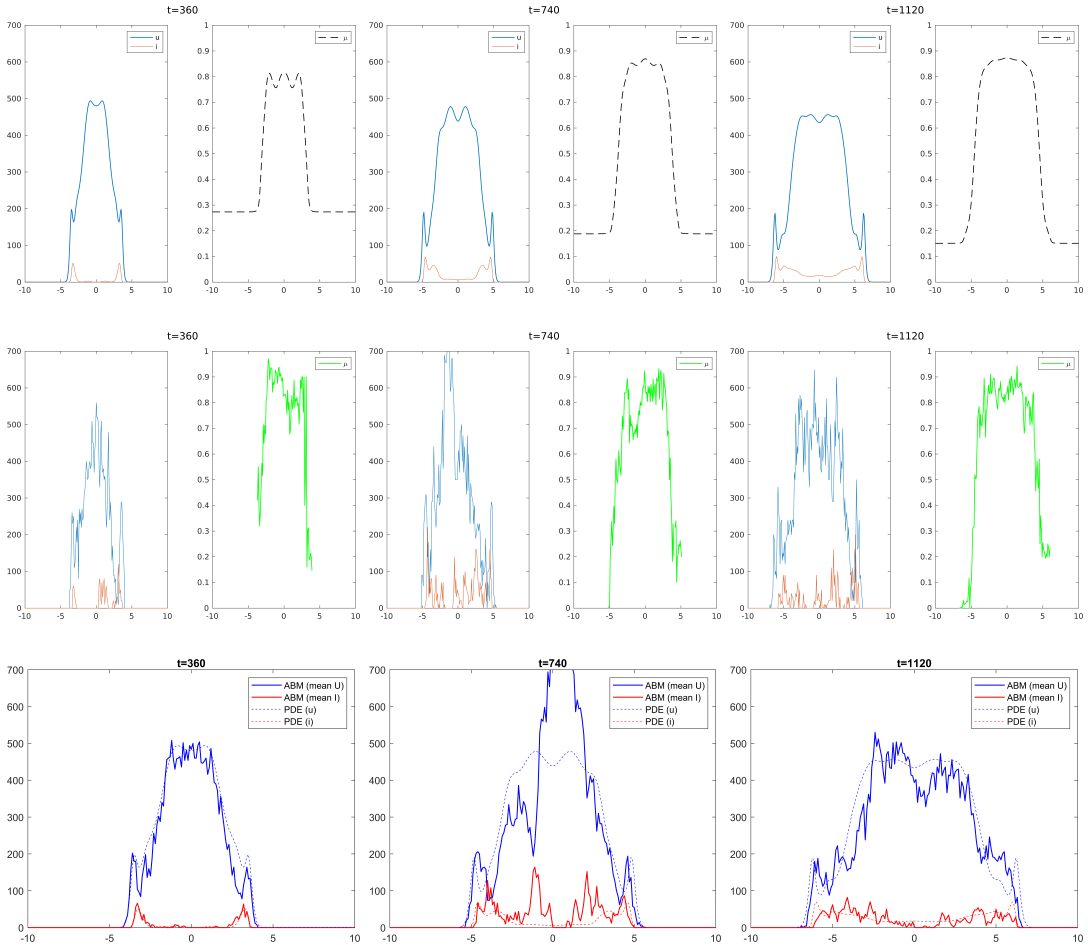

Figure 4.31: Evolution of cell populations for large $\zeta = 0.0004$. A strong containment of tumour growth and a more selective epigenetic profile are observed. In the PDE model (top row), the reduction in cell density is more gradual and spatially continuous, whereas in the ABM (middle row) the infection leads to a discontinuous and fragmented structure, suggesting a more aggressive selection effect and spatial heterogeneity. The bottom panels report the average cell densities across 5 independent ABM simulations, capturing the overall tendency of tumour suppression while smoothing out local stochastic variations.

The epigenetic mean $\mu(x,t)$ varies significantly with ζ: the higher the ζ is, the higher the mean becomes, reflecting the selectivity of the infection.

- For $\zeta = 0$, the epigenetic mean remains low and constant over time (in this case, a bell-shaped structure is absent), indicating a non-selective infection. The virus does not discriminate between cells with different epigenetic levels, allowing for unimpeded tumour growth and a more uniform distribution of the tumour population.
- For $\zeta = 0.0002$, the epigenetic mean shows a pronounced gradient, reflecting a preference of the infection for cells with low y. In this case, viral therapy is partially effective in reducing tumour growth, creating a selective effect on infected cells.
- For $\zeta = 0.0004$, the epigenetic mean is maximal, with a strongly selective distribution that limits tumour growth. The infection is extremely effective in targeting the most proliferative cells (with low y), sparing the less aggressive ones. This results in a more marked tumour containment effect, with a reduction in cell density in the central regions of the distribution.

From the plots, it is clearly observed that increasing ζ leads to a more effective tumour reduction, with progressive selection of cells based on their epigenetic state. The infection

becomes targeted and primarily affects the most sensitive cells, leaving behind those with a less favourable epigenetic profile for replication.

The analysis of parameters ζ and η highlights the key role of epigenetic regulation in tumour growth and in the effectiveness of viral therapy. Both parameters significantly influence the distribution of infected and uninfected cells, as well as the epigenetic mean of the entire cell population. However, they act in different ways: η regulates the epigenetic inhibition of uninfected cell growth. High values of η lead to a strong reduction in cell proliferation and a more widespread infection, with a lower epigenetic mean. When η is low, tumour growth is less regulated, allowing uncontrolled proliferation of tumour cells. Parameter ζ instead regulates the epigenetic dependence of viral infectivity. High values of ζ induce infection selectivity for low-y cells, leading to reduced tumour growth and increased epigenetic mean in the surviving cells. In contrast, low values of ζ result in a uniform distribution of the infection, limiting the effectiveness of viral therapy.

Therefore, combining a high value of η to limit tumour growth with a moderate value of ζ to optimize viral spread could represent an effective strategy to enhance the efficacy of virotherapy.

4.5.5 Analysis of the interaction between epigenetic inhibition and viral infectivity

The combined effect of high epigenetic inhibition and high viral infectivity is also a very interesting aspect to consider. This scenario represents a condition in which the growth of uninfected cells is strongly limited, while the spread of an oncolytic virus is more selective and targeted at cells with higher proliferative capacity. Later on, we evaluate the effect of increasing the initial number of infected cells, to verify whether a higher viral load can improve the effectiveness of therapy.

To test the combined effect of η and ζ, two sets of simulations were performed:

- **Case 1**: Simulation with $\eta = 0.99$ and $\zeta = 0.0004$, keeping the initial number of infected cells constant.
- **Case 2**: Same conditions as Case 1, but with an increased initial number of infected cells.

The following plots show the evolution of the distribution of uninfected and infected cells over time, comparing results obtained from the two models.

In Figure 4.32, left panel (ABM), two symmetric peaks with a high concentration of uninfected cells can be observed. The PDE model (right panel) shows a similar spatial distribution with minor differences due to model formulation. Infected cells are present in smaller quantities in both models, suggesting that the infection has just begun to spread. The absence of significant cellular populations in the central zone also suggests limited growth.

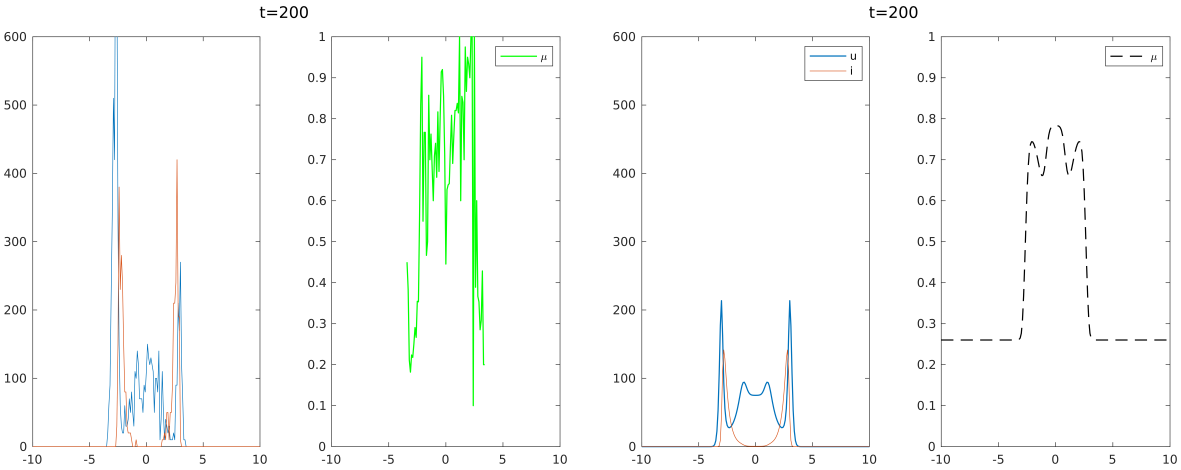

(a) Agent-Based model (b) PDE model

Figure 4.32: Distribution of infected cells (in red) and uninfected cells (in blue) at time $t = 200h$. The ABM (a) and PDE (b) models show similar patterns with two main peaks of uninfected cells and a compact distribution of infected cells.

As the simulation progresses, the infection spreads further, and an alteration in the spatial distribution of tumour cells is observed. The two initial peaks have decreased in height, and the distribution has expanded, indicating that the tumour has spread spatially. Infected cells increase slightly but remain in lower proportion compared to uninfected cells. The central part shows an increase in cell density, suggesting that the virus is beginning to target previously "uncolonised" areas.

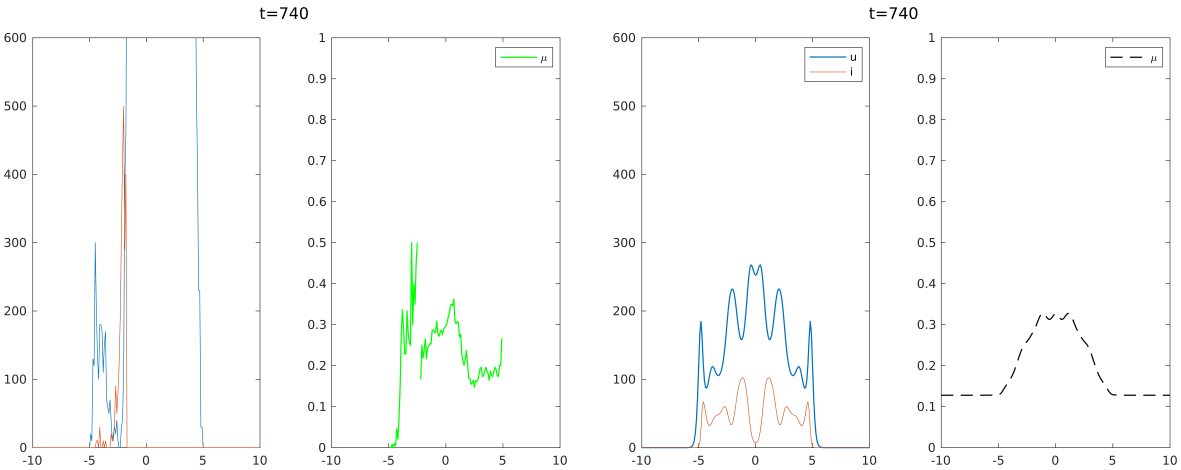

(a) Agent-Based model (b) PDE model

Figure 4.33: Distribution of infected and uninfected cells at time $t = 740h$. Both ABM (a) and PDE (b) models show more fragmented tumour growth compared to earlier times, with a greater spread of infected cells.

In the long term, there is a further reduction in the density of uninfected cells, indicating a progressive effectiveness of virotherapy. The distribution has become much more irregular and fragmented. Infected cells are present in many more areas compared to earlier time points, indicating an expansion of viral infection. The growth of uninfected cells continues, but is less structured than before, suggesting that the virus is altering the dynamics of proliferation.

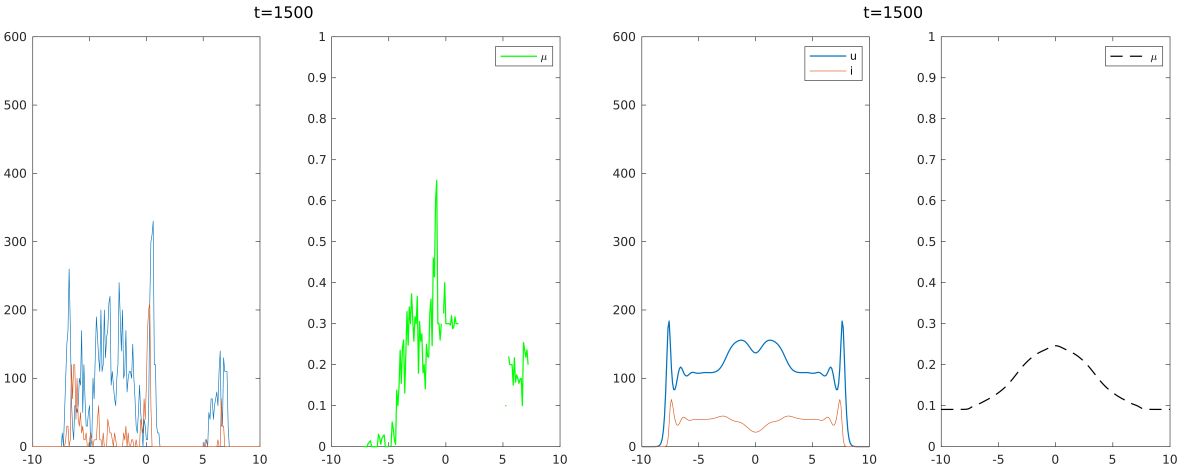

(a) Agent-Based model (b) PDE model

Figure 4.34: Distribution of infected and uninfected cells at time $t = 1500h$. A significant reduction in uninfected cell density is observed in both ABM (a) and PDE (b) models, indicating containment of tumour growth.

The three images in Figure 4.35 show only the behaviour of uninfected cells in the two models.

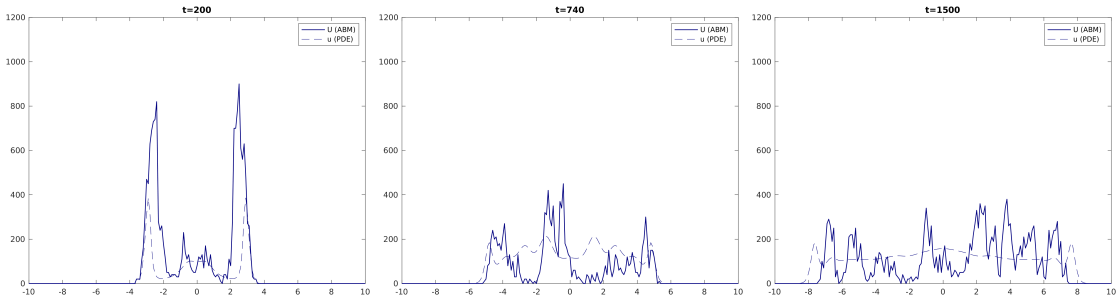

Figure 4.35: Comparison between the ABM (solid line) and the PDE model (dashed line) at three time points: $t = 200h$, $t = 740h$, $t = 1500h$. Both models reproduce tumour growth and the effect of viral therapy, but with differences in spatial distribution.

In this scenario, characterised by strong epigenetic inhibition of tumour growth and high selectivity of viral infection, very marked differences emerge between the ABM and the continuous PDE solution. As shown in the last two images in Figure 4.35, the behaviour of the cell population is significantly altered compared to previous cases, with drastically reduced tumour growth and a highly irregular spatial distribution.

At $t = 740h$, the ABM exhibits a very pronounced peak around $x \approx -2$, while the PDE solution shows a more diffuse profile, without such marked localised concentrations. This suggests that, in the discrete model, uninfected cells are aggregating in specific regions of the epigenetic space, temporarily escaping both epigenetic inhibition and the action of the virus. The comparison with the continuous solution highlights how the discrete approach generates more fragmented spatial structures and local peaks in cell density, an effect amplified by the intrinsic stochastic fluctuations.

Over time, this heterogeneity intensifies: at $t = 1500h$, multiple distinct peaks can be observed in the ABM distribution, while the PDE solution continues to show a uniform configuration. The combined effect of η and ζ thus has a significant impact on the system dynamics: the high epigenetic inhibition prevents widespread tumour cell growth, while the selectivity of the infection leads to an irregular spatial profile.

This discrepancy between the two models can be explained by several factors. First, the strong growth inhibition imposed by $\eta = 0.99$ significantly reduces the proliferative capacity of the cells, preventing a uniform expansion of the tumour population. Second, the high viral infectivity selectively targets cells with low y values, progressively eliminating the most proliferative populations and leaving only cells that are less susceptible to infection. In the discrete model, this process generates regions where growth is almost completely suppressed, alternating with areas where cells still manage to survive, forming the observed peaks.

Notably, the trend of the epigenetic mean $\mu(x,t)$ provides important information on the epigenetic state of the tumour population. In Figure 4.36, it can be observed that, over time, the epigenetic mean shows a decreasing tendency, indicating a progressive adaptation of the system to viral therapy.

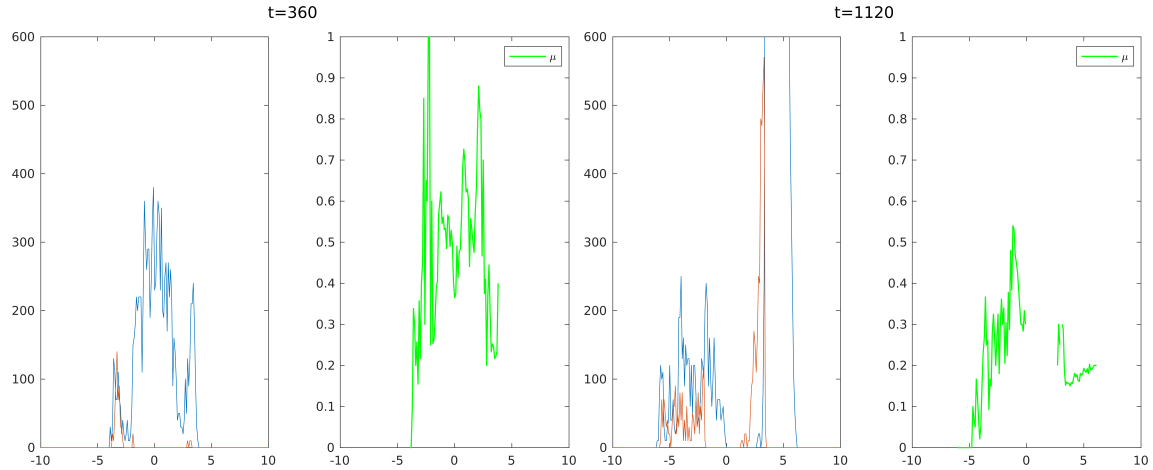

Figure 4.36: Evolution of the epigenetic mean in the ABM at time points $t = 360h$ and $t = 1120h$. Significant fluctuations are observed, with a gradual lowering of the average values of μ. The mean value continues to decrease, suggesting a progressive effect of virotherapy in selecting for cells with less aggressive phenotypes.

At $t = 360h$, the epigenetic mean varies mostly between 0.1 and 0.8, with some more pronounced fluctuations. The spatial distribution of μ appears more compact and localised compared to later times. A sharp peak above 0.8 indicates the presence of some regions with high epigenetic resistance, but most values remain below 0.5. This suggests that epigenetic inhibition is still effectively controlling cellular proliferation, preventing excessively rapid tumour growth.

At the later time point ($t = 1120h$), the epigenetic mean has shifted towards slightly higher values, with a more distributed growth. Fluctuations increase, suggesting that some tumour regions are developing greater epigenetic resistance. The peak near 0.8–0.9 disappears, but values more frequently around 0.4–0.5 are observed, suggesting more widespread tumour growth. This epigenetic heterogeneity may indicate that tumour cells are developing adaptive strategies to overcome epigenetic inhibition.

Now we present the average spatial distributions of infected and uninfected cells at three key time points, comparing results computed from the PDE model and from the ABM averaged over five simulations. Each panel shows both the PDE distribution and the ABM average side by side for direct visual comparison.

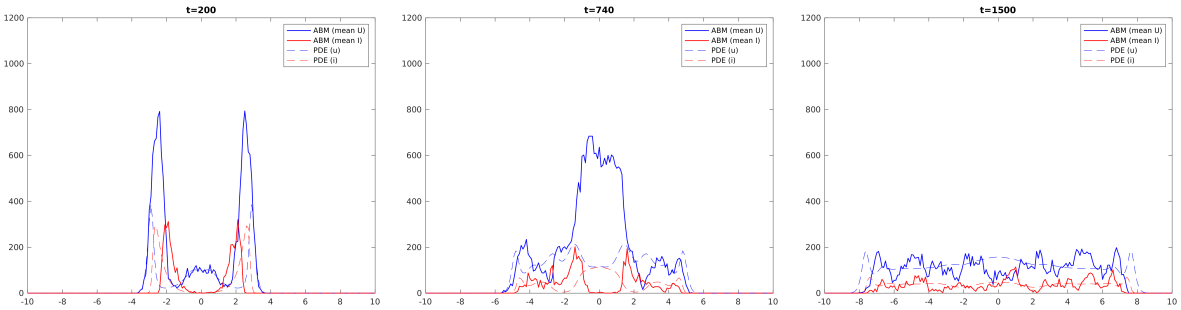

Figure 4.37: Average spatial distributions of infected (red) and uninfected (blue) cells at three time points. The solid blue line represents the average distribution of uninfected cells computed from five ABM simulations, while the solid red line shows the corresponding infected cell average. The dashed blue and dashed red lines represent the uninfected (u) and infected (i) cell densities, respectively, as obtained from the deterministic PDE model. The ABM average results display sharper peaks and minor local fluctuations, in contrast to the smoother, more symmetric profiles of the PDE.

At time $t = 200h$ (Fig. 4.37, left), both the PDE model and the averaged ABM simulations reveal a strongly symmetric distribution of uninfected cells, characterised by two prominent peaks located around $x \approx \pm 2$. This configuration indicates the persistence of the initial tumour structure, with minimal disruption from viral infection. Infected cells are still present in relatively low numbers, concentrated near the same spatial locations, and their distributions are noticeably narrower and lower in amplitude. The ABM average shows slightly more pronounced peaks and minor irregularities, reflecting residual stochastic fluctuations from individual simulations. Meanwhile, the PDE output remains smooth and regular. Notably, the central region ($x \approx 0$) contains negligible cell density, implying that viral propagation has not yet penetrated the inner domain. These results suggest that, at this early stage, virotherapy has initiated but not yet caused a significant structural shift in tumour distribution.

At $t = 740h$ (Fig. 4.37, centre), the dynamics of the infection have progressed considerably. The ABM simulations display a marked increase in the number of infected cells, with their spatial distribution overlapping partially with that of the uninfected cells, particularly in the central region of the domain. Compared to the PDE model, the ABM-derived distributions exhibit sharper peaks and higher irregularity, reflecting the spatial heterogeneity induced by the discrete and stochastic nature of the agent-based framework. The infected component reaches significantly higher values than at earlier times, while uninfected cells appear more confined around $x \approx 0$, suggesting a substantial disruption of the original tumour structure. Meanwhile, the PDE output remains smoother and more symmetric, albeit following a qualitatively similar progression.

At $t = 1500h$ (Fig 4.37, right), both models indicate an advanced phase of the infection, where the spatial distribution is broadly dispersed and the initial tumour pattern appears essentially dissolved. Infected cells are present at low density throughout the domain, while uninfected cells are distributed unevenly. The ABM average continues to display local fluctuations and spatial heterogeneity, reflecting the residual variability across simulations. By contrast, the PDE solution maintains a smoothed, centralised profile, although it also captures the general decay of tumour structure. Overall, the comparison reveals a qualitatively consistent progression between the two models, while highlighting differences in spatial detail due to stochastic noise and discrete interactions inherent in the ABM approach.

Increase in the initial number of infected cells

In this section, we analyse the cellular dynamics considering a higher initial number of infected cells compared to the previous simulation. This configuration allows us to evaluate whether

a greater initial viral load can improve the effectiveness of virotherapy.

At the initial time $t = 200h$ (Figure 4.38, left panel), two main peaks of uninfected cells can be observed with a denser distribution compared to the previous case: the presence of infected cells is already more evident respect to the previous seen case, indicating that the infection has spread more rapidly due to the higher initial viral load.

As the simulation progresses ($t = 360h$, Figure 4.38, right panel), the overall tumour density reaches its maximum. The infected cells spread more uniformly compared to the previous case, contributing to a more widespread infection of the tumour tissue.

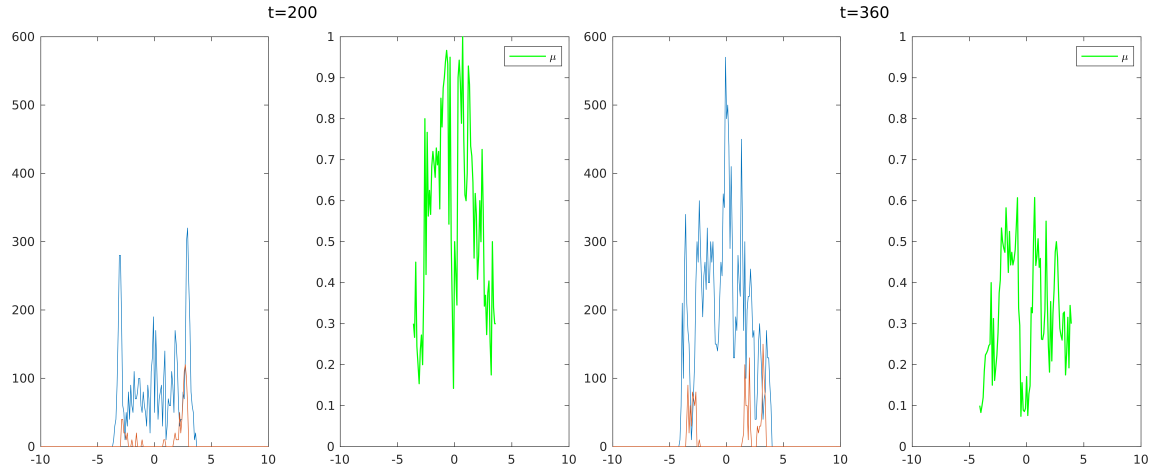

Figure 4.38: Distribution of infected (in red) and uninfected (in blue) cells in the ABM at time points $t = 200h$ and $t = 360h$. Compared to the previous simulation, a higher initial infection is observed, leading to a faster spread of the oncolytic virus.

Later ($t = 740h$, Figure 4.39, left image), a decrease in tumour cell density and an increase in the spread of infected cells is observed. This suggests that virotherapy has increased its effectiveness, progressively eliminating the tumour.

In the long term ($t = 1120h$ and $t = 1500h$, central and right panels in Figure 4.39), the density of uninfected cells drops sharply, indicating a strong action of the virotherapy. However, a slight increase in density is observed at $t = 1500h$, suggesting a possible adaptation of the tumour to the viral infection.

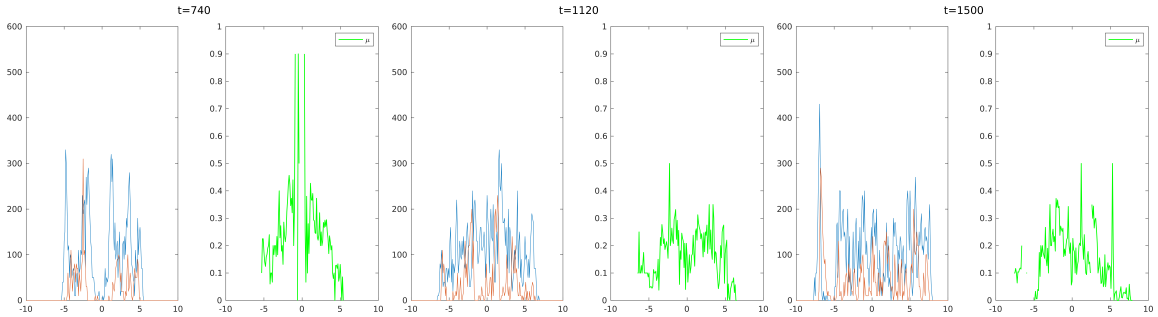

Figure 4.39: Cell distribution at times $t = 740h$, $t = 1120h$, and $t = 1500h$. The density of uninfected cells decreases significantly, indicating the effect of virotherapy.

The three images in Figure 4.40 show only the behaviour of uninfected cells in the two models.

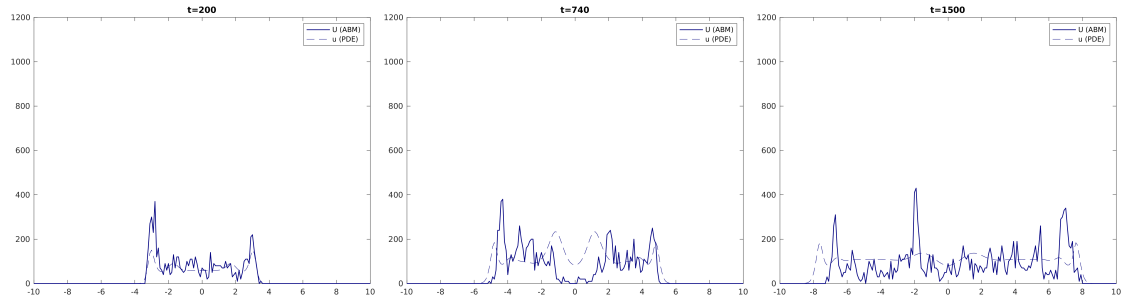

Figure 4.40: Comparison between the ABM (solid line) and the PDE model (dashed line) at three time points: $t = 200h$, $t = 740h$, $t = 1500h$, in the case of increased initial viral load. The spatial distribution and suppression of uninfected tumour cells are visibly affected by the stronger virotherapy.

In this configuration, characterised by a higher initial concentration of infected cells, virotherapy exhibits an even stronger influence on the spatial and temporal dynamics of tumour cell populations. As seen in Figure 4.40, both models continue to describe tumour suppression, but notable differences emerge with respect to the previous case in terms of spatial localisation and magnitude of cell density.

At $t = 200h$, the ABM shows an early suppression of tumour cells, with a narrow peak around $x \approx -3$, much lower in intensity compared to the analogous time point in the lower-infection scenario. The PDE model reflects a similar trend, with a smooth and modest distribution centred slightly right of the ABM peak. This indicates that the increased viral presence leads to a rapid reduction in the number of uninfected cells from the beginning, limiting early tumour expansion.

By $t = 740h$, the ABM distribution remains highly fragmented but with lower peak values compared to the earlier case. The usual aggregation around specific regions (e.g., $x \approx -4$ and $x \approx 3$) is still present but appears more subdued, suggesting that even those cells temporarily escaping infection are now under greater pressure. The PDE solution, in contrast, shows a broader yet consistently reduced density profile. The comparison again highlights how the ABM captures sharp local effects and variability, while the PDE offers a smoothed, averaged dynamic.

At $t = 1500h$, the effect of the increased viral pressure becomes even more evident. The ABM shows multiple isolated peaks, as in the lower infection case, but with considerably reduced amplitude, none exceeding 300 in cell count, unlike the >400 peaks previously observed. The PDE profile remains uniform and low across space, confirming the overall suppression of tumour activity. Notably, the distance between the ABM peaks suggests isolated survival niches rather than coordinated regrowth.

Comparing the two scenarios (Fig. 4.35 and Fig. 4.40), the main difference lies in the extent of suppression and fragmentation. The higher number of infected cells amplifies the selective pressure, accelerating the elimination of susceptible tumour cells and further impeding the emergence of dominant subpopulations. While the discrete ABM still permits the formation of isolated clusters due to stochastic effects and local variability, their size and frequency are significantly reduced. The PDE model, by its nature, smooths out these variations, but even it reflects the overall diminishing trend. This highlights the importance of initial infection load in determining the long-term success of virotherapy, especially in systems with strong epigenetic constraints.

The analysis of the results shows that the combination of high epigenetic inhibition and selective infectivity has a significant impact on tumour growth. The proliferation of uninfected

cells is notably reduced compared to previous cases. The PDE model predicts a more homogeneous distribution compared to the ABM, which reveals a more fragmented tumour growth and local fluctuations. The trend of the epigenetic mean confirms a selective effect of the therapy, leading to a progressive reduction of the more proliferative phenotypes. Moreover, increasing the initial viral load accelerates the effect of virotherapy, leading to a faster reduction of tumour cells. Overall, high epigenetic inhibition, combined with targeted selectivity of the oncolytic virus and an increased initial number of infected cells, represents an effective strategy to contain tumour growth. However, the value of the initial viral load still needs to be optimised to maximise therapeutic efficacy and avoid potential resistance phenomena. It may also not be clinically viable for every tumour, given the difficulty of obtaining a generous initial infection for some forms of cancers (glioblastomas or some carcinomas, for instance).

Chapter 5

Conclusions and future developments

The analysis conducted on the numerical simulations has made it possible to identify the key dynamics that govern the effectiveness of virotherapy, highlighting the role of fundamental biological parameters.

The simulations presented allow us to evaluate the behaviour of two mathematical models — continuous (PDE) and discrete (ABM) — in describing the evolution of a tumour undergoing virotherapy.

One of the most significant results emerging from the simulations is the qualitative consistency between the two modelling approaches, despite their different nature: the PDE model describes the average behaviour of the cell population in a continuous manner, whereas the ABM reproduces the individual dynamics of cells on a discrete grid.

The comparison shows that both models predict similar spreads of infection, which propagates from the tumour centre. Differences are observed in the diffusion speed and in the spatial distribution of epigenetic susceptibility. In particular, the ABM tends to show greater granularity and local variability, with more irregular infection fronts. The PDE model, on the other hand, produces smoother and more regular profiles.
From a computational perspective, the PDE model is more efficient for simulating large spatial domains and long time spans, while the ABM offers more detailed insight into local cellular dynamics, such as epigenetic mutation and cell competition. The possibility of deriving the continuous model as the limit of the ABM reinforces the theoretical robustness of their complementarity.

In the PDE model, an infection wave propagates toward the edges of the domain, followed by a gradual decrease in the density of uninfected cells. Infection shows a "biphasic" effect: it initially slows tumour growth, but later, due to epigenetic selection, some cells manage to escape infection by stabilising in peripheral regions. In the ABM, the dynamics are more complex and realistic, with significant local fluctuations in infection density. These emerging behaviours are not immediately visible in the continuous model but may be critical to understanding therapeutic resistance. Temporal evolution also shows that the response of the system is not monotonic: in some simulations, after an initial phase of tumour regression, a resurgence of growth occurs due to epigenetic adaptation. This phenomenon is particularly evident in cases with low values of ζ, where the virus has low infectivity even toward susceptible cells.

It is also interesting to note that the trend of the epigenetic mean over time clearly shows the selection process induced by viral pressure: in the early phases of the simulation, the mean tends to increase, indicating that the virus preferentially eliminates cells with low y (more proliferative but also more resistant), leaving space for more susceptible but less aggressive

cells. However, in many cases this trend later reverses, indicating recolonization by less susceptible but more proliferative cells. Comparison between the two models reveals that the ABM produces a more *noisy* and variable epigenetic mean due to intrinsic stochastic fluctuations. The PDE model, on the other hand, shows more *regular* curves but is sometimes less sensitive to local phenomena. In both cases, the epigenetic mean proves to be a useful indicator for predicting treatment efficacy and identifying emerging resistance phenomena.

Furthermore, simulations show that in the initial phases, epigenetic variance tends to increase slightly, then decreases over the course of the infection: this phenomenon reflects the selection of a more resistant phenotypic subgroup. However, in scenarios with low infectivity or high epigenetic plasticity, the variance remains high or even increases over time, suggesting a residual evolutionary potential of the tumour that could undermine therapeutic success. The ABM is particularly effective in highlighting these effects, whereas the PDE model, although confirming the general trends, does not always capture the formation of highly resistant subpopulations.

Moreover, simulations show that for high η values, the cell population concentrates around phenotypes with low viral susceptibility: the system rapidly selects for low-y cells, which escape infection but grow more slowly. This appears beneficial from a therapeutic point of view, but also tends to favour long-term tumour survival. In such scenarios, infection initially reduces tumour mass but fails to eliminate it: the tumour adapts, generating a population of "silent" but resistant cells. On the other hand, for low values of η, growth remains relatively uniform across the entire epigenetic range, and the virus manages to infect a larger fraction of cells. This can lead to high residual epigenetic variability, potentially undermining the long-term effectiveness of the therapy. Thus, the optimal choice of η is a trade-off between immediate efficacy and prevention of tumour relapse.

The parameter ζ instead regulates the infection rate as a function of the epigenetic value y. It defines how sensitive the virus is to phenotypic susceptibility: high values imply aggressive infectivity even toward resistant cells, while low values make the virus more selective, infecting only highly vulnerable cells. We show that a virus with high infectivity (ζ high) can rapidly reduce tumour mass but risks eliminating cells that serve as a natural obstacle on tumour growth. This can create unstable dynamics, where the most aggressive cells survive and evade infection, regenerating a tumour that is harder to control. In scenarios with low ζ, the infection is selective and controlled: the virus primarily infects high-y cells, leaving the more resistant cells intact. This leads to a slower reduction of the tumour but results in greater stability of the therapy over time. Once again, optimising the ζ parameter depends on the specific biological context and the desired therapeutic strategy.

Finally, the interaction between η and ζ, assessing the combined effect of epigenetic inhibition of growth and viral infectivity, confirms that there is no universally optimal combination. The effectiveness of virotherapy depends nonlinearly on the balance between the two parameters. In particular, scenarios with low η and high ζ tend to rapidly eliminate tumour cells but with a higher probability of regrowth, due to the survival of escaping phenotypes. Conversely, combinations with high η and low ζ result in a more moderate yet longer-lasting therapeutic effect. It is interesting to note that initial epigenetic variability plays a key role in the system's response: highly heterogeneous tumours are more resilient, whereas initially more homogeneous tumours respond better to therapy, regardless of the values of the two parameters. This suggests that the initial diagnosis of the tumour's epigenetic profile could guide the personalisation of virotherapy to a better outcome.

5.1 Final conclusions and further directions

The simulations developed in this thesis demonstrate the great potential of mathematical modelling in understanding and optimising oncologic virotherapy.

The main conclusions that emerged are:

- The effectiveness of virotherapy is strongly influenced by the epigenetic variability of the tumour cell population.
- The parameters η and ζ play a crucial role in balancing viral selectivity, aggressiveness, and cell survival.
- Epigenetic adaptation of the tumour can lead to resistance phenomena, even in the presence of initially effective infections.
- The epigenetic mean and variance are key indicators for monitoring therapeutic response and predicting its evolution.

This work suggests that an integrated approach, based on multiscale simulations and experimental data, could significantly contribute to the development of personalised virotherapies. There are still many unanswered and interesting questions. Among them, let us suggest a few of relevance to us.

1. Extension to multidimensional spatial domains: the simulations conducted were performed in a one-dimensional domain for simplicity and clarity. However, the real tumour environment is three-dimensional, with complex and anisotropic structures. Extending the PDE and ABM to two and three dimensions would allow for a more realistic description of viral spread and tumour growth, especially in the presence of physical barriers or oxygen gradients. In this regard, some initial results in 2D are presented and briefly discussed in the Appendix.
2. Integration with biological and clinical data: a crucial step for model validation is integration with experimental data. Using real epigenetic profiles, clinical parameters and data obtained from tumour biopsies could improve model accuracy and make them decision-support tools in therapy. Bridging the gap between mathematical theory and clinical practice is one of the most ambitious yet promising challenges.
3. Adaptive models and machine learning: integrating with artificial intelligence techniques such as machine learning and Bayesian optimisation could enable automatic calibration of models based on available data and prediction of therapy progression in real time. In particular, machine learning could be used to estimate optimal parameters (η, ζ) for a specific patient, thereby personalising the therapeutic approach.
4. Study of interaction with other therapies: as currently investigated in a number of clincal trials, virotherapy is particularly promising when combined with immunotherapy, radiotherapy, or epigenetic treatments. Introducing additional biological mechanisms into the models, such as an adaptive immune system response or cyclic drug administration, could provide new insights into how to maximise the effectiveness of combined therapies.

These perspectives show how mathematics, when integrated with computation and biological data, can offer a significant contribution to the medicine of the future. Oncolytic virotherapy could greatly benefit from reliable predictive models capable of guiding effective and personalised therapeutic decisions, even at the stage of clinical trials or "proof of concepts" for experimental cures.

Appendix A

Two-dimensional spatial models

Introduction

The analysis presented in this Appendix are still under development and represent an extension of the one-dimensional model described in the previous chapters. The aim of this section is to present the initial results of simulations carried out on the two-dimensional realisation of the previously discussed mathematical models. This allows us to consider a more complex and realistic geometry for studying the spread of infected and uninfected cells in a biological environment. Although the work is not yet complete, simulations provide a useful preliminary overview for understanding the potential of the approach and outlining possible future research directions.

A.1 PDE Model

In one-dimensional models, the simulation of cellular dynamics develops along a single spatial dimension (x), limiting the ability to explore phenomena occurring in more complex environments. However, to more realistically represent the spread of cells in a biological environment or tissue, it is necessary to move to a two-dimensional settings. Radial symmetry is a useful assumption: in infections that spread from a central point, or in contexts where cell diffusion occurs uniformly around a point (such as tumour growth or the spread of an infection), radial geometry provides an accurate framework.

The two-dimensional spatial model with radial symmetry differs from the one-dimensional model in that we now consider the radial distance from the centre as the main variable determining interactions between cells. Furthermore, the simulation domain is extended from a line to a two-dimensional plane, creating a radial grid in which the positions of the cells are defined in terms of radii and angles.

A.1.1 Context

In our PDE model in two spatial dimensions, we consider the distribution of both infected and uninfected cells within a two-dimensional domain. The spatial grid is defined using radial coordinates, where each cell in the grid represents a region of the domain. Radial symmetry is employed to define the distance between cells and to model radial flows.

The main modification compared to the one-dimensional model lies in the definition of the spatial grid. In a one-dimensional system, the grid consists of nodes along a single line, whereas in the two-dimensional model, the grid is defined over a plane. Each point in the grid represents a region in the radial plane, where the cells move and interact depending on their distance from the centre.

The extension to the two-dimensional case entails a change in the mathematical formulation, numerical discretisation and simulations. In this section, we present the newly developed

model, the modifications in the Matlab code, and the results obtained, concluding with a comparison between the outcomes in the two cases: one with a single spatial dimension and the other with two spatial dimensions.

A.1.2 Model equations

In the model under consideration, the spatial variables are represented by $x \in \Omega$, where Ω is the spatial domain. For the 2D radial model, we assume that the domain Ω has radial symmetry, i.e., it depends only on the distance r from the centre, and not on any angular directions.

Due to this symmetry, the cell densities depend only on the variable r for the spatial component, and not on any angle. Therefore, we can rewrite the system assuming that the equations depend only on r.

In 2D with radial symmetry, the Laplacian in polar coordinates is expressed as:

$$\nabla^2 = \frac{\partial^2}{\partial r^2} + \frac{1}{r}\frac{\partial}{\partial r}$$

so that, we need to modify the spatial Laplacian terms Δ_x in the original equations accordingly.

Equation for uninfected cells

The equation for $u(t, x, y)$ in the 2D radial model becomes:

$$\partial_t u(t,r,y) = D_y \Delta_y u(t,r,y) + D_r \frac{1}{r}\partial_r(r\partial_r u(t,r,y)) + p\Big(r(y) - \frac{\rho(t,r)}{K}\Big)u(t,r,y) - \beta(y)\ u(t,r,y)\ i(t,r)$$

Equation for infected cells

The equation for $i(t, x)$ in the 2D radial model becomes:

$$\partial_t i(t,r) = D_r \frac{1}{r}\partial_r(r\partial_r i(t,r)) + i(t,r)\int_Y \beta(y)u(t,r,y)dy - qi(t,r)$$

Density equation

The equation for $\rho(t, x)$ in the 2D radial model becomes:

$$\rho(t,r) \coloneqq \int_Y u(t,r,y)dy + i(t,r)$$

Putting all the above together, the resulting equations for the 2D radial model are:

$$\begin{cases} \partial_t u(t,r,y) = D_y \Delta_y u(t,r,y) + D_r \frac{1}{r}\partial_r(r\partial_r u(t,r,y)) + p\Big(r(y) - \frac{\rho(t,r)}{K}\Big)u(t,r,y) - \beta(y)\ u(t,r,y)\ i(t,r) \\ \partial_t i(t,r) = D_r \frac{1}{r}\partial_r(r\partial_r i(t,r)) + i(t,r)\int_Y \beta(y)u(t,r,y)dy - qi(t,r) \\ \rho(t,r) \coloneqq \int_Y u(t,r,y)dy + i(t,r) \end{cases}$$

The functions $r(y)$ and $\beta(y)$ remain identical, since they do not depend on spatial variables.

A.1.3 Modifications to the matlab code

The Matlab code has been modified to implement the model in two spatial dimensions, using the radial symmetry. In the one-dimensional case, diffusion occurs along a single spatial direction, whereas in the two-dimensional case, diffusion is described along a radial direction and an epigenetic one, as in the one-dimensional case. The main modifications concern the spatial discretisation and the handling of diffusion in the two spatial directions.

1D code

In the code for the one-dimensional model, the spatial grid is defined by a variable x, divided into uniform intervals of length dx. The solution u is calculated on a grid of size N_x, and the temporal evolution takes place over a time interval T_{pde} with a time step dt. The diffusion and reaction equations are implemented using a finite difference method for both spatial and temporal variables.

2D code with radial symmetry

In the two-dimensional case, the spatial grid is defined by the radial variables r and epigenetic variables y. To exploit the radial symmetry, the radial variable r is divided into uniform intervals of length dr, while the epigenetic variable y is discretised with a step size of dy. Diffusion is calculated separately in the two directions, radial and epigenetic. Radial diffusion, due to the polar geometry, includes a correction term arising from the dependence on r, which modifies the diffusion term at the boundaries.

Thus, the main modifications concern the definition of **radial diffusion**: in the two-dimensional case, radial diffusion is calculated differently compared to the one-dimensional case due to the radial geometry and the transformation of the Laplacian in this new context. The formula for radial diffusion therefore includes an additional term that accounts for the variation of the distance r in the radial direction. This term is represented as:

$$\frac{1}{r}$$

A.1.4 Results of simulations

The analysis of the numerical simulations of the 2D radial model relies on two main plots: the first represents the spatial distribution of uninfected cells *u(t,r,y)*, while the second shows the distribution of infected cells *i(t,r)*. Both highlight the radial nature and the temporal evolution of the biological dynamics being modelled.

Spatial evolution of uninfected cells

The images in Figure A.1 show the spatial evolution of the tumour cell density of uninfected cells $u(t, r, y)$ in a two-dimensional radial domain over time. Each figure represents a snapshot of the spatial distribution at three distinct time points: $t = 101h$, $t = 501h$, and $t = 1001h$. The effect of radial diffusion and interaction with the surrounding environment is clearly observable.

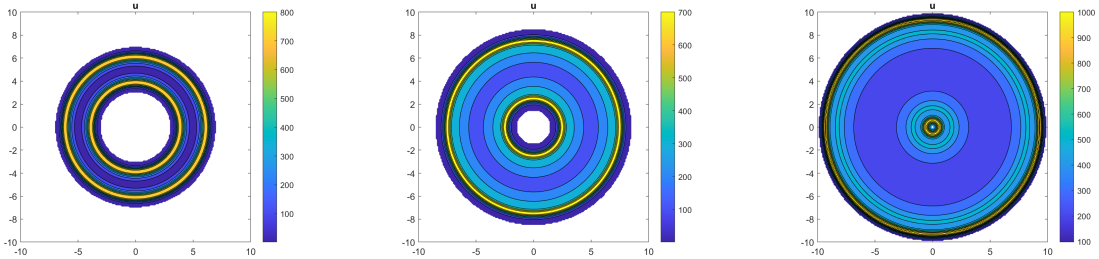

t = 101h. t = 501h. t = 1001h.

Figure A.1: Spatial evolution of the uninfected tumour cell density $u(t, r, y)$ in the two-dimensional radial domain at three successive time points ($t = 101h$, $t = 501h$, and $t = 1001h$). The images show the radial symmetric dynamics of cells from an initial configuration concentrated in an annular region, with gradual expansion towards the centre and periphery. The dynamics are governed by diffusion, logistic growth, and interaction with the total density $\rho(t, r)$.

t = 101h. At this initial stage, a *ring-shaped* distribution is observed. The uninfected cells are concentrated in an intermediate radial band, leaving the centre of the domain empty. This structure is consistent with the initial condition set in the model, where the cell population is initially confined to a narrow radial interval. The absence of density at the centre reflects the initial configuration and the embryonic stage of radial diffusion.

t = 501h. At 501 hours, a marked **radial expansion** of the uninfected tumour population is evident. The ring has expanded both inward and outward, reducing the central void and increasing the domain coverage. The density appears more uniform than at the initial time point, yet a denser peripheral region is still clearly visible. This behaviour is consistent with the diffusion and growth mechanism predicted by the model: cells proliferate depending on the availability of space and nutrients, spreading radially.

t = 1001h. At the last time point analysed, the distribution has reached an almost entirely centred and homogeneous profile, with the highest density shifted towards the centre. The previously empty region is now fully colonised, while the outer ring has expanded to the edges of the domain. This suggests that the cells have reached a balance between diffusion and saturation, with density regulated by the logistic term and the diffusion coefficient. The resulting profile is consistent with advanced tumour expansion in a confined radial environment.

These trends reflect the interaction between diffusion and reaction terms in the PDE formulation. Spatial diffusion works to homogenise the distribution, while the reaction terms $p(r(y) - \rho/K)$ and $-\beta(y)ui$ model logistic growth and the reduction of healthy cells due to infection, respectively. The decrease in density in the inner regions is consistent with a greater presence of infected cells, which deplete resources from the uninfected cells and reduce their population through the contagion process. The concentric contours observed indicate a radially symmetric distribution.

Spatial evolution of infected cells

Figure A.2 shows the radial distribution of the infected cell density $i(t, r)$ at the three time points considered above.

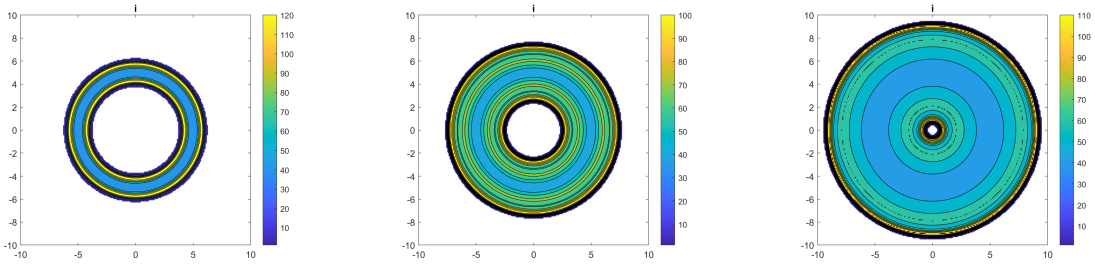

t = 101h. t = 501h. t = 1001h.

Figure A.2: Evolution of the spatial density of infected cells $i(t, r)$ in the 2D radial domain at three different time points: $t = 101h$, $t = 501h$, and $t = 1001h$. The progressive extension of the infection starting from an initial (thin) ring is observed, with penetration towards the centre and an increasingly wider coverage of the domain over time.

t = 101h. At the initial time point, the distribution of infected cells $i(t, r)$ is localised in a thin ring around the centre of the domain. This configuration reflects the initial infection being confined to the area where uninfected tumour cells are present at the start. The infection has not yet significantly spread but is already active in the tumour region, suggesting an initial interaction between the two cell populations.

t = 501h. After approximately 500 hours, the diffusion of infected cells has significantly increased. There is an expansion both inward and outward, with a progressive filling of the central region of the domain. The infected density has increased and is more evenly distributed along the radial direction, a sign of the effectiveness of diffusion and continuous interaction with the uninfected cells.

t = 1001h. In the final phase, the distribution of infected cells covers almost the entire domain. The density reaches a maximum in the central zone and gradually diminishes towards the outer regions. The resulting configuration suggests that the system is approaching an almost spatially homogeneous state, with a fully diffused and stabilised infection, consistent with the dynamics predicted by the model and the domain saturation conditions.

These behaviours result from the interaction between diffusion, which tends to expand the distribution, and the growth term $\int_Y u(t, r, y)dy$, which is maximised in areas where uninfected cells are abundant. The concentration gradually decreases towards the outer regions, where the number of uninfected cells is higher and contagion is less effective. The purple boundary represents the outer limit of infection spread, where the density of infected cells is almost zero due to the balance between diffusion and the natural death term.

Comparison between uninfected and infected cells

From the comparison between the two dynamics, it is observed that the uninfected tumour cells expand more rapidly than the infected ones, reaching the centre of the domain in shorter times and colonising the entire area with greater intensity. In contrast, the infected cells exhibit a more gradual evolution: they begin diffusion from the same annular region but take longer to reach a uniform profile and a similar spatial coverage. This behaviour is consistent with the infection mechanism predicted by the model, in which the infected population develops secondarily, depending on the presence of uninfected cells.

Visually, the representation using contour plots (`contourf`, which represents spatial density through a continuous colour scale) allows highlighting spatial density variations: areas with warmer colours (yellow and orange) indicate regions of **higher cell density**, while cooler shades (blue and light blue) represent areas with **low or no concentration**. Temporal evolution is thus reflected not only in the geometric shape of the distributions but also in the colour transition from blue to yellow as cells spread and multiply throughout the domain.

This transition is clearly visible, for instance, in the image of infected cells at $t = 101h$ (Figure A.2, left), where the distribution is almost entirely blue with a thin yellow ring indicating the initial infection zone. In the subsequent images, the yellow colour progressively expands, indicating cell growth.

In the case of uninfected cells (Figure A.1), it is observed that the yellow ring is initially well-defined, but quickly extends both inward and outward by $t = 501h$, occupying most of the domain by $t = 1001h$. The intermediate shades (light blue and light green) that develop between the rings indicate transition and active diffusion areas, consistent with the dynamics predicted by the PDE system. In summary, the transition from cool to warm colours reflects the intensifying cell presence over time, providing an immediate and intuitive reading of the spatial progression of infection and tumour growth.

The concentric radial structure observed in both graphs emphasises the symmetric nature of the problem, while the complementarity between the distributions of $u(r, t)$ and $i(r, t)$ highlights a natural balance of resources and contagion.

A.1.5 Different initial conditions

This section analyses three representetive simulations of the PDE mathematical model to study the behaviour of infected and uninfected cells in two spatial dimensions, with variations in the initial conditions: the goal is to compare the evolution of growth and interaction between the cells.
The simulations vary the initial parameters of the infected cells, while keeping those of the uninfected cells constant in the first and second cases, and modifying them in the third case:

- **Case 1**: $R_u = 2.6$ mm, $R_i = 0.6$ mm, $h_{uninf} = 0.5$*K, $h_{inf} = 0.1$*K.
- **Case 2**: $R_u = 2.6$ mm, $R_i = 1$ mm, $h_{uninf} = 0.5$*K, $h_{inf} = 0.2$*K.
- **Case 3**: $R_u = 2$ mm, $R_i = 2.4$ mm, $h_{uninf} = 0.4$*K, $h_{inf} = 0.3$*K.

The following images show the evolution of cell growth in the three simulations at two different time steps:

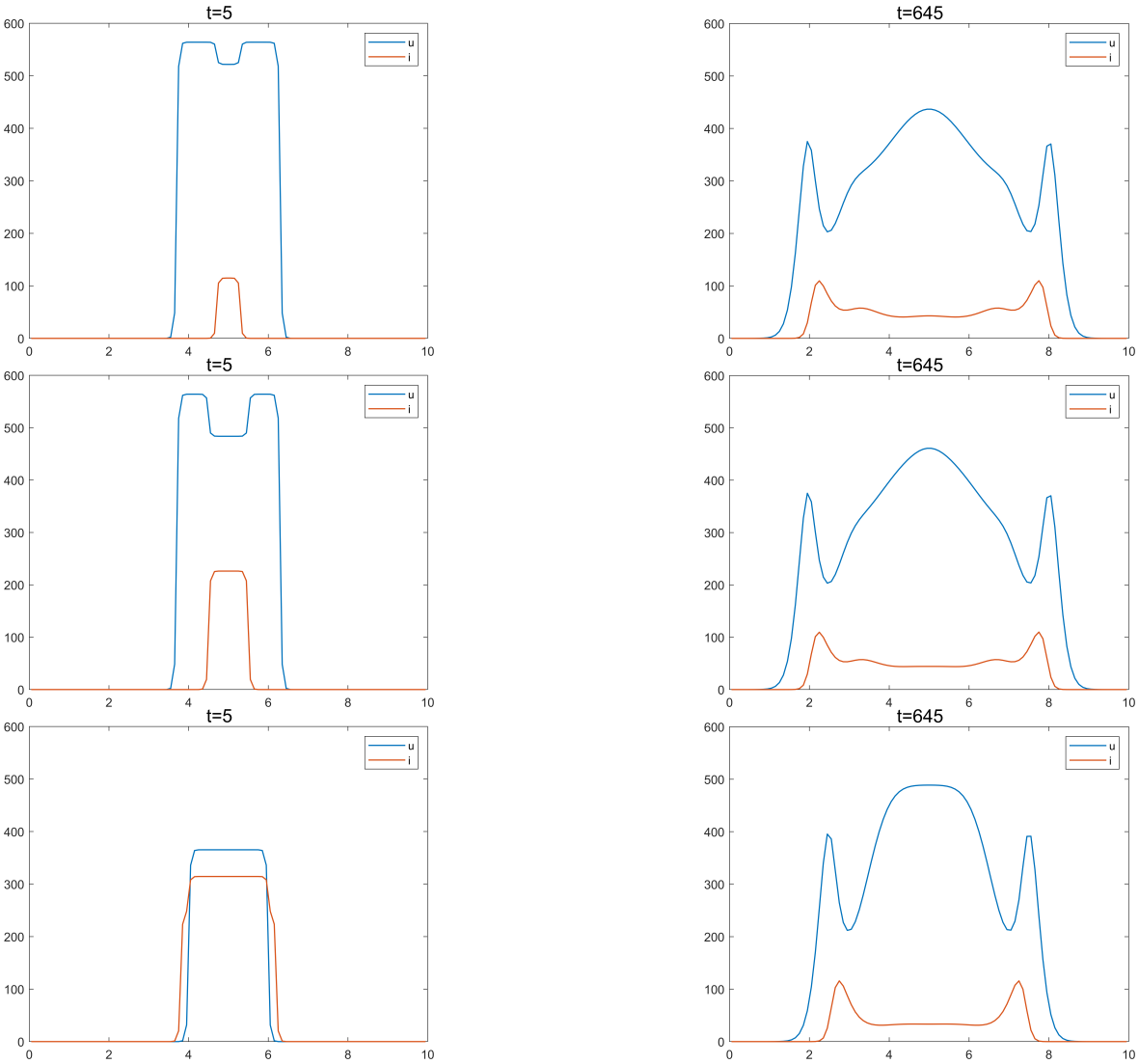

(a) $t = 5$ h (b) $t = 645$ h

Figure A.3: Spatial profiles of uninfected cells (blue) and infected cells (red) for the three simulation cases at two time points: an early stage ($t = 5$ h) and a later stage ($t = 645$ h). The figures are organised in rows, each corresponding to a different simulation case. The first row shows Case 1, characterised by a small initial infected area; the second row presents Case 2, where the initial infected region is of moderate size; the third row refers to Case 3, in which the infected area is initially large. The dynamics show how the initial conditions influence the competition between uninfected and infected cells over time.

The main observations are as follows:

- **Case 1**: The infected cells start with a limited volume and a low concentration. Growth occurs slowly, with contained expansion. The uninfected cells maintain a large area, and the progression is gradual.
- **Case 2**: The increase in the initial radius of the infected cells and their concentration leads to a greater expansion of the infected region over time. A more pronounced interaction between infected and uninfected cells is observed, with a progressive reduction in the latter.
- **Case 3**: The drastic reduction of the uninfected cell region and the expansion of the infected cells leads to faster growth of the infected cells, with a broader spatial distribution. The area of uninfected cells shrinks rapidly, suggesting a lower resistance to the spread of the infection.

Observing the evolution in the three cases, it emerges that the infected cells tend to grow faster and occupy more space when they start with a higher concentration and a larger domain. Expansion is instead limited when the initial area is small, suggesting that the diffusion dynamics are strongly dependent on the initial conditions.

In the first case, the uninfected cells manage to contain the growth of the infected cells, while in the second case, stronger competition is observed. In the third case, the reduced initial presence of uninfected cells allows for uncontrolled expansion of the infected cells.

These results indicate that modulating the initial conditions can significantly influence the outcome of treatment and the control of tumour progression.

A.1.6 Comparison between the two models

This section compares the simulations of the mathematical model based on partial differential equations (PDEs) conducted in the following spatial configurations:

- **2D Case (Radial Symmetry)**: Variation of cellular concentrations as a function of the radius r.
- **1D Case (Spatial Dimension x)**: Evolution of the system along a single spatial direction x.

The aim is to analyse the differences between these two representations and understand the effects of dimensionality on cellular dynamics.
The following images show the evolution of cell growth in the two simulations at the initial time points:

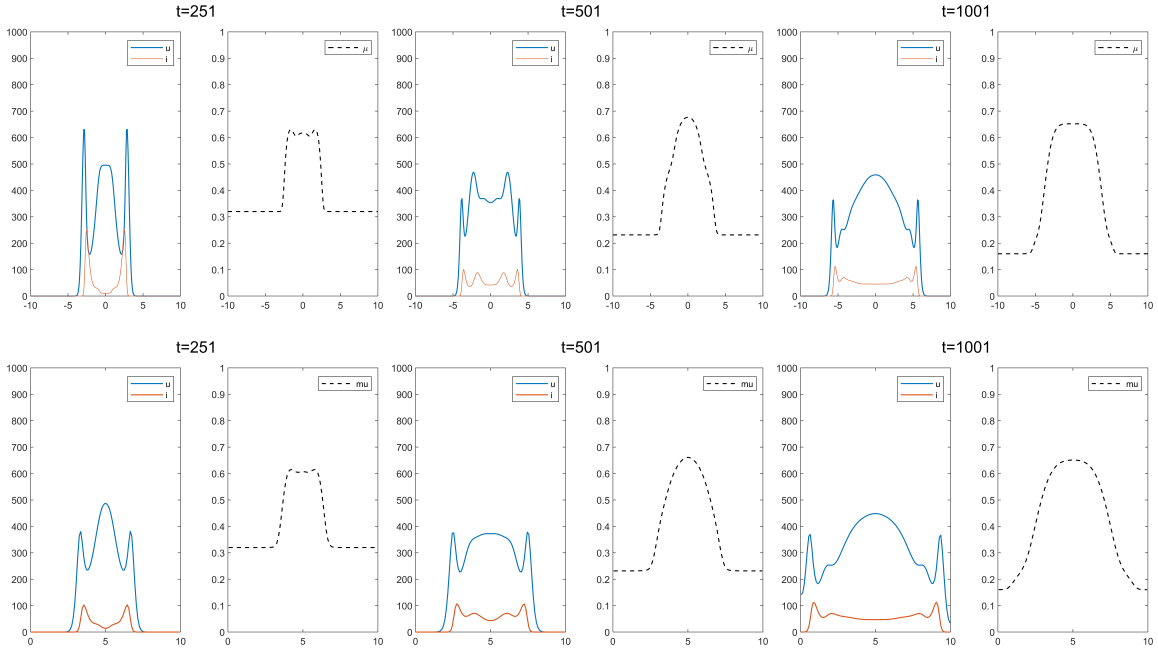

Figure A.4: Comparison between one-dimensional and two-dimensional simulations of the PDE model at three different time points: $t = 251h$, $t = 501h$, and $t = 1001h$. The first row shows the results for the one-dimensional case, while the second row refers to the two-dimensional case. Each column corresponds to a specific time point, increasing from left to right. For each simulation, the plots display on the left the spatial distribution of uninfected cells (in blue) and infected cells (in red), and on the right the corresponding epigenetic average μ. This comparison highlights how spatial dimensionality influences both the infection dynamics and the evolution of the phenotypic trait over time. Note the different scales, introduced to better capture the dynamics of the system.

The main differences between the 1D and 2D simulations include:

- **Propagation structure**: The 1D simulation shows the propagation of infected cells along a single direction, with a sharp advancing front. In the 2D model, growth is more diffused, and a more gradual radial propagation is observed.
- **Expansion of infected cells**: In 1D, the growth of infected cells is more evident in a single direction, with a sharp transition between infected and uninfected cells. In 2D, the growth of infected cells occurs on multiple fronts simultaneously, expanding symmetrically around the tumour's centre.
- **Interface between infected and uninfected cells**: In 1D, the interaction is more localised, and there is a well-defined separation between the two populations. In 2D, the transition is more gradual, and radial diffusion allows for greater mixing between the cells.
- **Effects of dimensionality**: The addition of a second dimension in the 2D model introduces greater complexity in the diffusion and growth dynamics. Infected cells can expand in radial direction, slowing the growth front compared to the 1D case, where propagation occurs more rapidly along the single available direction.

The comparison between the 1D and 2D simulations highlights how dimensionality significantly influences tumour growth dynamics. While the 1D model provides a simplified view, useful for quantitative analysis and quick calculations of cellular interactions, the 2D model offers a more realistic representation of spatial propagation and the diffusion of infected cells.

A.2 ABM

Similar to the PDEs, the complete equation for the density of uninfected cells ($u_{j,\ell,k}$) and infected cells ($i_{j,\ell}$) takes into account:

- motion along x and z;
- epigenetic mutation along y;
- proliferation/death;
- the infection process.

The equations have been reformulated to include additional terms that represent the contribution of nearby cells in the two spatial directions. Below are the equations of the extended 2D model, following the same rationale for the one-dimensionale case.

Density of uninfected cells

The dynamics of uninfected cells in two spatial dimensions (x and z) is described by the following equation:

$$
\begin{aligned}
u^{n+1}_{j,\ell,k} = {} & (1-\theta_y)\frac{\theta_u}{4}\left[u^n_{j-1,\ell,k} + u^n_{j+1,\ell,k} + u^n_{j,\ell-1,k} + u^n_{j,\ell+1,k}\right] \\
& + \frac{\theta_y}{4}\frac{\theta_u}{4}\left[u^n_{j-1,\ell,k+1} + u^n_{j-1,\ell,k-1} + u^n_{j+1,\ell,k+1} + u^n_{j+1,\ell,k-1}\right] \\
& + \frac{\theta_y}{4}\frac{\theta_u}{4}\left[u^n_{j,\ell-1,k+1} + u^n_{j,\ell-1,k-1} + u^n_{j,\ell+1,k+1} + u^n_{j,\ell+1,k-1}\right] \\
& + (1-\theta_y)(1-\theta_u)\left[1+\tau G(\rho^n_{j,\ell})\right]u^n_{j,\ell,k} \\
& + \frac{\theta_y}{4}(1-\theta_u)\left[u^n_{j,\ell,k+1} + u^n_{j,\ell,k-1}\right] \\
& \times (1-\tau\beta(y_k)i^n_{j,\ell}).
\end{aligned}
$$

Density of infected cells

The dynamics of infected cells is described as follows:

$$\begin{aligned} i_{j,\ell}^{n+1} = & \frac{\theta_i}{4}(1-\tau q)\left[i_{j-1,\ell}^n + i_{j+1,\ell}^n + i_{j,\ell-1}^n + i_{j,\ell+1}^n\right] \\ & + (1-\theta_i)(1-\tau q) i_{j,\ell}^n \\ & + \tau i_{j,\ell}^n \sum_k \beta(y_k)\chi u_{j,\ell,k}^n. \end{aligned}$$

The extension of the model from one spatial dimension (1D) to two dimensions (2D) introduces a series of structural changes, including the extension of spatial discretisation, increased complexity in diffusion and pressure calculations, the reformulation of random walks and infection spread, with overall more complex data memory management. The simulations of the ABM are still in progress and therefore not included in this thesis. These ideas will be further developed and implemented in MATLAB in future work.

Acknowledgements

First and foremost, I wish to express my sincere gratitude to **Professor Marcello Edoardo Delitala**, my supervisor, for his constant support, availability, and for offering me such a stimulating and intellectually engaging thesis topic. His trust, guidance, and presence throughout all stages of this work have been invaluable.

My heartfelt thanks also go to **Professor Federico Frascoli**, who warmly welcomed and supported me during my time at *Swinburne University of Technology* in Australia. His encouragement and availability—despite the distance—had a meaningful and tangible impact on the development of this project.

I would also like to thank the entire **Swinburne University of Technology** for the opportunity to carry out part of my research within its academic environment. I am grateful for the resources, hospitality, and inspiring atmosphere that greatly enriched both my professional and personal experience.

I am deeply grateful to **Dr David Morselli** for his technical assistance and remarkable patience during the more complex phases of this research, from mathematical modelling to the implementation of Matlab code. His expertise and generosity with his time were essential to the progress of my work.

I would also like to extend my sincere appreciation to the **Politecnico di Torino**, an institution that has consistently challenged and shaped me, providing the tools, knowledge, and opportunities necessary for both academic and personal growth.

Lastly, my deepest thanks go to my **family**, for their unwavering love, trust, and patience—far greater than I likely deserved. This achievement would not hold the same meaning without their presence and support throughout the entire journey.

Bibliography

[1] Enderling H. and Chaplain M.A.J. Mathematical modeling of tumor growth and treatment. *Current Pharmaceutical Design*, 20(30):4934–4940, 2014.

[2] Dejardin D., Kraxner A., Schindler E., Städler N., and Wolbers M. An overview of statistical methods for biomarkers relevant to early clinical development of cancer immunotherapies. *Frontiers in Immunology*, 15(1351584):1–17, 2023.

[3] C. Robert, M. M. Milhem, J. J. Sacco, and et al. Primary efficacy, safety, and survival data from the registration-intended cohort of patients with anti–PD-1–failed melanoma from the IGNYTE clinical trial with RP1 combined with nivolumab. *Journal of Clinical Oncology (supplement)*, 42(16):9517, 2024.

[4] T.D. de Gruijl, V. van Beusechem, M. Donia, and et al. ORCA-010 oncolytic therapy: Inducing tumor-specific immune responses and activation of tumor microenvironment in treatment-naïve prostate cancer. Abstract presented at the ESMO Immuno-Oncology Congress 2024, 2024.

[5] Paiva L. R., Silva H. S., Ferreira S. C., and Martins M. L. Multiscale model for the effects of adaptive immunity suppression on the viral therapy of cancer. *Physical Biology*, 10(2):025005, 2013.

[6] Wodarz D. and Komarova N. L. *Computational Biology of Cancer: Lecture Notes and Mathematical Modeling*. World Scientific, 1st edition, 2005.

[7] Morselli D., Delitala M. E., Jenner A. L., and Frascoli F. A hybrid discrete-continuum modelling approach for the interactions of the immune system with oncolytic viral infections. *arXiv*, abs/2404.06459:1–29, 2024.

[8] Zou H., Mou X, and Zhu B. Combining of oncolytic virotherapy and other immunotherapeutic approaches in cancer: A powerful functionalization tactic. *Global Challenges*, 7(9):2200094, 2022.

[9] Malinzi J., Ouifiki R., Eladdadi A., Torres D. F. M., and White K. J. A. Enhancement of chemotherapy using oncolytic virotherapy: Mathematical and optimal control analysis. *Mathematical Biosciences and Engineering*, 15(6):1435–1463, 2018.

[10] Wilkie K. P. and Hahnfeldt P. Mathematical models of immune-induced cancer dormancy and the emergence of immune evasion. *Interface Focus*, 3(4):20130010, 2013.

[11] de Pillis L. G. and Radunskaya A. E. The dynamics of an optimally controlled tumor model: A case study. *Mathematical and Computer Modelling*, 37(11):1221–1244, 2003.

[12] Timalsina A., Tian J. P., and Wang J. Mathematical and computational modeling for tumor virotherapy with mediated immunity. *Bulletin of Mathematical Biology*, 79(8):1736–1758, 2017.

[13] Wang Y., Zhu M., Chi H., Liu Y., and Y G. The combination therapy of oncolytic virotherapy. *Frontiers in Pharmacology*, 15:1380313, 2024.

[14] Tonekaboni S. A. M., Dhawan A., and Kohandel M. Mathematical modelling of plasticity and phenotype switching in cancer cell populations. *Mathematical Biosciences*, 283:30–37, 2017.

[15] Gatenby R. A. and Gillies R. J. A microenvironmental model of carcinogenesis. *Nature Reviews Cancer*, 8(1):56–61, 2008.

[16] Almeida L., Audebert C., Leschiera E., and Lorenzi T. Discrete and continuum models for the coevolutionary dynamics between CD8+ cytotoxic T lymphocytes and tumour cells. *Mathematical Medicine and Biology: A Journal of the IMA*, 40(2):141–174, 2023.

[17] Conte M., R. T. Woodall A., Xella, Cassady K. A., Branciamore S., Brown C. E, and Rockne R. C. Car T-cell and oncolytic virus dynamics and determinants of combination therapy success for glioblastoma. *bioRxiv*, 2025.01.23.634499, 2025.

[18] Chisholm R. H., Lorenzi T., Desvillettes L., and Hughes B. D. Evolutionary dynamics of phenotype-structured populations: from individual-level mechanisms to population-level consequences. *Zeitschrift für angewandte Mathematik und Physik*, 67(1–2):1–34, 2016.

[19] Macfarlane F. R., Ruan X., and Lorenzi T. Individual-based and continuum models of phenotypically heterogeneous growing cell populations. *AIMS Bioengineering*, 9(1):68–92, 2022.

[20] Lorenzi T., Pugliese A., Sensi M., and Zardini A. Evolutionary dynamics in an si epidemic model with phenotype-structured susceptible compartment. *Journal of Mathematical Biology*, 83(6–7):72, 2021.

[21] Morselli D., Delitala M. E., and Frascoli F. Agent-based and continuum models for spatial dynamics of infection by oncolytic viruses. *Bulletin of Mathematical Biology*, 85(10):92, 2023.

[22] Kaid Z., Pouchol C., and Clairambault J. A phenotype-structured model for the tumour-immune response. *Mathematical Modelling of Natural Phenomena*, 18(22):22, 2023.

[23] Fiandaca G., Delitala M. E., and Lorenzi T. A mathematical study of the influence of hypoxia and acidity on the evolutionary dynamics of cancer. *Bulletin of Mathematical Biology*, 83:37, 2020.

[24] Villa C., Maini P. K., A. P. Browning, Jenner A. L., Hamis S., and Cassidy T. Reducing phenotype-structured PDE models of cancer evolution to systems of ODEs: a generalised moment dynamics approach. *arXiv*, 2024.

[25] Leschiera E., Lorenzi T., Shen S., Almeida L., and Audebert C. A mathematical model to study the impact of intra-tumour heterogeneity on anti-tumour CD8+ T cell immune response. *arXiv*, 2021.

[26] Celora G. L., Byrne H. M., Zois C., and Kevrekidis P. G. Phenotypic variation modulates the growth dynamics and response to radiotherapy of solid tumours under normoxia and hypoxia. *arXiv*, 2021.

[27] Wang S., Li Y., Xu C., Dong J., and Wei J. An oncolytic vaccinia virus encoding hyaluronidase reshapes the extracellular matrix to enhance cancer chemotherapy and immunotherapy. *Journal for ImmunoTherapy of Cancer*, 12(3):e008431, 2024.

[28] Zamarin D., Lee P. W., and Diallo J. S. Oncolytic virotherapy. *Nature Reviews: Cancer*, 14:1–12, 2014.

[29] Feng S., Hu K., Li M., Zhang Y., and Wang J. Enhancement of oncolytic virotherapy by combining with chemotherapy and immunotherapy. *OncoTargets and Therapy*, 11:5993–6002, 2018.

[30] Maio M. and NIBIT Foundation. Overcoming immunotherapy resistance with epigenetic priming: The NIBIT-ML1 trial. Clinical trial report, 2022.

[31] Aghi M. K., Liu T., Rabkin S., and Martuza R. L. Hypoxia enhances the replication of oncolytic herpes simplex virus. *Molecular therapy: the Journal of the American Society of Gene Therapy*, 17(1):51–56, 2009.

[32] Guo Z. S. The impact of hypoxia on oncolytic virotherapy. *Virus Adaptation and Treatment*, 3(1):71–82, 2011.

[33] Shayan S., Arashkia A., and Azadmanesh K. Modifying oncolytic virotherapy to overcome the barrier of the hypoxic tumor microenvironment. Where do we stand? *Cancer Cell International*, 22(1):370, 2022.

[34] Russell S. J., Peng K., and Bell J. C. Oncolytic virotherapy. *Nature Biotechnology*, 30(7):658–670, 2012.

[35] Cristi F., Gutiérrez T., Hitt M. M., and Shmulevitz M. Genetic modifications that expand oncolytic virus potency. *Frontiers in molecular biosciences*, 9:831091, 2022.

[36] Davola M. E., Vito A., Wei J., El-Sayes N., Workenhe S., and Mossman K. L. Genetic modification of oncolytic viruses to enhance antitumor immunity. *Methods in Enzymology*, 635:231–250, 2020.

[37] Yin Z. and Wang Z. Strategies for engineering oncolytic viruses to enhance cancer immunotherapy. *Frontiers in pharmacology*, 15:1450203, 2024.

[38] Zhao Z., Cao L, Sun Z., Liu W., Li X., Fang K., Shang X., Hu J., Chen H., and Lou Z. A structure-guided genetic modification strategy: Developing seneca valley virus therapy against nonsensitive nonsmall cell lung carcinoma. *Journal of Virology*, 97(14):e00459-23, 2023.

[39] Dong H., Li M., Yang C., et al. Combination therapy with oncolytic viruses and immune checkpoint inhibitors in head and neck squamous cell carcinomas: an approach of complementary advantages. *Cancer Cell International*, 23(1):1, 2023.

[40] Garofalo M., Bertinato L., Staniszewska M., et al. Combination therapy of novel oncolytic adenovirus with anti-pd1 resulted in enhanced anti-cancer effect in syngeneic immunocompetent melanoma mouse model. *Pharmaceutics*, 13(4):547, 2021.

[41] Spiesschaert B., Angerer K., Park J., and Wollmann G. Combining oncolytic viruses and small molecule therapeutics: Mutual benefits. *Cancers*, 13(14):3386, 2021.

[42] Everts A., Bergeman M., McFadden G., and Kemp V. Simultaneous tumor and stroma targeting by oncolytic viruses. *Biomedicines*, 8(11):474, 2020.